GKSS
FORSCHUNGSZENTRUM
in der HELMHOLTZ-GEMEINSCHAFT

Micromechanical Modeling of the Deformation of HCP Metals

(Vom Promotionsausschuss der Fakultät V: Verkehrs-und Maschinensysteme der Technischen Universität Berlin im Jahr 2007 als Dissertation angenommene Arbeit)

Author:

S. Graff

ISSN 0344-9629

HELMHOLTZ
| GEMEINSCHAFT

GKSS 2008/1

GKSS 2008/1

Micromechanical Modeling of the Deformation of HCP Metals

(Vom Promotionsausschuss der Fakultät V: Verkehrs-und Maschinensysteme der Technischen Universität Berlin im Jahr 2007 als Dissertation angenommene Arbeit)

Author:
S. Graff
(Institute of Materials Research)

GKSS-Forschungszentrum Geesthacht GmbH · Geesthacht · 2008

Die Berichte der GKSS werden kostenlos abgegeben.
The delivery of the GKSS reports is free of charge.

Anforderungen/Requests:

GKSS-Forschungszentrum Geesthacht GmbH
Bibliothek/Library
Postfach 11 60
D-21494 Geesthacht
Germany
Fax.: (49) 04152/871717

ISSN 0344-9629

GKSS-Forschungszentrum Geesthacht GmbH · Telefon (04152) 87-0
Max-Planck-Straße 1 · D-21502 Geesthacht / Postfach 11 60 · D-21494 Geesthacht

GKSS 2008/1

Micromechanical Modeling of the Deformation of HCP Metals

(Vom Promotionsausschuss der Fakultät V: Verkehrs- und Maschinensysteme der Technischen Universität Berlin im Jahr 2007 als Dissertation angenommene Arbeit)

Stéphane Graff

117 pages with 55 figures and 11 tables

Abstract

Nowadays, intense research is conducted to understand there lation between microstructural features and mechanical properties of hexagonal close-packed (hcp) metals. Due to their hexagonal structure, hcp metals exhibit mechanical properties such as strong anisotropy, which is more pronounced than for construction metals with cubic crystal structure, and tension/compression asymmetry. Deformation mechanisms in hcp metals, dislocation motion on specific slip systems and activation of twinning, are not yet completely understood.

The purpose of this work is to link the physical mechanisms developing during deformation of magnesium (Mg) on the microscale with the macroscopic yielding properties of texture Mg samples. It will be shown that the mechanical behavior of hcp metals may be understood and reproduced with the help of a visco-plastic model for crystal plasticity and a phenomenological yield criterion with appropriate hardening behavior.

The study of single crystal specimens subjected to channel die compression tests reveals the active slip systems and twinning systems of the material considered. The material anisotropy at mesoscale is reproduced by using adequate critical resolved shear stresses (CRSS) for the considered deformation mechanisms. In order to describe the macroscopic behavior, texture is incorporated into polycrystalline Representative Volume Elements (RVEs) and various mechanical properties of extruded bars and rolled plates can be predicted. For RVEs exhibiting the texture of rolled plates the numerical results reveal the plate's anisotropic yielding and hardening behavior on a mesoscale.

In order to extend the modeling possibilities to process simulations and to allow for time-saving simulations of structural behavior, a phenomenological yield surface accounting for anisotropy and tension/compression asymmetry has been established and implemented in a finite element code. Its numerous model parameters are calibrated by an optimization procedure based on a Monte-Carlo search and the strain hardening behavior is described by an evolution of the parameters with plastic strain. This model is finally applied in deep drawing simulations of a cup.

Mikromechanische Modellierung der Verformung in Metallen mit hexagonaler Gitterstruktur

Zusammenfassung

Heutzutage wird intensive Forschung betrieben, um den Zusammenhang zwischen mikrostrukturellen Eigenschaften und mechanischem Verhalten von Metallen mit hexagonaler Gitterstruktur zu verstehen. Wegen ihrer hexagonalen Struktur verfügen diese Metalle über Besonderheiten der mechanischen Eigenschaften wie eine starke Anisotropie, die ausgeprägter ist als für Konstruktionsmetalle mit kubischer Kristallstruktur, und Zug-/Druck-Asymmetrie. Die Verformungsmechanismen in Metallen mit hexagonaler Gitterstruktur, wie Versetzungsbewegungen auf bestimmten Gleitsystemen und Bildung von Zwillingen, sind bis heute noch nicht vollständig verstanden.

Das Ziel der vorliegenden Arbeit ist es, die physikalischen Mechanismen, die während der Verformung von Magnesium auf der Mikroebene auftreten, mit dem makroskopisches Fließverhalten von texturierten Magnesiumproben in Korrelation zu bringen. Es wird gezeigt, dass das atypische mechanische Verhalten dieser Metalle mit Hilfe eines visko-plastischen Modells für Kristallplastizität und eines phänomenologischen Fließkriteriums mit angepasstem Verfestigungsverhalten verstanden und reproduziert werden kann.

Die Untersuchung von Einkristallproben in so genannten „Channel-Die“-Druckversuchen offenbart die aktiven Gleit- und Zwillingssysteme des Materials. Die Anisotropie des Materials auf Makroebene wird durch entsprechende kritische Schubspannungen (CRSS) für die angenommenen Verformungsmechanismen reproduziert. Um das makroskopische Verhalten von Polykristallen zu beschreiben, werden repräsentative Volumenelemente (RVE) als Anordnungen einer Vielzahl unterschiedlich orientierter Einkristalle betrachtet. Die Orientierungsverteilung wird der makroskopisch gemessenen Textur angepasst. Durch numerische Simulationen an diesen RVE kann das Fließverhalten von extrudiertem Material und gewalzten Blechen vorhergesagt werden.

Um Simulationen auf makroskopischer Ebene, z.B. von Umformversuchen, mit vertretbarem Aufwand durchführen zu können, wurde eine phänomenologische Fließfläche, die die Anisotropie und die Zug-/Druck-Asymmetrie berücksichtigt, in einen Finite-Elemente-Programm implementiert. Diese Fließfläche erfordert die Anpassung einer großen Anzahl von Modelparametern, die mit einer Monte-Carlo-Suche angepasst werden. Das Verfestigungsverhalten wird durch eine Entwicklung dieser Parameter mit der plastischen Vergleichsdehnung nach von Mises beschrieben. Dieses Modell wird dann für Tiefziehsimulationen eines Napfes eingesetzt.

Manuscript received / Manuskripteingang in TKP: 16. Januar 2008

Contents

Chapter 1

Introduction

In today life it has become very common and easy to travel, either by car or by plane. Since many car manufacturing companies and firms operating airplanes are present on the market the travelling possibilities have increased a lot and the travelling costs for the customer have been reduced at the same time. The main way in reducing the travelling costs is to reduce fuel consumption. This is particularly true because fuels price has increased drastically during the last years and will go on increasing constantly in next decades.

Partly for this reason, magnesium alloys have attracted attention in recent years as lightweight materials for the transportation industry. Indeed, the low density of magnesium (1.74 g/cm^3) and its relatively high specific strength make it an excellent candidate for the development of alloys destined to save structural weight and consequently fuel consumption in the automotive industry [58, 41, 28]. However, magnesium (Mg) and magnesium alloys components exhibit unusual mechanical properties for structural metals, like a pronounced anisotropy and unlike yielding in tension and compression. These mechanical properties as well as the limited ductility of magnesium wrought alloys at room temperature is related to their hexagonal close-packed (hcp) structure and the corresponding deformation mechanisms activated during plastic deformation. Indeed, metals with hcp crystalline structures present a reduced number of available slip systems compared to body centered cubic (bcc) and face centered cubic (fcc) geometries, which makes the accommodation of arbitrary plastic deformation difficult. In hcp metals, mechanical twinning therefore goes along with dislocation slip during plastic deformation.

A profound understanding of these underlying mechanisms of dislocation gliding and mechanical twinning for magnesium wrought alloys, at single crystal and polycrystalline level, would thus contribute to a knowledge based characterization of those alloys. Creating such a knowledge is one goal of this work. It is necessary to help in improving the mechanical performances of magnesium alloys and the fabrication processes of components made out of these alloys.

Tests on single crystals of hcp metals for various crystallographic orientations are sophisticated, and the respective literature is scarce. Wonsiewicz and Backhofen [85] as well as Kelley and Hosford [43, 44] conducted thorough channel die tests on single crystal

Mg specimens, displaying its complex deformation behavior and revealing the active slip and twinning systems. The data in [43, 44] are used in this work to identify the material parameters of constitutive equations based on crystal plasticity, which is then used for predicting the mechanical behavior at mesoscopic level of polycrystalline representative volume elements (RVEs). In this way the microscopic features developing during plastic deformation of Mg are linked to the mesoscale and allow for the prediction of yielding behavior of arbitrarily textured solids as for example extruded bars or rolled plates. The atypical yielding behavior at single crystal and polycrystalline aggregate level is shown to be very sensitive to the material parameters identified as well as to the crystallographic orientation and thus to the material texture.

As simulations of the structural behavior of polycrystalline structures cannot be performed effectively with models of crystal plasticity, which require much computationnal time, models with phenomenological constitutive equations, which do not account for microstructural events and materials texture, need to be developed. Developing such a model is another goal of this work. Finally, such models for phenomenological modeling are used for the design of industrial products because they allow for accurate predictions of the mechanical behavior of components.
A yield potential proposed by Cazacu and Barlat [19], which accounts for anisotropy and unlike yielding in tension and compression, is introduced in the present work. The procedure for the identification of its numerous model parameters, which can be realized with the help of the yield surfaces generated by the crystal plasticity based RVE calculations, is presented. Finally, numerical simulations of the deep drawing process of rolled plates is presented and the structural mechanical behavior of the sheets depending on the material anisotropy is discussed.

In this work a method linking mechanical behavior at single crystal level and at structural level, going trough polycrystalline aggregates, is developed and applied to magnesium. This methodology allows for a deep understanding of micromechanical features occuring during plastic deformation of Mg and for the prediction of mechanical behavior of components at structural level by requiring only a reduced amount of experimental data. The methodology presented here, is not restricted to Mg but may be applied to any other hcp metal.

Chapter 2

Deformation Mechanisms in Metals

2.1 Crystallographic Structure of Metals

Contrary to plastics or ceramics, whose constitutive molecules are disorganised, metals have an organised crystallographic structure. The common crystallographic structures encountered in metals, body centered cubic (bcc), face centered cubic (fcc), and hexagonal close-packed (hcp) are illustrated in Figure 2.1.
In this figure the spheres represent the metal atoms which are perfectly organised such that the presented structures are repeated periodically in the three dimensions of space. For example, α-iron crystallises into the bcc structure while aluminium, copper and nickel build fcc structures, and magnesium or zinc crystallise into the hcp structure.

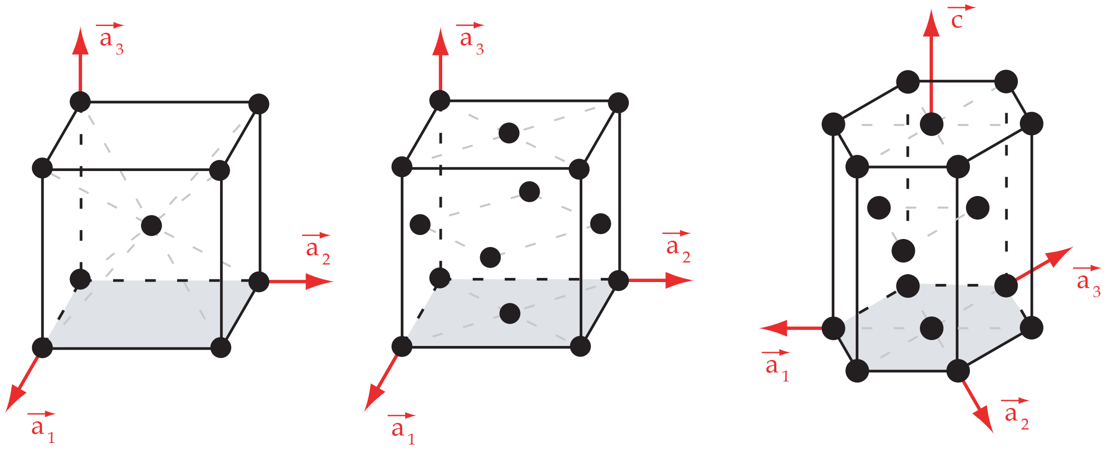

Figure 2.1: *Crystallographic structures of metals: body centered cubic (bcc), face centered cubic (fcc), and hexagonal close-packed (hcp) lattice structures*

As shown in Figure 2.1, planes and directions of the cubic lattice can be represented easily in the cartesian coordinate system $(\vec{a}_1, \vec{a}_2, \vec{a}_3)$. In the case of hcp metals, planes and directions of the hexagonal lattice can be described with the Miller-Bravais indices related to a coordinate system of three basal vectors $\vec{a}_i$ and the longitudinal axis $\vec{c}$, also called c-axis later. Even if metals tend to crystalize in these perfect organised structures pile up defaults, also named dislocations, appear to be extremely frequent and play a crucial role in the deformation behavior of metals.

2.2 Slip Mechanism and Hardening Behavior

Deformation of metals may be of two natures, elastic and plastic. A comparison between elastic and plastic deformations resulting from shear loading is made in Figure 2.2. Elastic deformation corresponds to pure lattice stretching and is fully reversible as the applied load is supressed. Plastic deformation instead is irreversible since a residual deformation remains after the load is supressed, and is controled by slip of dislocations on specific crystallographic planes and in specific directions which is triggered by mechanical shear loading.

A given combination of a crystallographic plane and crystallographic direction is defined as a slip system. This form of plastic deformation is particularly true at low homologous temperatures, which is of interest in the present work, while at high homologous temperatures additional mechanisms like recrystallisation and grain-boundary sliding for example may take place.

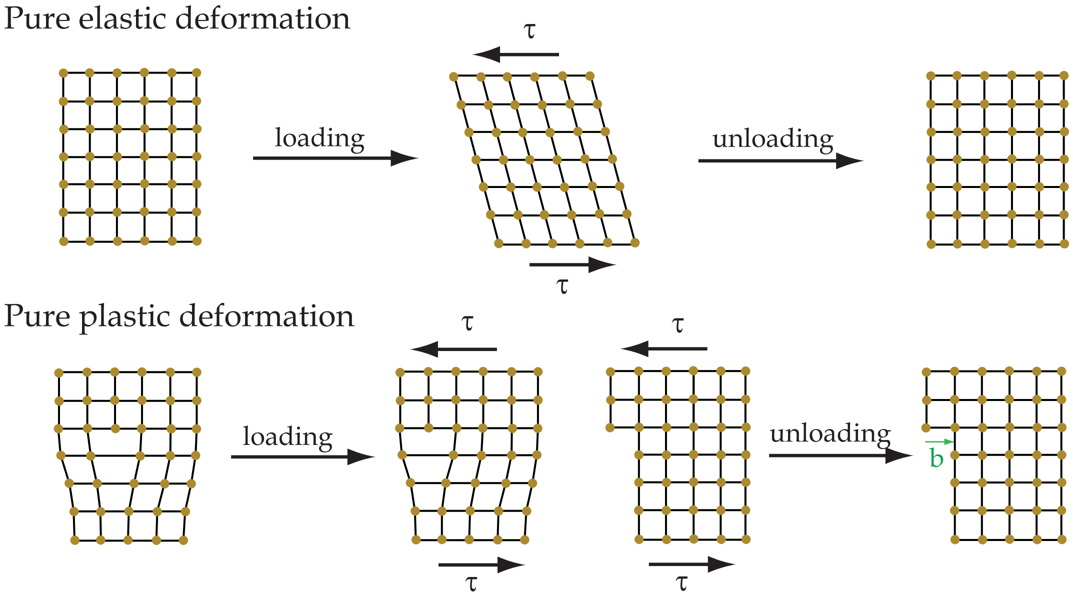

Figure 2.2: *Elastic deformation corresponding to pur stretching of the crystal lattice (up) and plastic deformation trough dislocation slip (down)*

The relative displacement of the two crystal halves resulting in the remaining plastic deformation is called the Burgers vector $\vec{b}$ and its magnitude is one atomic distance on the example of Figure 2.2. Schmid [69] observed that slip for a specific slip system is activated when a critical value of shear stress is reached. This value is also called critical resolved shear stress (CRSS) of the slip system.

In the case of a tensile test, schematically represented in Figure 2.3, this observation leads to the following relation between critical applied stress σ_c and critical shear stress τ_c,

$$\tau_c = \sigma_c cos(\lambda) cos(\varphi) \tag{2.1}$$

where $\mu = cos(\lambda)cos(\varphi)$ is the so called Schmid factor. This relation is usually called the Schmid law.

The stress strain curve of Figure 2.3 shows that the applied stress $\sigma_{applied}$ is a linear function of the deformation strain ϵ in the range of elastic deformation corresponding to $\sigma_{applied} \leq \sigma_c$. This mechanical behavior observed at macroscopic scale is called linear elasticity. As the applied stress becomes higher than σ_c the macroscopic relation between stress and strain is not linear anymore and the mechanical behavior is called plastic. As the sample in unloaded a deformation called plastic deformation remains and the new critical stress σ_c to be reached in order to escape the elastic range and to enter into plasticity is higher, the material is hardening.

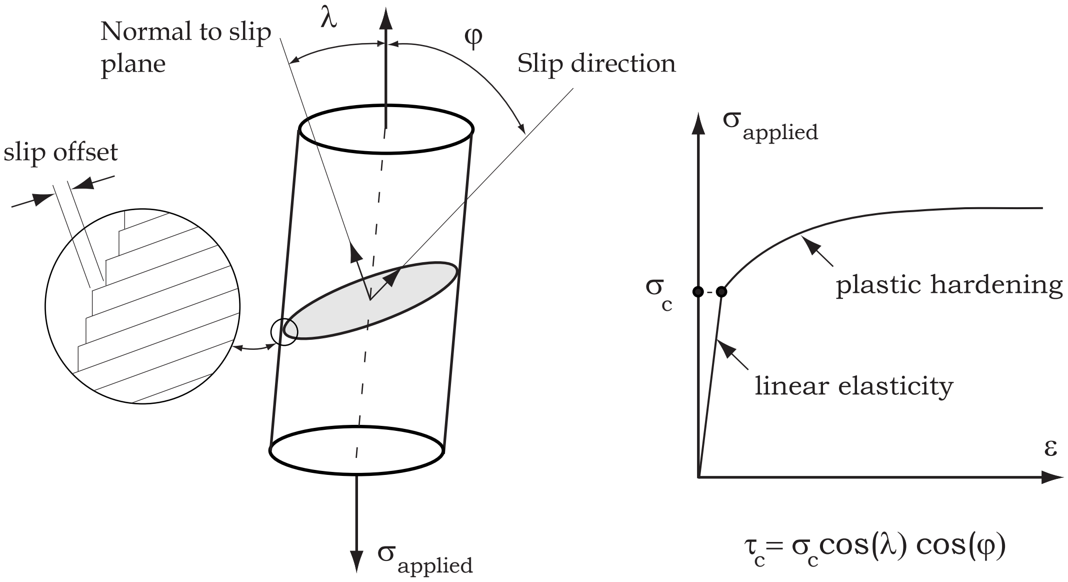

Figure 2.3: *Relationship between applied stress* $\sigma_{applied}$ *and shear stress* τ *acting on a specific slip system in a uniaxial tensile test*

Indeed, metals harden after the limit of elasticity is reached which is directly related to dislocations moving into the tested sample as well as an increasing number of such dislocations and therefore an increasing interaction of the dislocations with the movement of others. Dislocations may be of different natures, ideally of edge or of screw character but almost always of mixed edge and screw character. They may interact in many ways with other dislocations or obstacles like impurities and precipitate creating thus jogs, vacancies, new dislocation sources and others.

Describing in detail the mechanism of dislocation mechanics is omitted here since this is beyond the scope of this work. Further information of microstructural observations of dislocations interactions may be found for example in Cottrell [21] or Seeger [71] and more detailed information about dislocation mechanics may be found for example in [35, 36, 10].

2.3 Mechanical Twinning

Mechanical twinning is a deformation mode controled by mechanical shear loading like slip. Contrary to slip, where the crystallographic orientations remain unchanged, mechanical twinning corresponds to a sudden reorientation of a small distinct volume of the crystal lattice. Figure 2.4 shows an example of mechanical twinning. The planes of symmetry, twin planes, separate the twinned region from the untwinned regions of the crystal lattice. Whether mechanical twinning is triggered by a critical shear stress, as dislocation slip is, remains an open question.

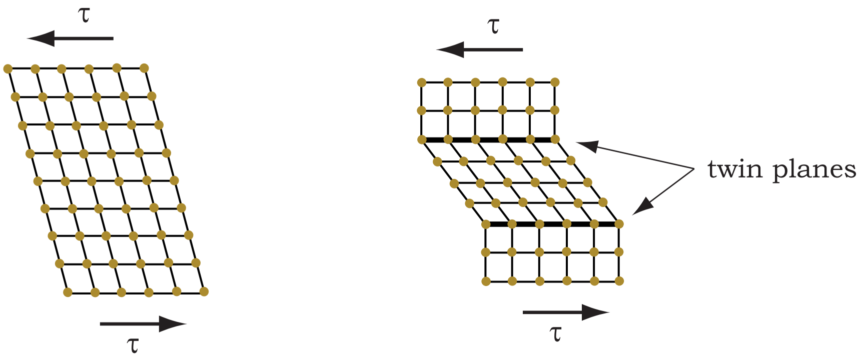

Figure 2.4: *Crystal lattice reorientation due to mechanical twinning*

This deformation mode may occur in most crystals but hcp metals are particularly subjected to twinning, especially at low homoglogous temperatures. In hcp metals the twinning systems can be activated by either tension or compression of the c-axis, depending on whether the deformation results in an elongation or a shortening of the c-orientation.

2.4 Deformation of hcp Metals

A non exhaustive list of deformation modes frequently observed in hcp metals are presented in Figure 2.5. Slip systems are defined via a plane and a direction in which, and along which, a dislocation may move, respectively, as subjected to external loading. Mechanical twinning is defined via a plane only, the twin plane.
Their are always several equivalent slip and twinning systems, due to the symmetry of the hexagonal structure, but only one of each family is displayed in Figure 2.5 for clarity. As it can be seen in Figure 2.5, which is not even complete, the number of different families of deformation modes which may occur in hcp metals is high, however, hcp materials generally have a small number of active modes. The nature of dislocations in an hexagonal lattice may be regrouped in three families, $\langle a \rangle$, $\langle c \rangle$ and $\langle a + c \rangle$, with respective Burgers vectors of lengths a, c and $\sqrt{a^2 + c^2}$, see Figure 2.5. Which of these slip systems gets activated, depends among other factors on the aspect ratio a/c.
The restricted number of available slip systems in hcp metals, which is due to the low symmetry of the hexagonal lattice, usually makes the accommodation of arbitrary strains through dislocation slip only difficult. It becomes especially difficult if the number of

independent slip systems is less than 5, which have been shown by von Mises [84] to be the minimum needed to undergo homogeneous deformation by crystallographic slip in polycrystals. For this reason, twinning is often an additionnal deformation mode in hcp metals which allows for deformation in c-direction. A detailed review concerning crystallography and deformation modes of hcp metals can be found in Partridge [61].

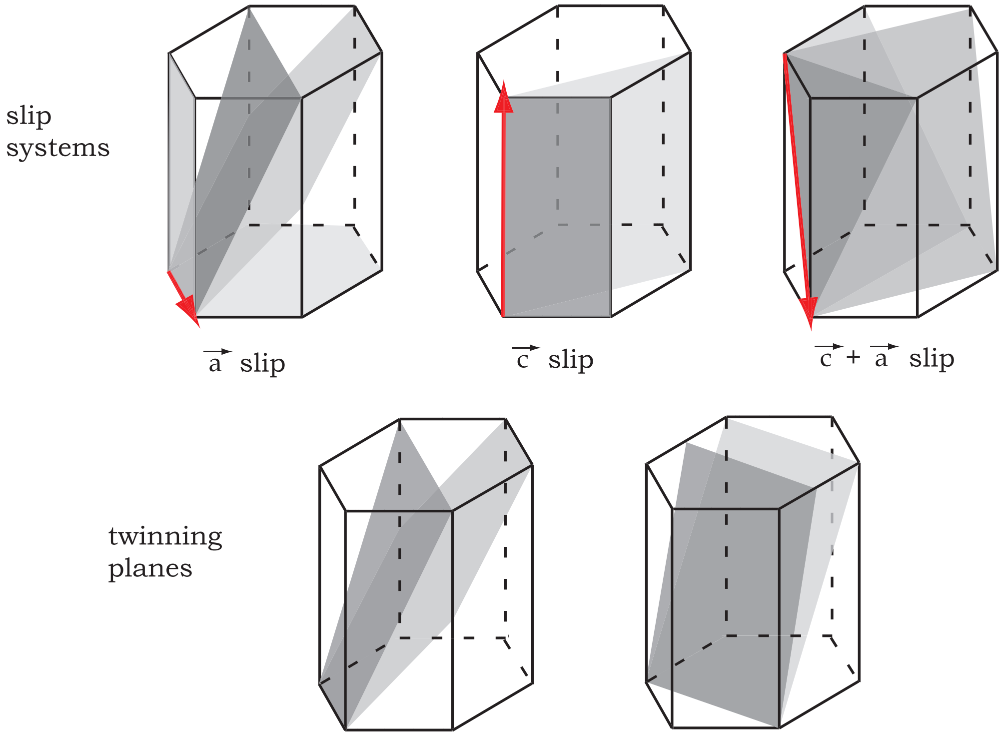

Figure 2.5: *Frequently observed deformation modes in hcp metals, grey surfaces represent slip and twinning planes, vectors represent slip directions*

2.5 The Special Case of Magnesium

As shown in the previous section, the number of possible deformation modes in hcp metals is high and identifying those active in a specific material is not a trivial task. In this section the deformation modes of magnesium are discussed refering to experimental evidences and numerical studies. The deformation modes mentioned later in this section are listed in Figure 2.6.

2.5.1 Experimental Evidences

Historically, the deformation mechanisms of magnesium at low homologous temperatures were found to be mainly basal slip and twinning, see Beck [13]. At room temperature tensile twinning has been far the most observed twinning mechanism. At temperatures above $225\,°C$ other slip systems like pyramidal $\langle a\rangle$ were supposed to be active in order to explain the increasing ductility of Mg.

The deformation mechanisms of Mg have been studied further in detail in the 50's and 60's in a wide temperature range from approximately $-190\,°C$ to above $350\,°C$. Burke and Hibbard [18] performed tensile tests of magnesium single crystals in different crystallographic orientations. Basal slip was found to be the only activated deformation mode in a wide range of orientations, prismatic $\langle a\rangle$, pyramidal $\langle a\rangle$, and tensile twin where observed as well. Tensile tests on high purity Mg extrusion samples performed by Hauser et al. [30, 29] at $25\,°C$ revealed basal slip to be the predominant deformation mechanism. Basal slip was suggested to be the predominant deformation mechanism as it was found to be uniformly distributed all over the grains, while traces of slip on the prismatic planes have been observed only in parts of the grain which may have been subjected to higher stresses such as near corners or reentrant angles.

Since basal slip is identified to be an easy glide slip system in Mg at low temperatures, Reed-Hill and Robertson [64] as well as Yoshinaga and Horiuchi [89] performed tensile tests on Mg single crystal with basal plane parallel to the loading direction. This orientation of the single crystals aims to make non-basal slip much more favorable while avoiding basal slip. Both studies showed prismatic $\langle a\rangle$ glide to be the predominant deformation mechanism at room temperature in these conditions. At high temperatures slip markings have been observed in [89] suggesting that pyramidal $\langle a\rangle$ slip may have contributed to plastic deformation. Reed-Hill and Robertson [65] concluded from tensile tests on notched specimens that pyramidal $\langle a\rangle$ slip is not an important mode of plastic deformation at room temperature.

Basal slip and prismatic $\langle a\rangle$ slip constitute 4 independent slip systems, and since pyramidal $\langle a\rangle$ produces a strictly equivalent shape change than combined basal and prismatic $\langle a\rangle$ slip, the number of independent shear systems issued from all 3 deformation modes observed in magnesium keeps 4. However, 4 independent shear systems is not enough to satisfy the criterion of von Mises [84]. Indeed, the von Mises criterion stipulates that 5 independent shear systems are required for a polycrystal to undergo homogeneous strain deformation without change in volume, which is the general assumption in metal plasticity. Tegart [79] suggested therefore non-basal slip systems having a component in c-direction to operate in hcp metals.

For the reasons detailed just before further studies have focused on understanding non-basal deformation mechanisms in Mg. With the expectation to avoid twinning and slip of pure $\langle a\rangle$ nature, Wonsiewicz and Backofen [85] as well as Kelley and Hosford [43] have performed channel die experiments of single crystals and polycrystalline material. In these tests no deformation mode with component in $\langle c\rangle$ direction, other than mechanical twinning, could be identified. Stohr and Poirier [74] and Obara et al. [59] have observed pyramidal $\langle a+c\rangle$ glide while performing respectively tension and compression tests on single crystals at relatively low homologous temperatures. These have been the first evidences of non-basal slip presenting a contribution for deformation in $\langle c\rangle$ direction in magnesium. Recently, Ando and Tonda [6] also identified pyramidal $\langle a+c\rangle$ as an active deformation mechanism at relatively low homogeneous temperatures. The Critical Resolved Shear Stress (CRSS) for pyramidal $\langle a+c\rangle$ systems determined in [74, 59, 6] for the ranges of temperatures analyzed is not identical, which is discussed in detail in Yoo et al. [88]. Yoo et al. [87] also introduced a source mechanism for $\langle a + c \rangle$ slip based on geometric and energetic considerations for hcp metals and alloys. This source mechanism is however unfavorable for Mg.

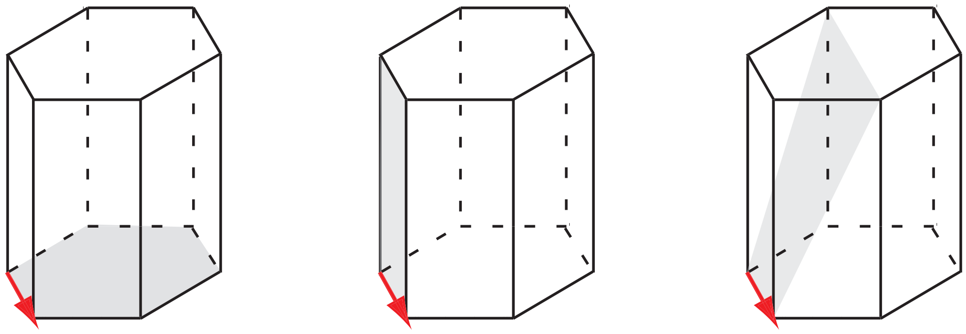

basal <a> prismatic <a> pyramidal <a>

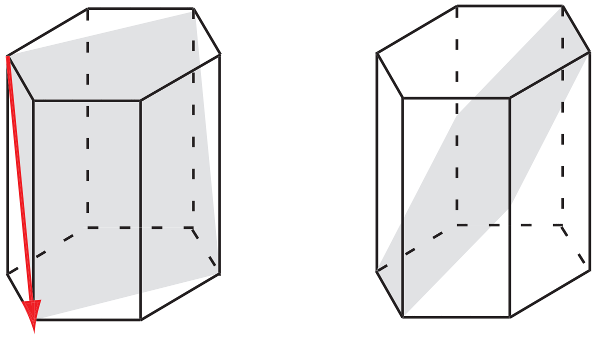

pyramidal <a+c> tensile twin

Figure 2.6: *Deformation modes observed in magnesium, grey surfaces represent slip and twinning planes, vectors represent slip directions*

2.5.2 Numerical Investigations

Modeling activities for understanding better the features of plastic deformation in magnesium alloys started recently and concentrate almost only on the alloy AZ31 and its variation AZ31B because they are the most common wrought magnesium alloys.
Agnew et al. [4] studied, among others, the relation between mechanical behavior and texture evolution of AZ31B. In order to reproduce similar textures than those observed experimentally, $\langle a + c \rangle$ slip needed to be taken into account. They even concluded that prismatic $\langle a \rangle$ slip should keep marginal for avoiding undesired features in the simulated texture. Thus, they have considered only basal, pyramidal $\langle a + c \rangle$ and tensile twin in the mechanical behavior simulations of AZ31B. These considerations showed to be satisfying at simulating uniaxial compression tests of a plate for both in-plane and through-thickness orientations.
In later studies, Agnew et al. [3] and Agnew and Duygulu [2] added prismatic $\langle a \rangle$ to

the previous set of deformation modes. Indeed, non-basal slip in $\langle a \rangle$ direction has been shown in [3, 2] to be necessary for modeling the in-plane anisotropy of AZ31B rolled plates at low temperatures.

Brown et al. [16] emphasize the importance of tensile twin and $\langle a+c \rangle$ slip in contributing to plastic deformation while modeling texture evolution of AZ31B rolled plates subjected to in-plane compression.

Staroselsky and Anand [73] could model the macroscopic mechanical behavior in tension and compression as well as the respective texture evolution of AZ31B extruded rods and rolled plates without considering any slip system having a deformation component oriented in $\langle a + c \rangle$ direction. The considered deformation mechanisms, basal, prismatic $\langle a \rangle$, pyramidal $\langle a \rangle$ and tensile twinning, were enough to get good agreement between experiment and simulation.

The systematic texture simulations of AZ31 conducted by Styczynski et al. [75] showed that the best agreement between simulated and experimental textures is obtained by considering basal, prismatic $\langle a \rangle$, pyramidal $\langle a + c \rangle$ and tensile twinning, which are the same than in [3, 2].

Yi et al. [86] also studied magnesium alloy AZ31 for understanding the relation between texture evolution and flow curves. The best concord was achieved using all three $\langle a \rangle$ deformation modes, basal, prismatic, pyramidal, as well as tensile twin and pyramidal $\langle a+c \rangle$.

As a resume, experimental and modeling investigations seem to show that the deformation mechanisms acting significantly in Mg and its alloys at low homologous temperature are still subjected to some discussions. But generally, the use of any $\langle a \rangle$ and an $\langle a + c \rangle$ non-basal slip system additionally to basal slip and tensile twinning seems to deliver satisfactory results in modeling. As a consequence, and since pyramidal $\langle a \rangle$ slip produce a strictly equivalent shape change than combined basal and prismatic $\langle a \rangle$ cross-slip, this system will not be considered in the present work, while basal $\langle a \rangle$, prismatic $\langle a \rangle$, tensile twinning on $\{10\bar{1}2\}$ and pyramidal $\langle a + c \rangle$ will, see Table 2.1.

Deformation Mode	Plane	Direction
Basal $\langle a \rangle$	$\{0001\}$	$\langle 11\bar{2}0 \rangle$
Prismatic $\langle a \rangle$	$\{1\bar{1}00\}$	$\langle 11\bar{2}0 \rangle$
Pyramidal $\langle a + c \rangle$	$\{11\bar{2}2\}$	$\langle 11\bar{2}3 \rangle$
Tensile twin	$\{10\bar{1}2\}$	$\langle 10\bar{1}1 \rangle$

Table 2.1: *Deformation modes considered in the present work, planes and directions are expressed in the Miller-Bravais coordinate system, see Figure 2.1*

Chapter 3

Modeling using Crystal Plasticity

3.1 Principle and History

Crystal plasticity aims on describing the plastic deformation of single crystals and polycrystals which results from shearing of specific crystallographic slip systems. In crystal plasticity models, the physical discrete events of slip are formulated into a mathematical continuum description. The schematic representation in Figure 3.1 shows a simplified correspondance between discrete dislocations motions and the continuum slip theory in an idealized two dimensionnal case.

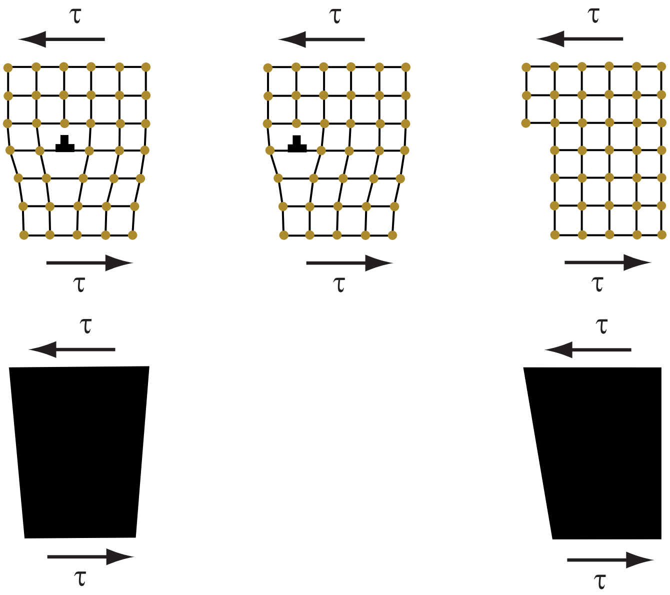

Figure 3.1: *Correspondance between discrete events of slip (above) and the continuum slip theory (below) in an idealized two dimensionnal case*

The description of macroscopic plastic strains in metal single crystals based on a physical description started with the work of Taylor [78, 77] and Schmid and Boas [70]. Plastic deformation in ductile crystals was found to result from dislocation motions on certain crystallographic slip systems when a critical value of shear stress is reached in these systems. The mathematical formulation of these discrete events into a continuum was developed by Hill [33], Teodosiu [80], Rice [66], Hill and Rice [34], and Mandel [54]. Micromechanical observations of crystal lattice defects as for example in Cottrell [21] or Seeger [71] motivate the need for a description of slip resistance, or slip hardening. In the case of multiple simultaneous slip the formulation of adapted constitutive equations for slip hardening is still subject to researches, see for example Kocks [46, 47], Peirce et al. [62], Bassani and Wu [11], Cuitiñio and Ortiz [22]. Algorithms for crystal plasticity models adapted to numerical calculations like the finite element method have been developed recently, by Peirce et al. [62], Needleman et al. [57], Cuitiñio and Ortiz [22], Anand and Kothari [5] as well as Miehe [55]. Complete descriptions about "crystal plasticity and evolution of polycrystalline microstructures" and "micromechanics of crystals and polycrystals" are given in Miehe and Schotte [56] and Asaro [7], respectively.

Over the years, different approaches for crystal plasticity have been developed which varie from the classical crystal plasticity framework established in the works mentioned above.
Following the work of Taylor [77], Taylor-type models for crystal plasticity assume that the strain distribution over the whole polycrystalline aggregate is homogeneous. Plastic strain at microscale is therefore identical to plastic strain at macroscale. This allows for computing stress and strain components for each grain separately and thus to save much computationnal time. Generally, in modelling deformation processes Taylor-type models give qualitative but not always quantitative satisfying predictions of texture evolution. This is due to the lack of interactions between the grains.
Self consistent models consist in assuming each grain embedded in a matrix which is attributed the mean mechanical properties of the surrounding polycrystalline aggregate. The first self consistant models were proposed by Kröner [49] and Hutchinson [39]. The model of Lebensohn and Tomé [50] may consider fully anisotropic crystalline behavior. Compared to classical crystal plasticity models, in such models the strains tend to be more accomodated through soft slip systems in grains which are well orientated for deformation.
Generalized continuum models aim to incorporate additionnal degrees of freedom in their constitutive equations compared to classical crystal plasticity models. This allows in accounting for size effects like the Hall-Petch effect, constrained plasticity in thin layer and around precipitates for example. These models fill the gap between dislocation dynamic methods and the classical crystal plasticity which is, at the same time, their limited range of application.

3.2 The Model Used in This Work

The model for crystal plasticity, which is described just after in this chapter, has been used in the present work in finite element simulations of single crystals and polycrystalline aggregates subjected to different loading hitories. Beside the numerous material parameters needed for calibrating the model, the reproduction of lattice crystallographic orientations and texture of polycrystalline aggregates is a key question for these simulations. Appendix A explains therefore how the crystals' crystallographic orientations are introduced into this model and especially how the texture of polycrystalline aggregates is reproduced. Please note that, in the following, no symbol is used to describe the scalar products in the mathematical description of the model.

3.2.1 Kinematic

The model of crystal plasticity used in this work employs the framework for classical crystal plasticity by Peirce et al. [62, 63] and Asaro [7, 8]. The numerical implementation in the finite element code ABAQUS is based on the user-material routine (UMAT) of Huang [37] extended to hexagonal structures. The lattice of a crystalline material undergoes elastic stretching, rotation and plastic deformation. The latter is assumed to arise solely from crystalline slip. As illustrated in Figure 3.2, the total deformation gradient $\mathbf{F}$ is decomposed as

$$\mathbf{F} = \mathbf{F}^{\star}\mathbf{F}^{p} \tag{3.1}$$

where $\mathbf{F}^p$ denotes plastic shear of the material to an intermediate reference configuration in which lattice orientation and spacing are the same as in the initial configuration, and $\mathbf{F}^{\star} = \mathbf{V}^{\star}\mathbf{R}^{\star}$ denotes stretching and rotation of the lattice. Superscript * always indicates the lattice part of the kinematic quantities in the following.

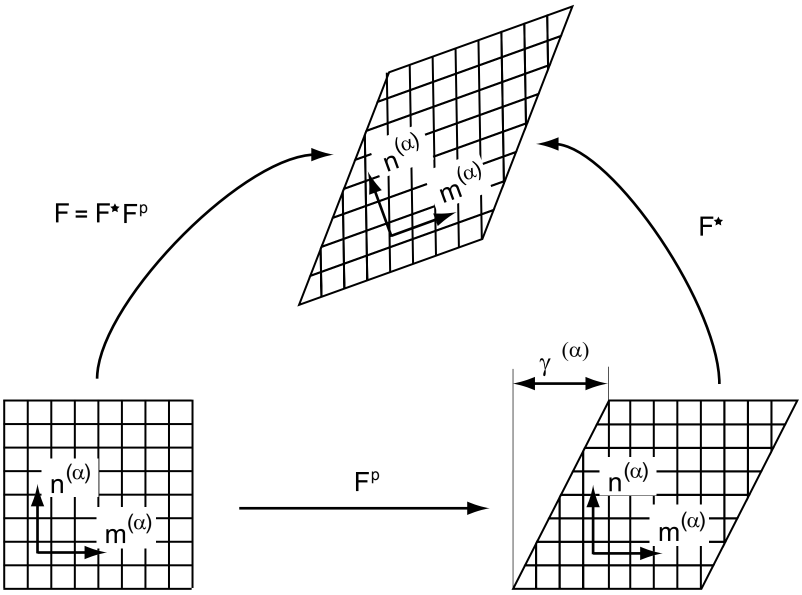

Figure 3.2: *Multiplicative decomposition of the deformation gradient* $\mathbf{F}$

The rate of change of $\mathbf{F}^p$ is related to the slip rate $\dot{\gamma}^{(\alpha)}$ of the α slip system by

$$\dot{\mathbf{F}}^{p}\dot{\mathbf{F}}^{p^{-1}} = \sum_{\alpha} \dot{\gamma}^{(\alpha)}\mathbf{m}^{(\alpha)} \otimes \mathbf{n}^{(\alpha)}, \tag{3.2}$$

where the sum ranges over all activated slips systems, and the unit vectors $\mathbf{m}^{(\alpha)}$, $\mathbf{n}^{(\alpha)}$ are the slip direction and the slip-plane normal, respectively, in both initial and intermediate reference configurations, which transform to

$$\mathbf{m}^{\star(\alpha)} = \mathbf{F}^{\star}\mathbf{m}^{(\alpha)}, \qquad \mathbf{n}^{\star(\alpha)} = \mathbf{n}^{(\alpha)}\mathbf{F}^{\star^{-1}} \tag{3.3}$$

in the current deformed configuration, where

$$\mathbf{n}^{\star(\alpha)}\mathbf{m}^{\star(\beta)} = \mathbf{n}^{(\alpha)}\mathbf{F}^{\star^{-1}}\mathbf{F}^{\star}\mathbf{m}^{(\beta)} = \mathbf{n}^{(\alpha)}\mathbf{m}^{(\beta)} = \delta_{\alpha\beta}. \tag{3.4}$$

The velocity gradient in the current configuration is given by

$$\mathbf{L} = \dot{\mathbf{F}}\mathbf{F}^{-1} = \mathbf{D} + \boldsymbol{\Omega}, \tag{3.5}$$

where the symmetric stretching rate, $\mathbf{D}$, and the skew vorticity or spin tensor, $\boldsymbol{\Omega}$, can be decomposed into lattice and plastic parts

$$\mathbf{D} = \mathbf{D}^{\star} + \mathbf{D}^{p}, \qquad \boldsymbol{\Omega} = \boldsymbol{\Omega}^{\star} + \boldsymbol{\Omega}^{p}, \tag{3.6}$$

with

$$\mathbf{D}^{\star} + \boldsymbol{\Omega}^{\star} = \dot{\mathbf{F}}^{\star}\mathbf{F}^{\star^{-1}}, \qquad \mathbf{D}^{p} + \boldsymbol{\Omega}^{p} = \sum_{\alpha} \dot{\gamma}^{(\alpha)}\mathbf{m}^{\star(\alpha)} \otimes \mathbf{n}^{\star(\alpha)}, \tag{3.7}$$

The elastic properties are assumed to be unaffected by slip, i.e. the stress is determined solely by $\mathbf{F}^{\star}$. Thus, the stretching rate, $\mathbf{D}$, is related to the Jaumann derivative of Cauchy's stress tensor, $\boldsymbol{\sigma}$, by

$$\overset{\nabla\star}{\boldsymbol{\sigma}} + \boldsymbol{\sigma}(\mathbb{I} : \mathbf{D}^{\star}) = \mathbb{C} : \mathbf{D}^{\star}, \tag{3.8}$$

where $\mathbb{C}$ is the fourth order tensor of elastic moduli and $\mathbb{I}$ the second order identity tensor. The Jaumann rate in equation 3.8 is the corotational stress rate on axes that rotate with the crystal lattice, which is related to the corotational stress rate on axes rotating with the material by

$$\overset{\nabla\star}{\boldsymbol{\sigma}} = \dot{\boldsymbol{\sigma}} - \boldsymbol{\Omega}^{\star}\boldsymbol{\sigma} + \boldsymbol{\sigma}\boldsymbol{\Omega}^{\star} = \overset{\nabla}{\boldsymbol{\sigma}} + (\boldsymbol{\Omega} - \boldsymbol{\Omega}^{\star})\boldsymbol{\sigma} - \boldsymbol{\sigma}(\boldsymbol{\Omega} - \boldsymbol{\Omega}^{\star}). \tag{3.9}$$

3.2.2 Constitutive Formulations

The crystalline slip is assumed to obey Schmid's law, i.e. the slip rate $\dot{\gamma}^{(\alpha)}$ depends on $\boldsymbol{\sigma}$ solely through Schmid's resolved shear stress,

$$\tau^{(\alpha)} = \mathbf{n}^{\star(\alpha)}\frac{\rho_0}{\rho}\boldsymbol{\sigma}\mathbf{m}^{\star(\alpha)}, \tag{3.10}$$

where ρ_0 and ρ are the mass densities in the reference and current states. The rate of change of the resolved shear stresses is

$$\dot{\tau}^{(\alpha)} = \mathbf{n}^{\star(\alpha)}\left[\overset{\nabla\star}{\boldsymbol{\sigma}} + \boldsymbol{\sigma}(\mathbb{I} : \mathbf{D}^{\star}) - \mathbf{D}^{\star}\boldsymbol{\sigma} + \boldsymbol{\sigma}\mathbf{D}^{\star}\right]\mathbf{m}^{\star(\alpha)}. \tag{3.11}$$

According to Peirce et al. [62], the constitutive equation of slip is assumed as a viscoplastic power law,

$$\frac{\dot{\gamma}^{(\alpha)}}{\dot{\gamma}_0^{(\alpha)}} = \left|\frac{\tau^{(\alpha)}}{\tau_Y^{(\alpha)}}\right|^n sign\left(\frac{\tau^{(\alpha)}}{\tau_Y^{(\alpha)}}\right), \tag{3.12}$$

where $\dot{\gamma}_0^{(\alpha)}$ is a reference strain rate, $\tau_Y^{(\alpha)}$ characterizes the current strength of the α slip system, and n is the rate sensitivity exponent. Strain hardening is characterized by the evolution of the strengths

$$\dot{\tau}_Y^{(\alpha)} = \sum_{\beta} h_{\alpha\beta}(\bar{\gamma})\dot{\gamma}^{(\alpha)}, \tag{3.13}$$

with $h_{\alpha\beta}$ being the self ($\alpha = \beta$) and latent ($\alpha \neq \beta$) hardening moduli depending on Taylor's cumulative shear strain on all slip systems,

$$\bar{\gamma} = \sum_{\alpha} \int_0^t |\dot{\gamma}^{(\alpha)}| d\tau. \tag{3.14}$$

Interactions of the different active slip systems is further defined assuming that

$$h_{\alpha\alpha} = h(\bar{\gamma}) \qquad \text{and} \qquad h_{\alpha\beta} = q_{\alpha\beta} h(\bar{\gamma}) \quad \text{for} \quad (\alpha \neq \beta), \tag{3.15}$$

so that the hardening law can be written as

$$\tau_Y^{(\alpha)} = \tau_0 + \int_0^t h(\bar{\gamma}) \left(\dot{\gamma}^{(\alpha)} + q_{\alpha\beta} \sum_{\alpha \neq \beta} \dot{\gamma}^{(\beta)} \right) d\tau \tag{3.16}$$

with $\tau_0 = \tau_Y^{(\alpha)}(0)$ as integration constant. Hardening parameters as well as the values of the interaction parameters $q_{\alpha\beta}$ have to be calibrated by a fitting procedure considering both, test results of single crystals as well as polycrystals.
Three different hardening laws are applied in this work, namely

- linear hardening

$$h(\bar{\gamma}) = h_0, \tag{3.17}$$

- Voce hardening

$$h(\bar{\gamma}) = h_0 \left(1 - \frac{\tau_0}{\tau_\infty}\right) exp\left(-\frac{h_0 \bar{\gamma}}{\tau_\infty}\right) \tag{3.18}$$

  with τ_∞ beeing the saturation stress,

- and particularly for deformation twinning

$$h(\bar{\gamma}) = \begin{cases} h_0 & \text{for} \quad \bar{\gamma} \leq \gamma_{ref} \\ h_0 \left(\dfrac{\bar{\gamma}}{\gamma_{ref}}\right)^{m-1} & \text{for} \quad \bar{\gamma} > \gamma_{ref}. \end{cases} \tag{3.19}$$

The integrated functions of equations 3.17, 3.18 and 3.19 presenting the different hardening characteristics used in this work are shown in Figure 3.3. The specific hardening law of equation 3.19 was assumed for deformation twinning in order to model the observed phenomenon of a sudden increase in stress due to saturation of twinning after a certain amount of deformation strain has been reached. This phenomenon is particularly well observed and discussed for the flow curves **E** and **F**, as well as **LS** and **TS** in [43, 44]. As developed earlier in this work twinning consists in a rotation of a finite domain of the crystal lattice. Lattice rotation due to twinning is not taken into account in the present framework of crystal plasticity. Hence, twinning is handled here as additional slip mechanism of the type $\{10\bar{1}2\}\langle 10\bar{1}1\rangle$ and the reorientation of crystallographic planes due to twinning is omitted. This way of representation for twinning assumes that, as twinning has saturated, further plastic deformation occurs only in the untwinned material. Furthermore, it is assumed that both, slip and twinning, can operate simultaneously at a material point where deformation twinning modeled as crystallographic slip is supposed to follow Schmid's law, see equations 3.12, 3.13 and 3.14. Its hardening law is assumed as in equation 3.19, and the polar character of tensile twinning, which was shown to be the main twinning mechanism active in magnesium, is taken into account with the restriction,

$$\tau_Y^{(\alpha)} \to \infty \qquad \text{for} \qquad \tau^{(\alpha)} \leq 0, \tag{3.20}$$

allowing only for extension of the c-orientation.

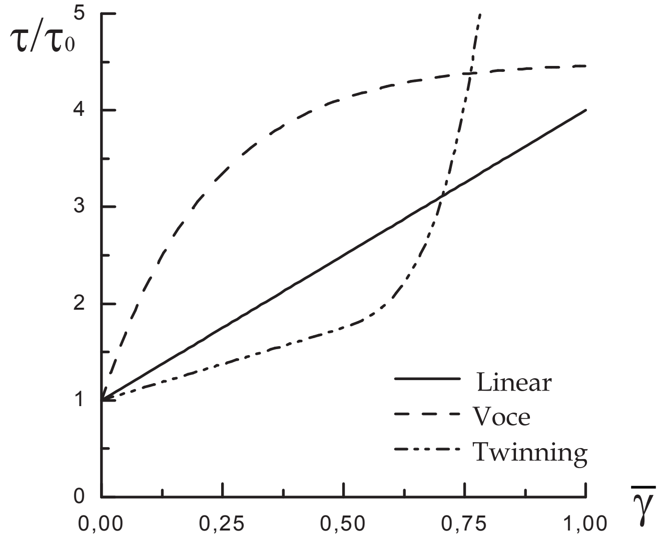

Figure 3.3: *Integrated functions of equations 3.17, 3.18 and 3.19 presenting the different hardening characteristics used in the following crystal plasticity calculations*

Chapter 4

Modeling using Phenomenological Yield Criteria

Models for crystal plasticity aim on describing mechanical mechanisms occuring at microscopic level, taking into account the crystallographic orientations of individual grains and the deformation modes by slip and twinning related to this orientation. These models require thus detailled information about deformation mechanisms and texture of the material considered. Taking these information into account in simulating the deformation behavior of components during fabrication processes for example, is extremely computational time consumming. In order to improve the design of industrial products in terms of costs and time, phenomenological models able to model mechanical behavior of a material at structural level are much more efficient tools. Due to the greater lengthscales of the considered components, in phenomenological models the material is considered as a continuum having homogeneous mechanical properties which may depend only on the direction in space, in the case of anisotropic materials. Such models are usually based on the concept of yield surface, which is well adapted to the continuum approach, and therefore appropriate to perform simulations of industrial applications in which large structures are generally considered. This chapter aims on introducing the concept of yield surface as well as the concepts of flow rule and hardening behavior related to it.

4.1 The Yield Surface Concept

The concept of a yield surface at a material point, point in the continuum, consists in the formulation of a scalar equation in a stress space of the Cauchy stress tensor. This equation aims on separating elastic and plastic deformation behavior of the material point and stress states inside the yield surface are elastic. This surface's equation may be formulated in a simple way as,

$$\Phi\big(\boldsymbol{\sigma}\big) - \Phi_0 = 0. \tag{4.1}$$

The term $\Phi\big(\boldsymbol{\sigma}\big)$ operating on the stress tensor, is the so called yield function and the term Φ_0 is a scalar limiting value of $\Phi\big(\boldsymbol{\sigma}\big)$, e.g. an initial yield strength. In the case of isotropic materials the yield function should not depend on the coordinate system in which it is expressed. For this reason, yield criteria of isotropic materials are generally expressed in terms of stress invariants. Most metals including Mg are insensitive to the hydrostatic pressure, denoted p, which is defined as,

$$p = -\sigma_m \qquad \text{where } \sigma_m \text{ is the mean stress,} \qquad \sigma_m = \frac{1}{3}(\sigma_{11} + \sigma_{22} + \sigma_{33}).$$

The first formulated yield condition was proposed by Tresca [82] and is insensitive to hydrostatic pressure. This yield criterion is satisfied when the maximum shear stress reaches a constant critical value σ_s. The shear stresses are written as functions of the principal stresses σ_I, σ_{II}, σ_{III}, which are themselves invariants. Finally this condition is expressed as,

$$max\left(\frac{|\sigma_I - \sigma_{II}|}{2}, \frac{|\sigma_{II} - \sigma_{III}|}{2}, \frac{|\sigma_{III} - \sigma_I|}{2}\right) - \sigma_s = 0 \tag{4.2}$$

where σ_s is the yield stress obtained from a simple shear test. Beside Tresca, the mostly used yield criterion for isotropic materials insensitive to hydrostatic pressure is the von Mises [83] one. This criterion is expressed as a function of the second invariant of the deviatoric stress tensor J_2 and the yield stress in uniaxial tension σ_Y as,

$$3J_2 - {\sigma_Y}^2 = 0 \tag{4.3}$$

or as a function of the stress components as,

$$\frac{1}{6}(\sigma_{22} - \sigma_{33})^2 + \frac{1}{6}(\sigma_{33} - \sigma_{11})^2 + \frac{1}{6}(\sigma_{11} - \sigma_{22})^2 + {\sigma_{12}}^2 + {\sigma_{23}}^2 + {\sigma_{13}}^2 - \frac{{\sigma_Y}^2}{3} = 0. \tag{4.4}$$

The von Mises and the Tresca criterion result in very similar yield locii as shown in Figure 4.1.

While the von Mises yield locus describes a circle in the deviatoric plane of the principal stress space, the Tresca yield locus describes a hexagon whose edges lie on the von Mises circle. Since both yield criteria are insensitive to hydrostatic pressure, the yield locii can be translated along the hydrostatic axis of vector $(1, 1, 1)$ such that the von Mises and Tresca yield surfaces represent finally an infinite cylinder with circle and hexagon basis, respectively, see Figure 4.1.

4.2 The Flow Rule Concept

The flow rule concept aims on linking stress and plastic strain components and thus completes the yield criterion in describing the plastic behavior of a material. In this concept the plastic strains are assumed to derive from a potential function called the plastic potential which consists in a scalar function of the form, $\psi = \psi(\boldsymbol{\sigma})$. The flow rule can then be expressed as,

$$\mathbf{D}^p = \dot{\lambda}\frac{\partial \psi}{\partial \boldsymbol{\sigma}}. \tag{4.5}$$

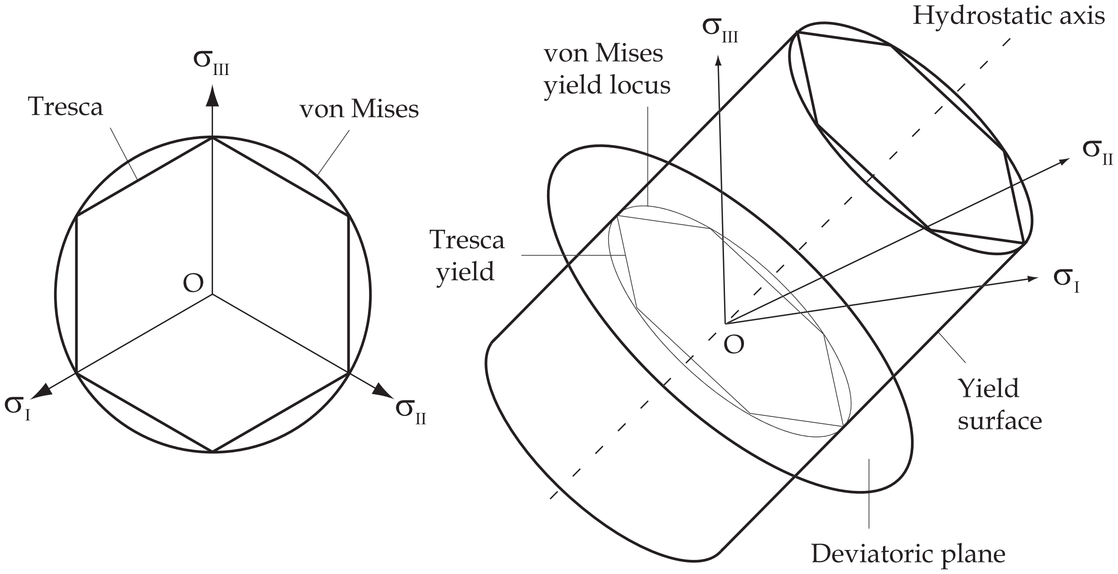

Figure 4.1: *Representation of Tresca and von Mises yield criteria in the space of principal stresses*

Here $\mathbf{D}^p$ is the tensor of plastic strain rates, $\dot{\lambda}$ is a positive scalar called plastic multiplier, and ψ is the plastic potential. In many materials and especially for most metals, the plastic potential ψ can be identified with the yield function Φ such that the flow rule is said associated. When Φ is defined insensitive to the hydrostatic stress, the condition of plastic incompressibility, $tr\big(\mathbf{D}^p\big) = 0$, is also satisfied by the flow relation which then writes:

$$\mathbf{D}^p = \dot{\lambda}\frac{\partial \Phi}{\partial \boldsymbol{\sigma}}. \tag{4.6}$$

This flow rule is also named normality rule because all components of the plastic strain rate tensor are normal, in the stress space, to the yield surface defined by Φ.
Combining the associated flow rule of equation 4.6 with a convex yield surface has been shown to be sufficient to satisfy Drucker's material stability postulate [25]. For this reason, an associated flow rule will be considered later in this work while convexity of the yield surface has to be ensured.

4.3 The Hardening Concept

For perfectly plastic materials, which present no hardening behavior, Φ_0 is constant and the yield surface shape and position are therefore invariant in the stress space during plastic deformation. In such cases, the stress state of a material point may simply move on the invariant yield surface during plastic deformation. This situation is named neutral loading. Nevertheless, in most cases metals do not behave as perfectly plastic material but harden as plastic strain increases. A hardening behavior, which is briefly introduced and explained in Figure 2.3 of section 2.2 for a uniaxial tension case, implies changes for the yield surface. Loading is therefore not neutral anymore. Hardening of a material is often taken into account in adding internal variables to the yield function Φ which may then be written as,

$$\Phi\Big(\boldsymbol{\sigma}, \mathbf{A}\big(\mathbf{E}^p\big), k\big(\mathbf{E}^p\big)\Big), \tag{4.7}$$

where $\mathbf{A}$ is a second order tensorial hardening parameter depending on $\mathbf{E}^p$, the plastic part of the strain tensor $\mathbf{E}$, and k is a monotonically increasing scalar function of $\mathbf{E}^p$. The hardening parameters $\mathbf{A}$ and k are variables that reflect the history of plastic deformation and inform about the actual state of the yield surface after kinematic and isotropic hardening, respectively. Indeed, two strain-hardening postulates are commonly used to describe the evolution of a yield surface in the stress space, namely isotropic and kinematic hardening. Figure 4.2 illustrates the changes in the yield surface with regard to both postulates.

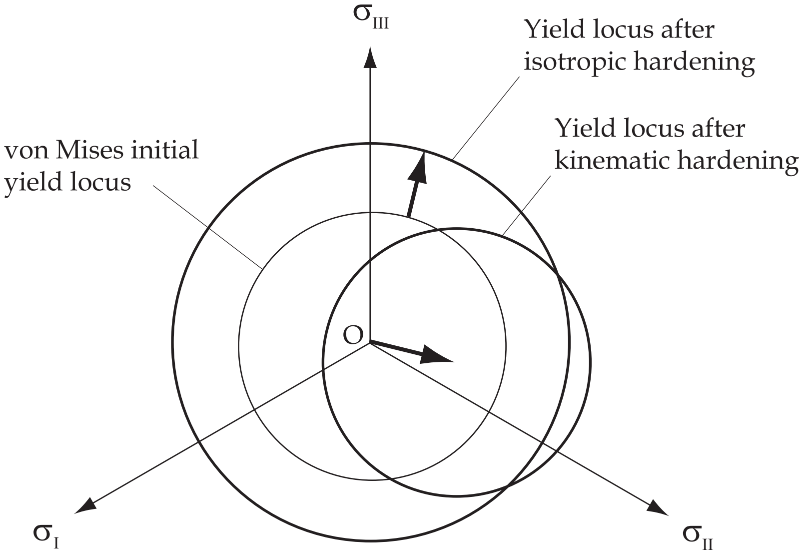

Figure 4.2: *Evolution of von Mises yield locus in the space of principal stresses for isotropic and kinematic hardening*

While isotropic hardening assumes uniform expansion without translation of the yield surface in the stress space, kinematic hardening assumes translation without expansion of the yield surface in the stress space, as plastic strain increases. In both strain-hardening models the yield surface shape remains unchanged during strain-hardening as shown on figure 4.2. Indeed, the von Mises yield locus remains a circle after any of both tranformations. Isotropic hardening is the most widely used strain-hardening concept and kinematic hardening, combined with isotropic hardening or not, is often introduced in material models while cyclic loadings are considered. Indeed, kinematic hardening allows for modeling the Bauschinger effect [12] for example.

Chapter 5

Crystal Plasticity: Channel Die Tests

5.1 Tests Set Up and Finite Element Models

In order to allow for the observation of deformation mechanisms other than the easy glide basal slip and tensile twinning, Wonsiewicz and Backhofen [85] as well as Kelley and Hosford [43, 44] performed channel die tests on pure magnesium single crystals [85, 43] and on pure magnesium samples cut out of a rolled plate [44]. The authors used a steel channel die experiment, see Figure 5.1a, in which small cuboid samples (approximately $6 \times 10 \times 13$ and $6 \times 13 \times 6$ mm^3) were compressed in one direction, while the second direction was constrained in displacement (rigid die) and the third one was free. The finite element model of this test is shown in Figure 5.1b for a polycrystalline aggregate. By changing the initial orientation of both single crystal and polycrystalline samples, different deformation modes can be activated. The experimental results of Kelley and Hosford [43, 44] are used here as a reference.

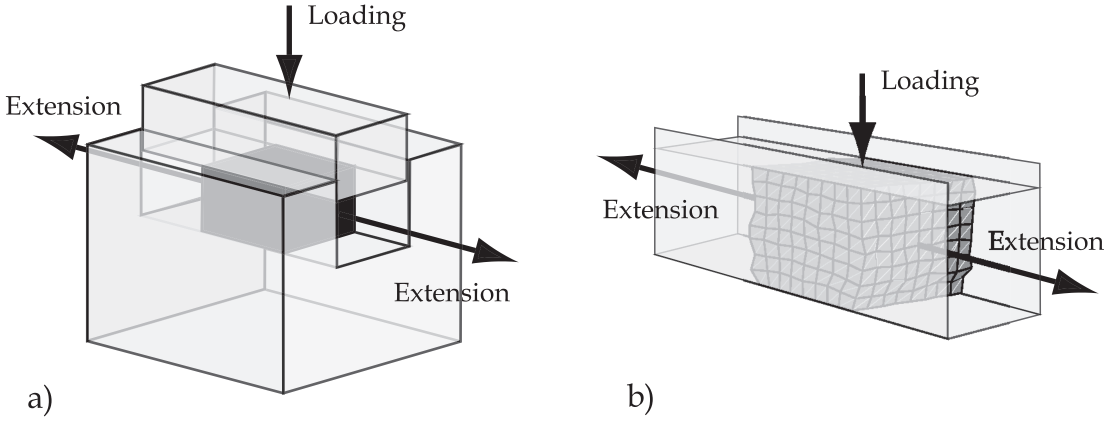

Figure 5.1: *Channel die test scheme a) and finite element model b)*

In the following, the loading direction is denoted as (1) and the constraint direction as (2). Table 5.1 gives an overview on the respective crystallograhic orientations for the case of the single crystal. The orientations with respect to compression loading and applied constraint for the polycrystalline case are indicated by two of the letters L (longitudinal or rolling), T (transverse) and S (short transverse or thickness), where the first letter denotes the loading direction and the second the extension direction.

Orientation	Loading (1)	Constraint (2)
A	$\langle 0001\rangle$	$\langle 10\bar{1}0\rangle$
B	$\langle 0001\rangle$	$\langle 1\bar{2}10\rangle$
C	$\langle 10\bar{1}0\rangle$	$\langle 0001\rangle$
D	$\langle 1\bar{2}10\rangle$	$\langle 0001\rangle$
E	$\langle 10\bar{1}0\rangle$	$\langle 1\bar{2}10\rangle$
F	$\langle 1\bar{2}10\rangle$	$\langle 10\bar{1}0\rangle$
G	$\langle 0001\rangle$ at 45 °	$\langle 10\bar{1}0\rangle$

Table 5.1: *Crystallographic orientations used in the channel die tests on single crystals by Kelley and Hosford [43]*

Simulations of single crystal and polycrystalline aggregates presented in the following have been realised in the framework of the finite element method using 8-node 3D elements. An equivalent discretisation has been chosen for single crystals and polycrystals, a crystal is described by one single finite element. Consequently, in a polycrystalline specimen the number of modeled grains corresponds to the number of finite elements. A representative volume element (RVE) has to consist of a sufficient large number of grains. In the following, $8 \times 8 \times 8$ grains are considered in the RVE, each represented by an 8-node brick element having its individual crystallographic orientation.

The detailled investigation presented in [23] concentrated on the effect of discretisation onto the mechanical response of RVEs made of an hcp material. It was found, within others, that 100 crystallographic orientations are enough to describe well the plastic anisotropy of the considered aggregate. The size of the RVE used in this work is thus satisfying. Another conclusion of this investigation [23] is that 27 integration points per finite element is sufficient to predict macroscopic stress-strain curves but not intragranular heterogeneities. In this work focus is made on predicting macroscopic stress-strain curves and the 8-node 3D element, which have only 8 integration points, have been chosen nevertheless in order to reduce computationnal time.

The $8 \times 8 \times 8 = 512$ individual orientations used in the simulations of the channel die test, and representing the experimental Mg rolled plate texture of Figure 5.2a, are displayed in Figure 5.2b. On these pole figures one can recognize that the measured distribution of basal planes is strongly orientated parallel to the thickness direction of the plate, with a deviation slightly higher around rolling than around transverse direction.

The die and the loading stamp, shown in Figure 5.1b, are modeled by rigid surfaces and friction between the sample and the rigid surfaces is accounted for, assuming a Coulomb friction coefficient of 0.05 for all tests. In case of the polycrystalline specimen, surfaces in extension direction have not been constrained. All simulations assume isotropic elasticity with Young's modulus $E = 45000$ MPa and Poisson ratio $\nu = 0.3$. Since experiments have been performed with quasistatic loading, the strain rate sensitivity exponent n appearing in equation 3.12 is put equal to 50, making the simulations almost rate independent. The reference strain rate for each slip system, $\dot{\gamma}_0^{(\alpha)}$, is chosen to be compatible with the time scale in the finite element simulations, and set to 10^{-3}.

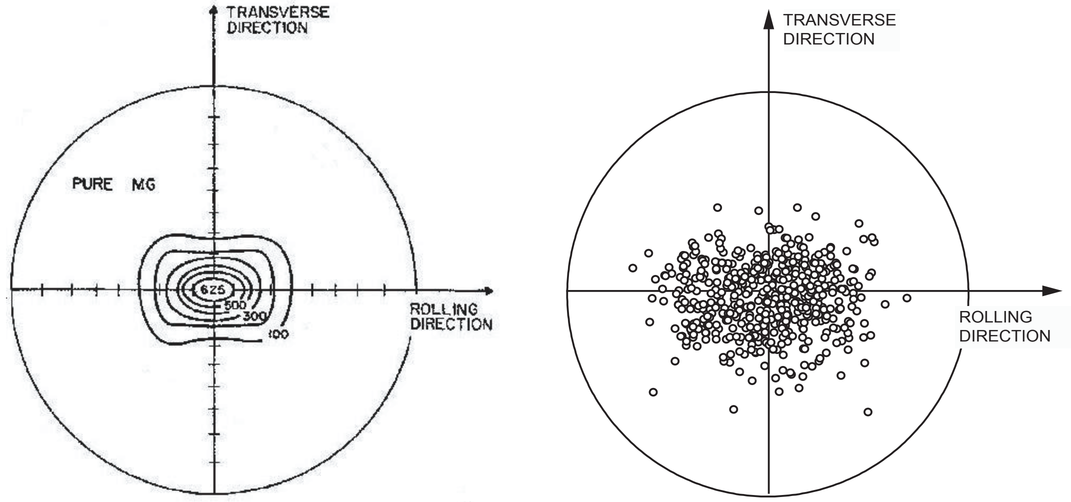

Figure 5.2: *(left) Experimental [44] and (right) simulated* (0001) *pole figures of a pure magnesium rolled plate sample*

In order to evaluate the mechanical response of single and polycrystals, the following definitions of true stresses and true (logarithmic) strains are respectively used,

$$\epsilon_{11} = \left\| ln\left(\frac{l^0_{11} + \Delta l_{11}}{l^0_{11}}\right)\right\| = \left\| ln\left(1 + \frac{\Delta l_{11}}{l^0_{11}}\right)\right\|, \tag{5.1}$$

$$\sigma_{11} = \frac{f}{A_0} F\left(1 + \frac{\Delta l_{11}}{l^0_{11}}\right). \tag{5.2}$$

Here, l^0_{11} and A_0 are the RVE's original length in loading direction and original section with regard to loading direction, respectively. F denotes the absolute value of the load and $f = 0.89$ is the friction correction coefficient introduced by Kelley and Hosford [43, 44]. The above expression for true stresses is obtained by assuming constant volume of the RVE during plastic deformation.

5.2 Identification of Material Parameters for the Crystal Plasticity Model

The determination of the parameters required in a model is generally a complex task. Their identification usually requires solving inverse problems because numerical simulations are calibrated to test data defined as reference. This task becomes especially complicated as the number of parameters to be identified is high, which is often the case in today developed material models, like in the present case. Various procedure exist nevertheless in order to solve this problem, starting from manual fitting, going to neural networks, in passing through trial and error, see the review articles [53, 15].

The constitutive model for crystal plasticity presented in chapter 3 requires three types of parameters per deformation mode α considered, the material constants for isotropic elasticity (Young's modulus and Poisson's ratio) excepted. These parameter types are,

- 2 parameters for the viscoplastic law, $\dot{\gamma}_0^{(\alpha)}$ and n, see equation 3.12,
- between 2 and 4 hardening parameters depending on the respective hardening law, τ_0, τ_∞, h_0, γ_{ref}, m, see equations 3.17, 3.18 and 3.19,
- parameters of latent hardening describing the interaction between the various deformation modes considered, $q_{\alpha\beta}$, see equation 3.16.

Regarding the numerous parameters to be determined, lots of fundamental questions, like the uniqueness of a parameter set, the sensitivity of the mechanical response to variations of these parameters and the design of appropriate tests capable of identifiing all or certain model parameters, are posed. None of these questions are answered here, as the focus is on the performance of the model and as test data have been taken from literature.
Based on these data, parameter identification has been realized here as a systematic trial and error procedure, since optimization methods were found inappropriate due to their lack of any physical background. The parameter identification required thus high expertise and insight knowledge of constitutive theories as well as experimental mechanics, and the resulting parameter set cannot claim to be the best possible fit.
For simplification, it has been assumed that all deformation modes belonging to the same basic mechanism have identical direct hardening parameters, and identical latent hardening parameters with respect to deformation modes belonging to a different basic mechanism. The four basic mechanisms are basal slip, prismatic slip, pyramidal slip and tensile twinning. Linear hardening of equation 3.17, with two parameters τ_0 and h_0, is assumed for basal slip. Voce hardening of equation 3.18, with three parameters τ_0, τ_∞ and h_0, is assumed for prismatic and pyramidal slip. And the combination of linear, τ_0 and h_0, and power law hardening, γ_{ref} and m, of equation 3.19 is assumed for tensile twinning. These assumptions are motivated by the deformation behavior observed in the tests, see discussion below. Finally, this adds up to $2 + 2 \times 3 + 4 = 12$ parameters for direct hardening to be calibrated, see Table 5.2.

	Basal $\langle a \rangle$	Prismatic $\langle a \rangle$	Pyramidal $\langle a+c \rangle$	Twinning
hardening law	equation 3.17	equation 3.18	equation 3.18	equation 3.19
τ_0 [MPa]	1	20	40	5
τ_∞ [MPa]	–	150	260	–
h_0 [MPa]	10	7500	7500	200
γ_{ref}	–	–	–	0.11
m	–	–	–	10

Table 5.2: *Direct hardening parameters, calibrated using experimental data of Kelley and Hosford [43, 44]*

Latent hardening is described by $4 \times 4 = 16$ interaction parameters $q_{\alpha\beta}$ to be calibrated, see Table 5.3. The material parameters of Tables 5.2 and 5.3 have been determined by

fitting simulation results to the test data of Kelley and Hosford [43, 44], namely channel die tests on single crystals of orientations **A** to **G**, see Table 5.1, and on specimens of orientations **LT**, **LS**, **TL**, **TS**, **SL**, **ST**, cut out from a textured rolled plate.
In the single crystal tests different deformation modes are activated depending on the respective crystallographic orientations of specimens.

β α	Basal $\langle a\rangle$	Prismatic $\langle a\rangle$	Pyramidal $\langle a+c\rangle$	Twinning
Basal $\langle a\rangle$	$q_{\alpha\beta}=0.2$	$q_{\alpha\beta}=0.5$	$q_{\alpha\beta}=0.5$	$q_{\alpha\beta}=0.5$
Prismatic $\langle a\rangle$	$q_{\alpha\beta}=0.2$	$q_{\alpha\beta}=0.2$	$q_{\alpha\beta}=0.2$	$q_{\alpha\beta}=0.5$
Pyramidal $\langle a+c\rangle$	$q_{\alpha\beta}=1.$	$q_{\alpha\beta}=1.$	$q_{\alpha\beta}=0.2$	$q_{\alpha\beta}=0.25$
Tensile twinning	$q_{\alpha\beta}=1.$	$q_{\alpha\beta}=1.$	$q_{\alpha\beta}=0.2$	$q_{\alpha\beta}=0.2$

Table 5.3: *Interaction (latent hardening) parameters, $q_{\alpha\beta}$, calibrated using experimental data of Kelley and Hosford [43, 44]*

This allows for a selective identification of the hardening parameters for a particular familly of deformation modes, provided that the respective mechanism is exclusively activated in the model. This requires that parameters for latent hardening have values different from zero. The actual values of the latent hardening parameters, in Table 5.3, cannot be concluded from the single crystal tests alone, but call for the polycrystal tests results. The discussion of the simulation results in next section will elucidate this more clearly.

5.3 Channel Die Tests of Mg Single Crystals and Polycrystals

Due to the reduced number of integration points used in the following simulations and the merely qualitative mapping of the texture, only approximate predictions of the specimens' deformation behavior while subjected to channel die tests can be expected.
A comparison of simulation and test results for single crystals of orientations **A** to **G**, see Table 5.1, is shown in Figure 5.3. Beside a general qualitative agreement between experimental and simulated results, the simulations capture the following specific features:

- Nearly identical stress-strain curves with high yield stress and strong but saturating hardening for orientations **A** and **B**, where the loading direction is $\langle 0001\rangle$;

- Nearly identical stress-strain curves with (compared to **A** and **B**) lower yield stress for orientations **C** and **D**, where the constraint direction is $\langle 0001\rangle$;

- Anomalous hardening behavior of orientations **E** and **F** with relatively low yield stress and almost no hardening at strains smaller than 0.06, followed by a sudden increase in stress,

- Saturation stress of orientation **E** exceeding that of **A** and **B**.

- Saturation stress of orientation **F** about that of **C** and **D**.
- Very low stress level for orientation **G**.

The simulated stress increase in orientation **F** is delayed compared to that obtained in the tests. As the simulations aimed at a unique set of model parameters, this deviation between test results and model predictions has been accepted. Note also, that the occurrence of stress rising for orientation **E** is not unambiguous in the tests, either. Considering the general assumptions made with respect to the hardening laws and the considerably large number of hardening parameters summarized in Table 5.2, the accordance between test and simulation results is considered as quite good.

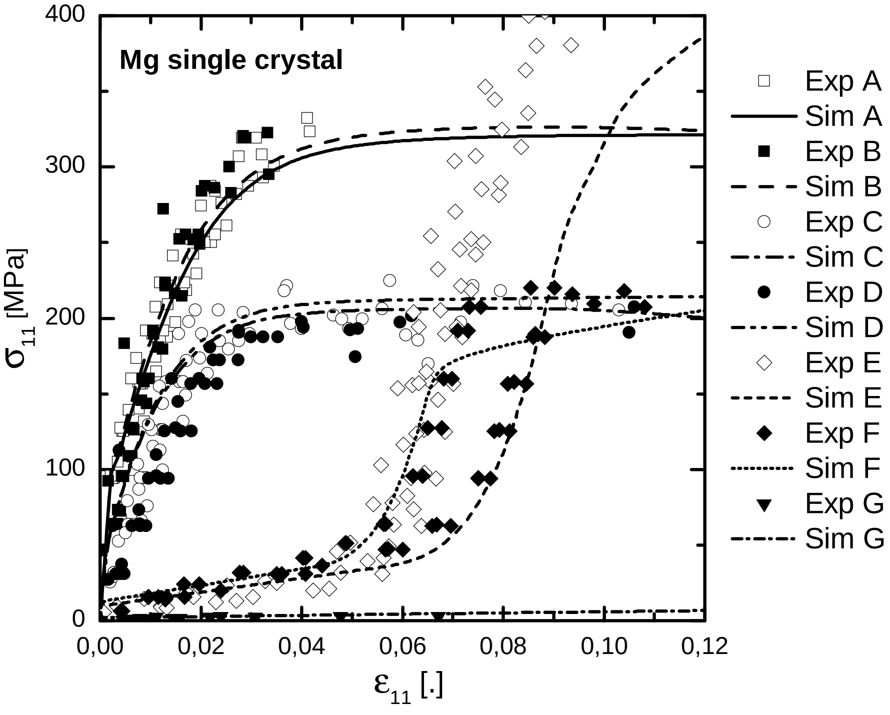

Figure 5.3: *Channel die tests of pure Mg single crystal, tests (Kelley and Hosford [43]) and simulations with parameter set of Tables 5.2 and 5.3*

The numerical simulations allow also for an analysis of the mechanisms causing the deformation of the single crystal samples. Figure 5.4 shows the evolution of the relative activities of the 4 deformation modes considered with increasing strain for each test. Relative activity describes the contribution of a specific deformation mode to the total plastic strain increment. It is calculated with respect to the increase of deformation,

$$\text{activity} = \frac{\gamma_{j+1}^{(\alpha)} - \gamma_{j-1}^{(\alpha)}}{\sum_\alpha \gamma_{j+1}^{(\alpha)} - \sum_\alpha \gamma_{j-1}^{(\alpha)}}, \tag{5.3}$$

providing information on the actual state of the respective mechanism.

Assuming non-zero values for the latent hardening parameters, the activation of the deformation modes for the different orientations occurs selectively. Only curves **A** and **B** show more than one family of mechanisms acting simultaneously, namely prismatic and pyramidal slip. Curves **C** and **D** are dominated by prismatic slip and curve **G** by basal slip over the whole range of strain. For orientations **E** and **F**, which favor plastic deformation resulting in an elongation of the c-axis, the transition from twinning to pyramidal slip occurs within a very small range of strains.

Because of its low critical resolved shear stress (CRSS) τ_0, tensile twinning is easily activated, and as saturation according to the power law 3.19 occurs, elastic deformation increases the stresses until the CRSS of pyramidal glide is reached, which explains the sudden increase of stresses at about 0.06 strain in Figure 5.5. This selectivity in the activation of slip mechanisms facilitates an efficient determination of the CRSS and the hardening parameter values of the different slip systems.

The comparison of Kelley and Hosford's [43, 44] channel die tests on polycrystalline samples with orientations **LT**, **LS**, **TL**, **TS**, **SL**, **ST**, cut out of Mg rolled plates with the simulation results is depicted in Figure 5.5. The two letters denote the orientation with respect to the loading and the direction of the channel die, respectively; L is the longitudinal or rolling direction, T the transverse and S the short transverse or thickness direction. The general trend is well reproduced for all curves except for curve **LT** where hardening is too small compared to the experimental data.

Due to the rolling process, the c-axes of the grains are orientated approximately parallel to the thickness direction of the plate with a slightly higher deviation in rolling than in transverse direction. This pronounced texture results in some qualitative similarities, of the flow curves between single crystals, Figure 5.3, and polycrystals, Figure 5.5. Polycrystals of orientations **LT**, **TL**, **ST**, **SL** show a monotonous hardening as the single crystals of orientations **A**, **B**, **C**, **D**. Those of orientations **TS** and **LS** exhibit the same striking hardening behavior as the single crystals of orientations **E** and **F**, namely relatively low yield stresses and little hardening at strains smaller than 0.04, followed by a sudden increase in stress.

Some differences of the hardening behavior of the polycrystals to that of single crystals are worth mentioning, however. The texture difference between the L and T orientation of the polycrystals is minor, see Figure 5.2, which levels the differences between the respective curves in Figure 5.5. The saturation stresses reached in the polycrystal specimens of orientations **ST** and **SL** are lower than those of the single crystals of orientations **A**, **B**, **C** and **D**, respectively, and the differences in the stresses of **LS** and **TS** are smaller than those between **E** and **F**. The curves **A**, **B**, **C**, **D** in Figure 5.3 saturate, whereas the curves **LT** and **TL** in Figure 5.5 do not. The specific shapes of the flow curves can be understood by the analysis of activated slip systems displayed in Figure 5.6 and are discussed below.

Despite the qualitative similarities in the hardening behavior between single crystals and textured polycrystals, the test data from polycrystals have great importance for the calibration of the material parameters, particularly the latent hardening parameters, $q_{\alpha\beta}$. Indeed, due to the varying orientations of grains in the RVE, more than one deformation mode has to be activated at the same time. This is manifested by Figure 5.6, which shows the "integral" activity of the respective slip systems in the RVE. The above statement even holds on the level of a material point, where (different from the single crystal case) several slip mechanism are active simultaneously. Hence, the latent hardening parameters affect the macroscopic response of the sample significantly and have to be identified from

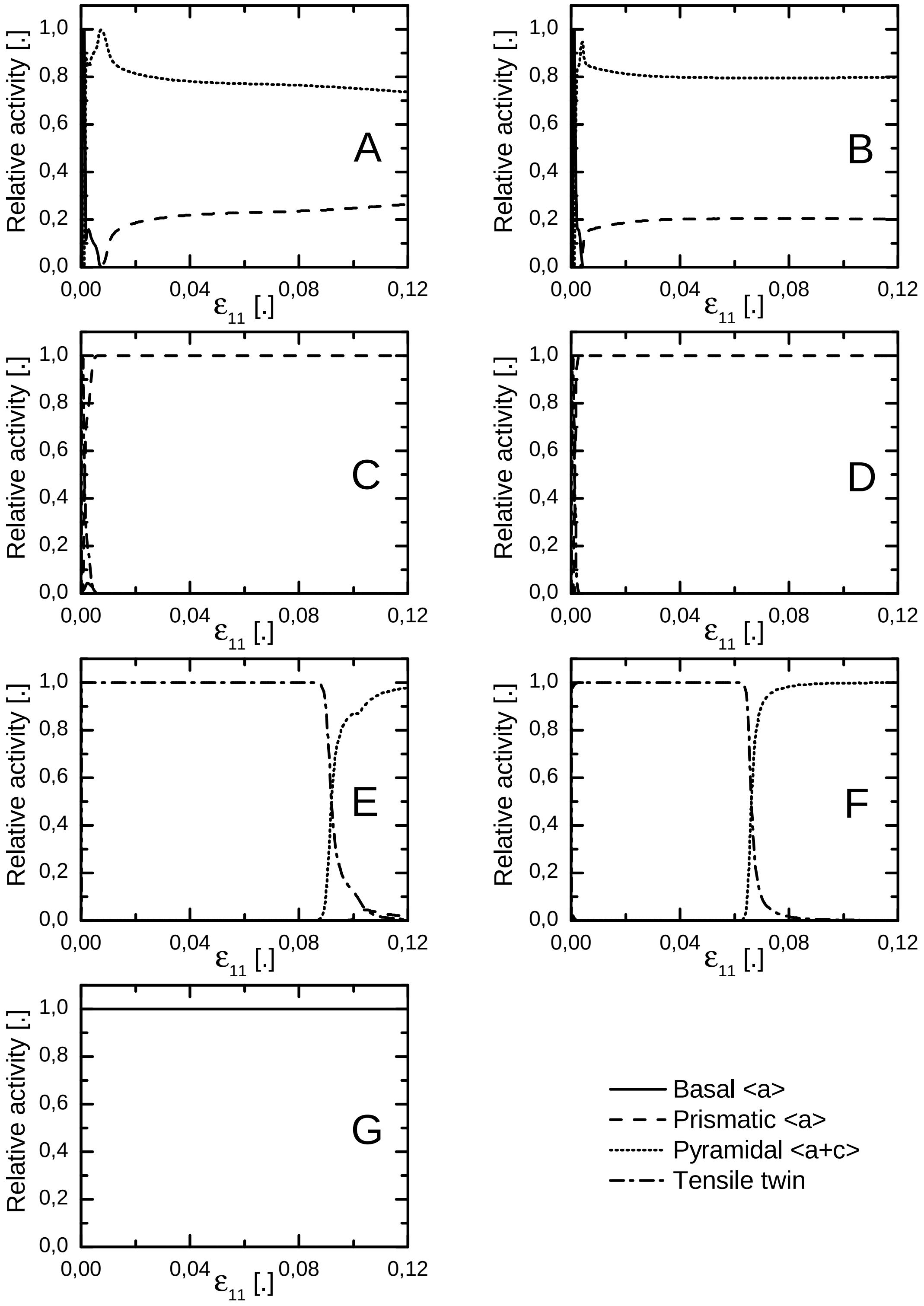

Figure 5.4: *Deformation modes' relative activity depending on the initial crystallographic orientation in simulated channel die tests of Mg single crystals*

the tests on polycrystals rather than on single crystals.

The relative activation of slip systems shown in Figure 5.6 helps in understanding the flow

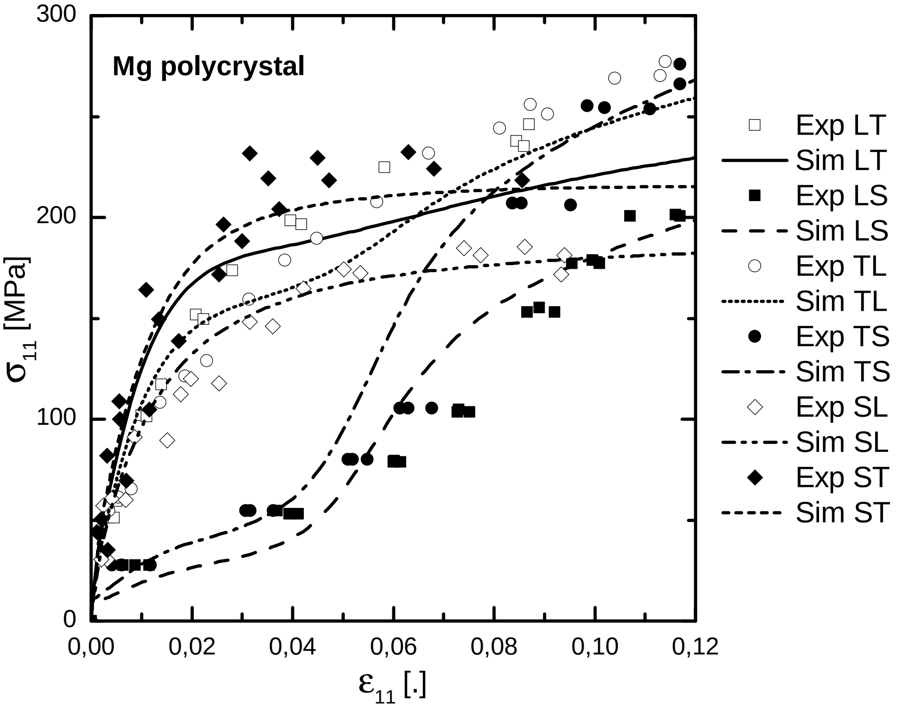

Figure 5.5: *Channel die tests of textured Mg rolled plate material, tests (Kelley and Hosford [43]) and simulations with parameter set of Tables 5.2 and 5.3*

curves of Figure 5.5. In the specimens of orientations **LT** and **TL**, about 60% of the plastic deformation results from prismatic slip with Voce hardening ($\tau_0 = 20$ MPa, $\tau_\infty = 150$ MPa), nearly 30% from basal slip with linear hardening ($\tau_0 = 1$ MPa). For the specimens of orientations **SL** and **ST**, pyramidal (Voce hardening, $\tau_0 = 40$ MPa, $\tau_\infty = 260$ MPa) and basal slip (linear hardening, $\tau_0 = 1$ MPa) contribute nearly equally by about 40% and prismatic slip (Voce hardening, $\tau_0 = 20$ MPa, $\tau_\infty = 150$ MPa) by about 20%. The low yield strength and hardening for the orientations **LS** and **TS** is due to the activation of tensile twinning ($\tau_0 = 5$ MPa), which contributes to the plastic deformation by about 40%, and the sudden increase of stresses beyond 0.05 strain results from the saturation of twinning going along with the activation of pyramidal slip.

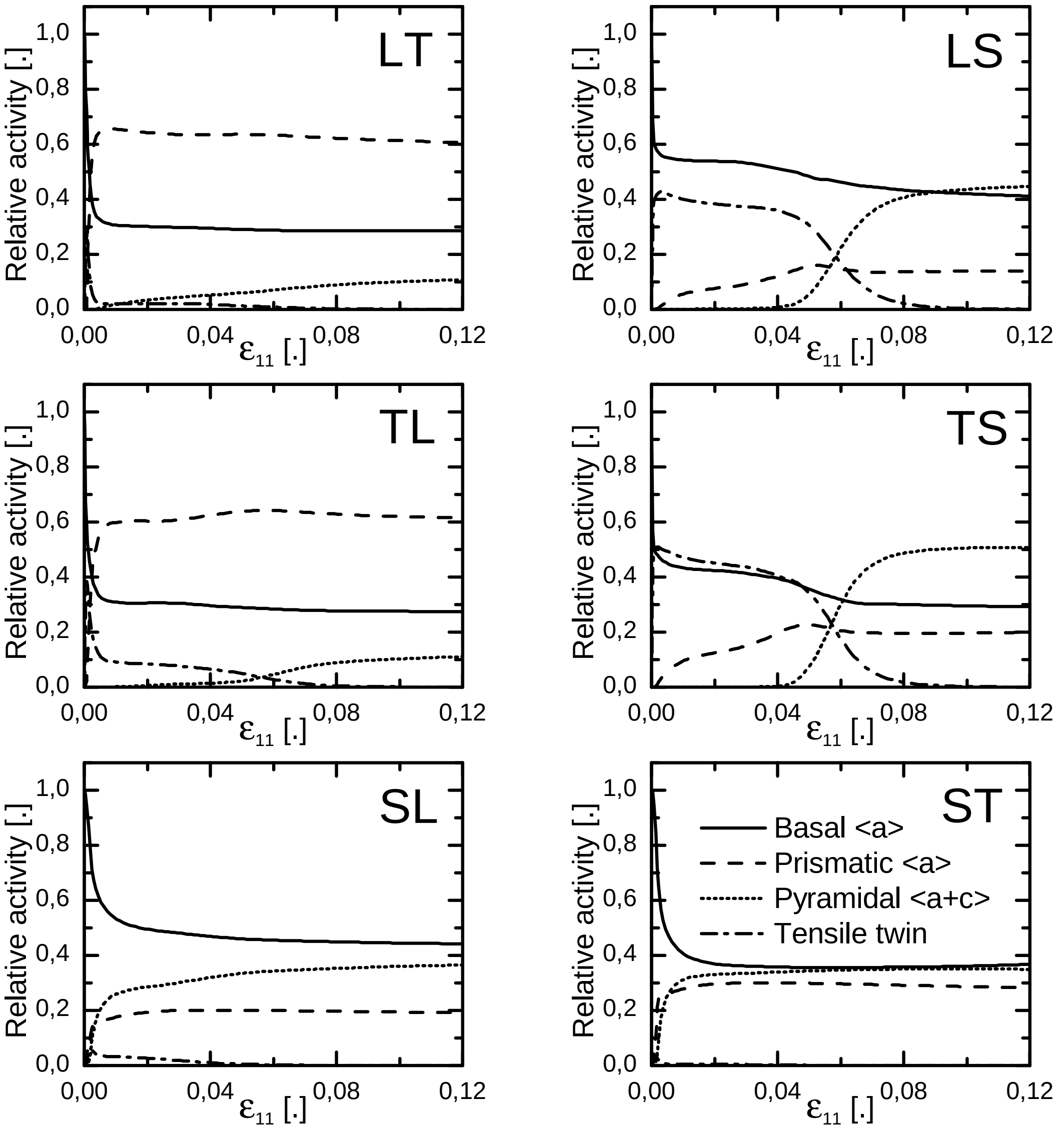

Figure 5.6: *Deformation modes' relative activity depending on the initial crystallographic orientation in simulated channel die tests of textured Mg rolled plate samples*

Chapter 6

Crystal Plasticity: Mechanical Properties of Extruded Rods

In the previous chapter all material parameters necessary for the crystal plasticity model used in this work have been calibrated with the help of channel die tests of Mg single crystals and polycrystalline aggregates out of rolled plates. In this chapter the significance of the calibrated material parameters is checked by performing uniaxial tension and compression tests on a virtual material with texture different than rolled plate. The virtual material chosen is made of Mg crystals and represents a typical extruded rod texture. Extruded rods out of magnesium alloys show a strong yielding asymmetry in tension and compression along the extrusion direction, see [51, 73, 45, 26, 27] and Figure 6.1. A similar mechanical behavior of the virtual material is expected which would confirm that the material parameters identified are somehow realistic.

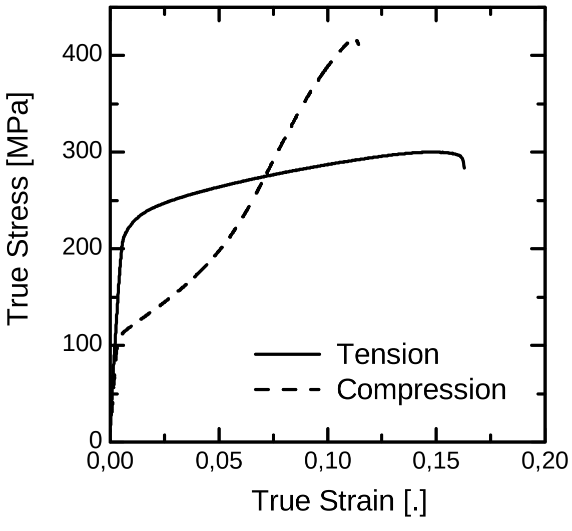

Figure 6.1: *Experimental results of the mechanical behavior, for uniaxial tension and compression test in extrusion direction, of an extruded AZ31 rod. Data: Bohlen J., private communication, GKSS Research Centre, Geesthacht, and published in [51]*

6.1 Finite Element Model of Uniaxial Tension and Compression Tests

The finite element model and the extruded rod texture which are used in the simulations of uniaxial tension and compression tests are displayed in Figure 6.2. The transfer from the micro to the macroscale is performed here, as in previous chapter, by means of representative volume elements (RVEs). As in the previous chapter each grain is attributed a specific crystallographic orientation and is described by a single 8-node brick finite element, and $8 \times 8 \times 8$ grains constitute the RVE, see Figure 6.2. Differently from the RVEs of previous chapter, additional periodic boundary conditions are considered to ensure the microstructure's periodicity.

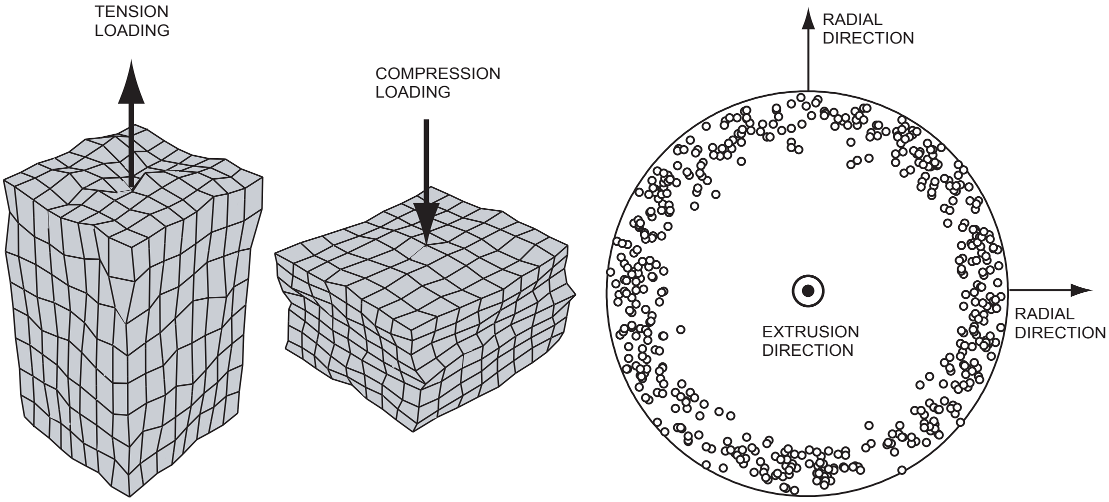

Figure 6.2: *Finite element model of uniaxial and compression tests (left) and typical (0001) pole figure of an Mg alloy extruded rod (right)*

The texture of extruded rods made out of magnesium and magnesium alloys typically shows the c-axis of the hexagonal structure to be orientated in radial direction of the rod, see for example [73, 45, 26]. The virtually generated texture of an extruded rod, illustrated in the (0001) pole figure of Figure 6.2, shows therefore strong preferred crystallographic orientations with c-axis in radial direction.

6.2 Extruded Rods Subjected to Uniaxial Tension and Compression Tests

Figure 6.3 displays the flow curves (**EDt**, **EDc**, **RDt** and **RDc**) of extruded Mg rods subjected to tensile and compression tests in both extrusion and radial direction. The stress-strain curves noted **EDt** and **EDc** in Figure 6.3, which correspond to tension and compression tests in extrusion direction, respectively, show very similar behavior than experimentaly observed. Indeed, this behavior is very comparable to the experimental flow curves for tensile and compression tests in extrusion direction of rods made of Mg and AZ31B which are presented in [27, 73], respectively. The flow curves **EDt** and **EDc** in Figure 6.3 show an important difference in yield stress (σ_Y), the ratio ${}^{EDt}\sigma_Y\ /{}^{EDc}\sigma_Y$ being almost two. The yield stress of **RDt** and **RDc** is also much different and interestingly, in this configuration, the yield stress in compression ${}^{RDc}\sigma_Y$ is higher than the tension one ${}^{RDt}\sigma_Y$. While the yield stress of **EDt** is relatively high compared to **EDc**, **RDt** and **RDc**, its hardening is very low above 0.025 true strain compared to the other curves. The hardening behaviors of **EDc** and **RDt** consisting in a low hardening rate in the first few percents of deformation and a sudden rapid increase after 0.05 strain recall that of the flow curves **E**, **F**, **LS** and **TS** observed in the channel die tests of previous chapter.

The slope of the macroscopically observed linear elastic behavior for all stress-strain curves of Figure 6.3 is different. Moreover, for all curves, this slope is different from Young's modulus $E = 45000$ MPa introduced in the calculations, where isotropic elasticity was considered. Non negligible plastic behavior of single grains occurs therefore already far below the observed macroscopic yield stresses affecting thus the slope of the macroscopically observed elastic behavior.

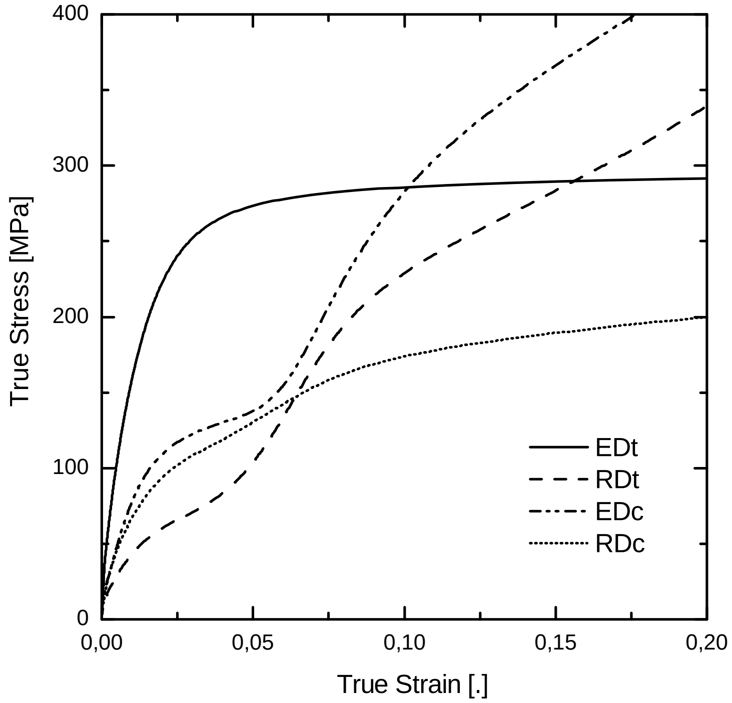

Figure 6.3: *Flow curves of extruded Mg rods, with texture shown in Figure 6.2, for uniaxial tension and compression tests in extrusion (**EDt**, **EDc**) and radial direction (**RDt**, **RDc**), respectively*

Explanations for such unusual mechanical behaviors may be found in analysing the relative contribution of the 4 families of deformation modes considered to the overall plastic deformation. In Figure 6.4, which allows for such an analysis, the term relative activity indicates the contribution of a specific deformation mode to the plastic strain increment, as the latter is set to 1. Figure 6.4 reveals for example that mechanical twinning is active in the three cases **EDc**, **RDt** and **RDc** during the first percents of deformation and is replaced after by pyramidal slip as it saturates. This phenomenon, which has already been observed for curves **E**, **F**, **LS** and **TS** in previous chapter, explains the lower macroscopic yield stress of **EDc**, **RDt** and **RDc** compared to **EDt** as well as the sudden increase in stress after 0.05 strain for **EDc** and **RDc**. The relatively low yield stress results from the large contribution of twinning ($\tau_0 = 5$ MPa) to plastic deformation at true strains less than 0.05, and the sudden increase of stresses beyond 0.05 true strain results from the saturation of twinning going along with the activation of pyramidal slip ($\tau_0 = 40$ MPa). The different hardening behaviour of curve **RDc** compared to **EDc** and **RDc**, which do not reveal such a sudden increase of stresses beyond 0.05 true strain even if mechanical twinning is active, may result from the activation of pyramidal slip already at the early stage of plastic deformation. The contribution of twinning is than reduced and so its influence onto the macroscopic flow curve.

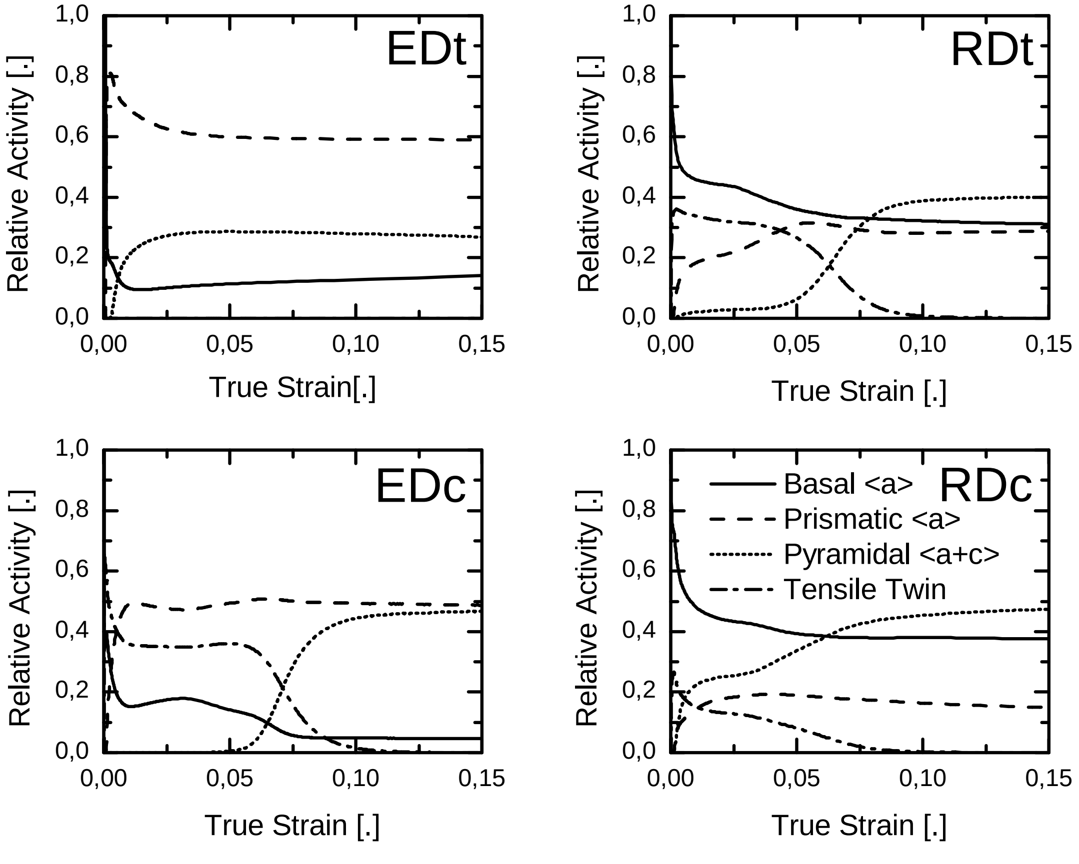

Figure 6.4: *Deformation Modes' relative activity for uniaxial tension and compression tests of Mg alloy extruded rods in extruded and radial direction*

One can also see in Figure 6.4 that in the very beginning of deformation, at strains less than about 0.015, rapid changes in the level of relative activity of the different deformation modes occur. After this range, some kind of an equilibrium is achieved and the relative activities remain almost constant. Plastic deformation occurs thus from almost the beginning of mechanical testing and reduces thus considerably the elastic modulus of the RVE. This explains why Young's moduli different from 45000 MPa are observed for each of the curves **EDc**, **EDc**, **RDt** and **RDc**. The yield stress observed at macroscopic level seems to correspond to the achieved equilibrium of the deformation modes relative activity at strains above 0.05.

Since the flow curves **EDt** and **EDc** reflect well, in a qualitative way, experimental observations [27, 73] of Mg and AZ31 extruded rods, the material parameters, which have been identified in previous chapter have demonstrated to be quite realistic. Further studies on magnesium polycrystalline aggregates, with other virtual or arbitrary textures, may also deliver realistic results. Moreover the use of combined channel die tests of hcp single crystals and polycrystals reveals to be an interesting method for the calibration of the numerous material parameters required in crystal plasticity models in general.

Chapter 7

Crystal Plasticity: Building Yield Surfaces from Biaxial Tests

In this chapter yield surfaces of single crystals and polycrystalline aggregates are generated by simulating biaxial tests. The shape of the yield surfaces are shown to be very anisotropic at both single crystal and polycrystalline levels. Their shape is also shown to be very dependent on the crystallographic orientations and texture, as well as on the material parameters introduced into the crystal plasticity model. These biaxial tests provide thus a deep understanding of the relationship between microstructural features and macroscopic mechanical behavior. Moreover the generated yield surfaces will be used later in this work as references while defining model parameters for a phenomenological yield criterion destined to simulate the mechanical behavior of structures of large length scales.

7.1 Finite Element Models of Biaxial Tests

The finite element models of single crystals and polycrystalline aggregates subjected to biaxial tests with loading path of constant ratio $\sigma_2 \,/\sigma_1 = \arctan(\rho)$, i.e. proportional loading, are illustrated in Figure 7.1.

As it was previously done in this work, one crystal is modeled by a single 8-node brick finite element. The single crystal subjected to biaxial loading is thus modeled by only one finite element and symmetric boundary conditions are applied to ensure the periodicity of the microstructure. In the case of a polycrystalline aggregate subjected to biaxial loading, the RVE is, as it was previously done in this work, modeled by $8 \times 8 \times 8$ finite elements describing the equivalent number of grains. Each grain is attributed a specific crystallographic orientation and the distribution of these orientations in space, representing the texture of the aggregate, is described in Appendix A. The RVE is attributed periodic boundary conditions in order to ensure the microstructure's periodicity.

As shown in Figure 7.1 the loading path is stress controled which allows for ensuring the ratio $\sigma_2 \,/\sigma_1 = \arctan(\rho)$ to remain constant during the test. In order to retrieve information about the yielding behaviour of the tested material in the whole space of stresses, σ_1

and σ_2, 16 loading paths are realised with equally spaced angles $\rho \in [0\,°, 360\,°]$. Usually yield surfaces of a hardening material are displayed as isocontours of the plastic equivalent strain ϵ_p. Therefore a number of unloading steps are realised along each loading path. This unloading steps inform about the state of the residual plastic strains and finally allow for building isocontours of equivalent plastic strain.

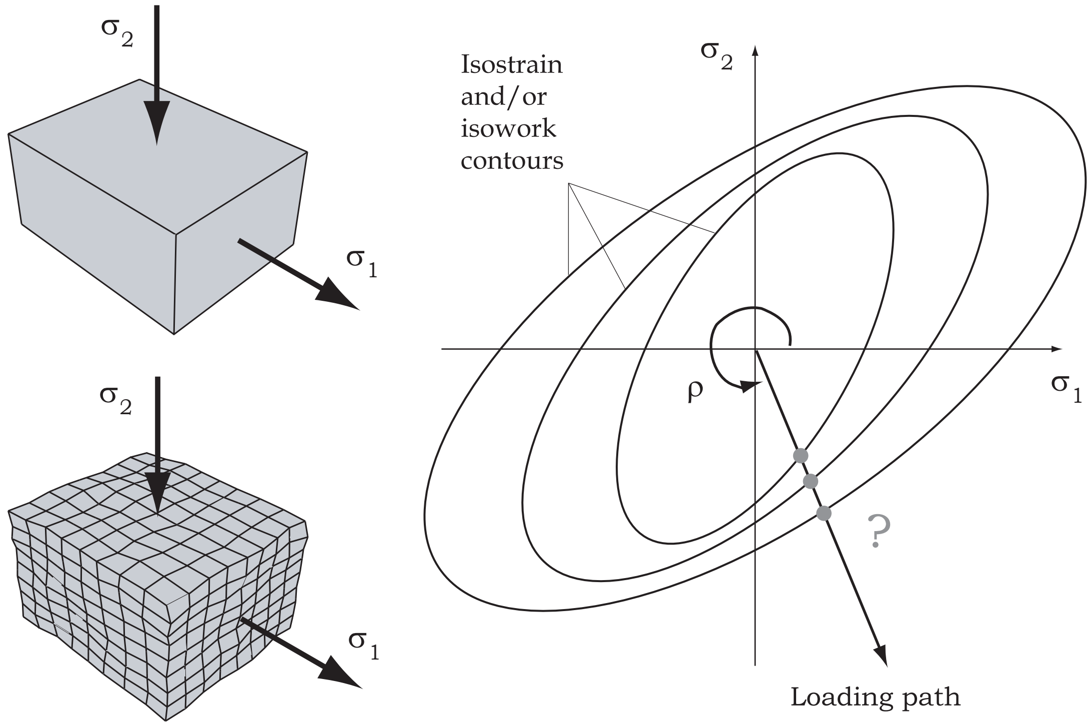

Figure 7.1: *Finite element models of a single crystal (top left) and a polycrystalline aggregate (down left) subjected to a biaxial test with loading path of constant ratio* $\sigma_2\ /\sigma_1 = \arctan(\rho)$ *(right)*

In this chapter, isocontours of equivalent plastic strain but also of equivalent plastic work W_p are shown. The amount of accumulated work W is known using the following equation,

$$W^j = W^{j-1} + \sum_{i=1}^{2} \frac{1}{2}\left(\sigma_i^{(j)} + \sigma_i^{(j-1)}\right)\left(\epsilon_i^{(j)} - \epsilon_i^{(j-1)}\right), \tag{7.1}$$

where the indices ^{j} denotes each time increment in the simulation and $W = W_p$ after each unloading step is completed.
In the following, the isocontours of equivalent plastic strain are plotted for $\epsilon_p = 0.01$ to 0.15 with an increment $\Delta\epsilon_p = 0.01$. In order to allow for the comparison between isostrain and isowork contours, the isocontours of plastic work are plotted for the levels of plastic work corresponding to the values of equivalent plastic strains in direction 1 ($\rho = 0$). Therefore, the level of stresses for ($\rho = 0$) are always identical for both representations of the yield surface evolution. In the following no isostrain contours of $\bar{\gamma}$, the internal variable defining the state of plasticity in the crystal plasticity model, are ploted since those contours have shown very similar yield surfaces shapes than for ϵ_p.

7.2 Yield Surfaces of Single Crystals

Since the mechanical properties of magnesium rolled plates are of main interest in this work, the yield surfaces of single crystals presented in this section have been restricted to a minimum, meaningful for understanding the mechanical features which may occur for such textures. As it was already said in chapter 5, the texture of Mg rolled plates is such that the grains crystallographic orientations, in term of the c-axis, are mainly orientated in plate thickness direction. As a consequence, the simulation results shown in this section consider only crystallographic orientations with c-axis mainly in 3-direction while loading occurs in 1 and 2-direction.

7.2.1 Yield Surfaces Depending on Crystallographic orientation

The strain hardening evolution of the yield surface of a single crystal with c-axis orientated in 3-direction, is illustrated in Figure 7.2. The material parameters used in these calculations are those identified in chapter 5 and are given in Tables 5.2 and 5.3. These yield surfaces reveal to be strongly anisotropic especially regarding their unlike behavior in tension and compression.

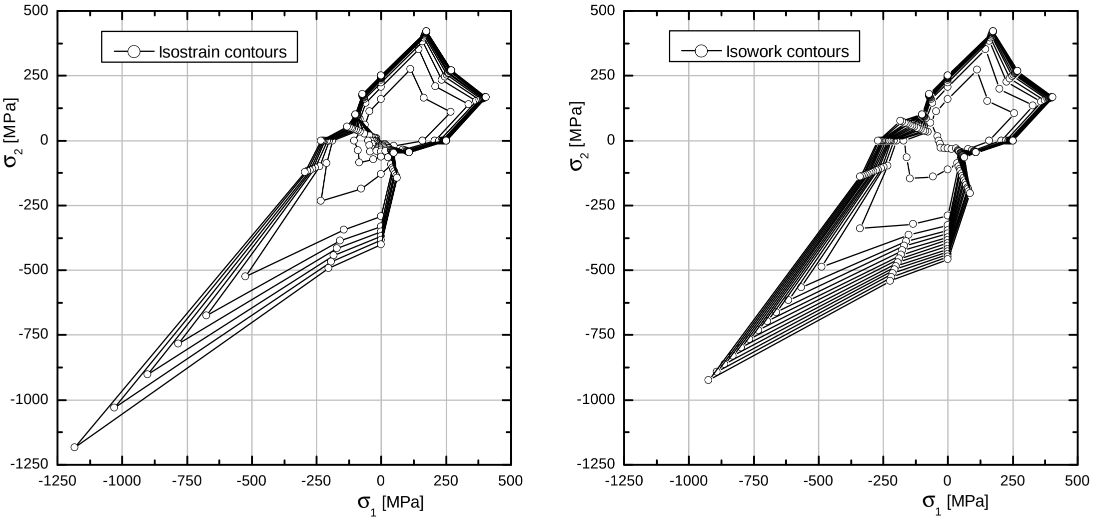

Figure 7.2: *Yield Surface of a single crystal with c-axis orientated in 3-direction, evolving with increasing von Mises equivalent plastic strain (*$\epsilon_p = 0.01, 0.15$ $\Delta\epsilon_p = 0.01$*) (left) and with increasing plastic work (right), obtained by simulations of biaxial tests on RVEs in the (1,2)-plane*

At the very beginning of plastic deformation, the single crystal yield surface shape is almost convex, except for $\rho = 45\,^\circ$, but a sharp non-convexity of the yield surface develops soon at $\rho = 135\,^\circ$ and $315\,^\circ$, already after small values of plastic strain around 0.02. The yield surface shape thus changes much and rapidly until the residual plastic strain reaches values of about 0.1 and tends to remain unchanged. The yield surface shape remains unchanged for all values of ρ except for the biaxial compression case with equal values of σ_1

and σ_2, $\rho = 225\,°$. All these observations hold independently whether the yield surfaces are defined as isocontours of equivalent plastic strain or of plastic work, see Figure 7.2. Since convex yield surfaces are desired in the context of phenomenological modeling, see chapter 4, the sharp non-convexity ($\rho = 135\,°$ and $\rho = 315\,°$) observed in both isocontour representations seem to indicate that the state of plastic deformation may not be defined here by the single scalar values, ϵ_p or W_p. This affirmation is at least true at the level of a single crystal. Nevertheless, the main difference between both isocontour representations of Figure 7.2 exists in the third quadrant. Indeed, in the case of biaxial compression the yield surface reaches much faster higher stresses (in absolute value) in the case of isowork contours than for isotrain contours.

Figure 7.3 illustrates the contribution of the 4 deformation modes considered to the overall plastic deformation of the sample, and thus help for analysing the highly anisotropic yield surface shapes in more detail. One can first notice that basal slip is never active in any of the 16 loading paths, even if its CRSS is far the smaller of all deformation modes considered, see Table 5.2. This is due to the crystallographic orientation, indeed the loads σ_1 and σ_2 are orientated $90\,°$ to the basal plane, which implies a Schmid factor $\mu = 0$.

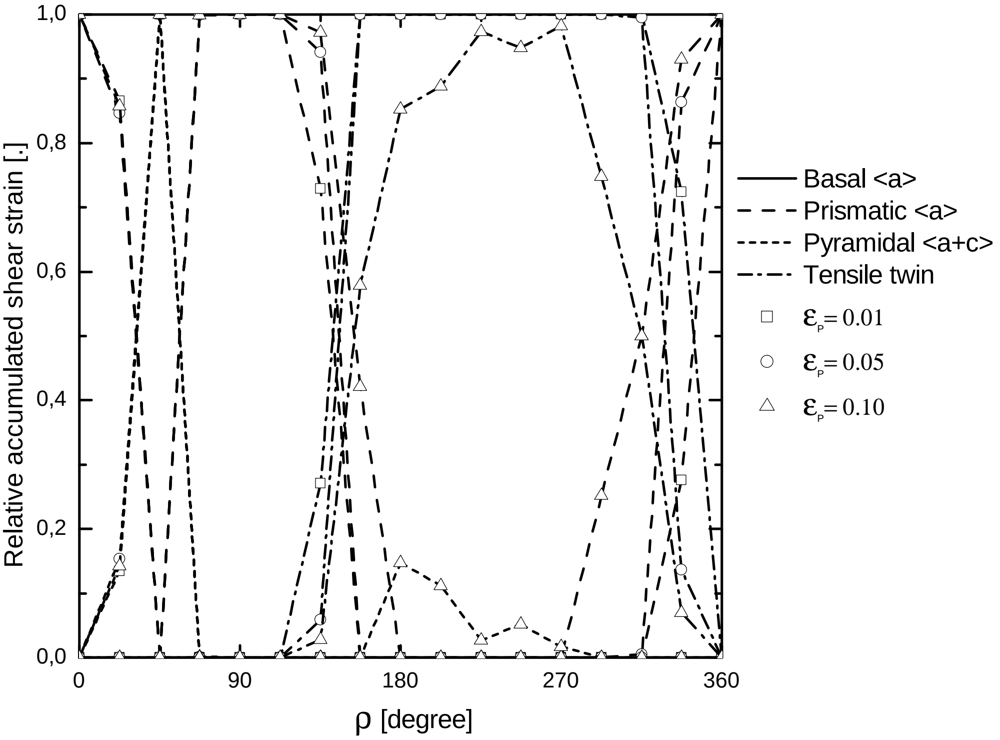

Figure 7.3: *Relative accumulated shear strain for the 4 considered deformation modes at 0.01, 0.05 and 0.10 equivalent plastic strain for biaxial tests in the (1,2)-plane on a Mg single crystal with c-axis orientated in 3-direction*

Figure 7.3 also reveals that plastic deformation is controled mainly by prismatic slip and mechanical twinning over all loading paths. Twinning dominates plastic deformation for $\rho \in]135\,°, 315\,°[$ and prismatic for $\rho \in]315\,°, 0\,°] \cup [0\,°, 135\,°[$. The transition from one dominant mode to the other one, at $\rho = 135\,°$ and $\rho = 315\,°$, results in the sharp non-convexity of the yield locus mentioned previously. This is a very interesting result since, for example, the corners of the Tresca yield criterion may be interpreted as the transition from one slip system to another which is at least an analogon. In Figure 7.2 the non-convexity is an additional effect of the different CRSS of the various slip systems and especially of their different hardening behaviors.

The slight non-convexity of the yield surfaces in Figure 7.2, for $\rho = 45\,^\circ$ already at small strains, is due to the activation of only pyramidal slip, instead of prismatic for lower and higher values of ρ, and this at all strains ϵ_p from 0.01 to 0.1. Pyramidal slip is also shown in Figure 7.3 to be active at relatively high strains ($\epsilon_p = 0.1$) in the third quadrant after twinning has saturated, which is a phenomenon already observed in the two previous chapters. In addition, due to the crystallographic orientation the CRSS of pyramidal slip is reached earlier around $\rho = 180\,^\circ$ than around $\rho = 270\,^\circ$ and the corresponding relative accumulated shear strain is therefore higher for $\rho = 180\,^\circ$ than for $\rho = 270\,^\circ$. This explaines the enormous difference in stresses at high strains $\epsilon_p = 0.15$ for these angles which is absent at $\epsilon = 0.01$, see Figure 7.2.

Hot rolled plates made out of magnesium show the predominant crystallographic orientation of the c-axis tilted typically from 10 to 20 ° from the plate thickness direction. In order to quantify the effect of such a variation of the crystallographic orientation from 3-direction onto the predicted yield surface, the previous single crystal is rotated 10 ° around 1-direction and new biaxial tests are performed. The evolution of the yield surface for this new single crystal model, with c-axis in the (2,3)-plane 10 ° away from 3-direction, is displayed in Figure 7.4. The contribution of the deformation mechanisms to plastic deformation of this new single crystal model is illustrated in Figure 7.5.

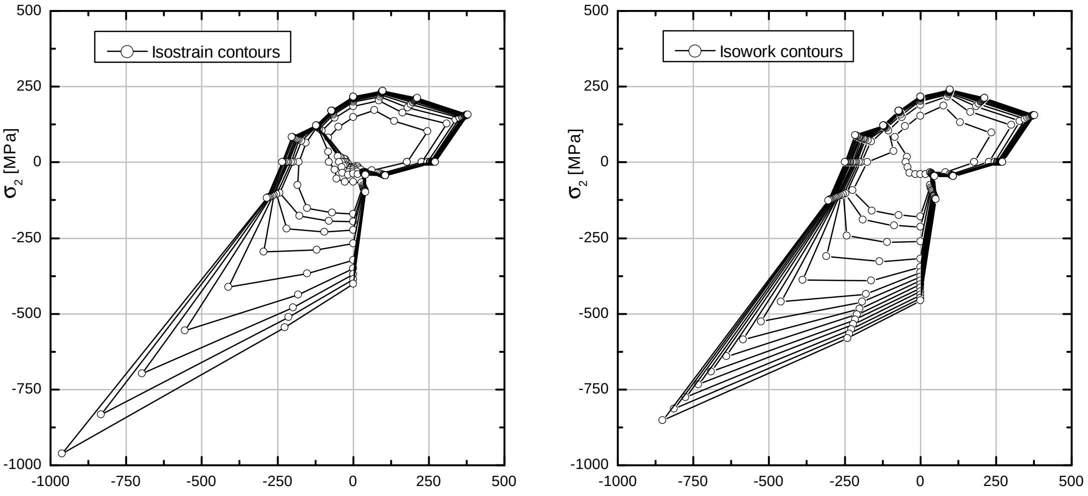

Figure 7.4: *Yield Surface of a single crystal with c-axis pointing in the (2,3)-plane* $10\,^\circ$ *away from direction 3 evolving with increasing von Mises equivalent plastic strain (*$\epsilon_p = 0.01, 0.15$*) (left) and increasing plastic work (right), obtained by simulations of biaxial tests on RVEs in the (1,2)-plane*

The yield surfaces shapes of Figure 7.4 show very similar features than those of Figure 7.2, for both the isocontours of equivalent plastic strain and plastic work. Nevertheless, the stress levels in Figure 7.4 compared to Figure 7.2, tend to reduce (in absolute value) such that the slight non-convexity for $\rho = 45\,^\circ$ and the sharp non-convexity for $\rho = 135\,^\circ$ almost disappeared. After Figure 7.5 the new crystallographic orientation is much more favorable for basal slip in the whole range $\rho \in [0\,°, 360\,°]$ which explains the general diminuation of the stress levels in the yield surfaces of Figure 7.4 compared to Figure 7.2. The CRSS of basal slip systems is indeed low, see Table 5.2.

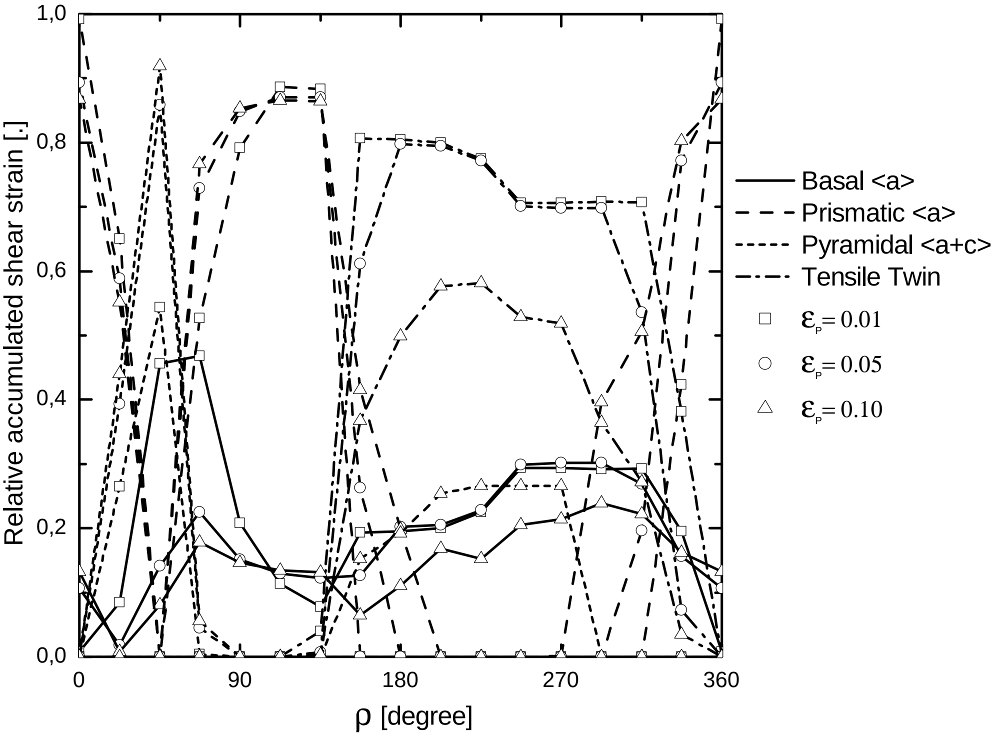

Figure 7.5: *Relative accumulated shear strain for the 4 considered deformation modes at 0.01, 0.05 and 0.10 equivalent plastic strain for biaxial tests in the (1,2)-plane on a Mg single crystal with c-axis pointing in the (2,3)-plane 10° away from direction 3*

A much more detailled study concerning the influence of crystallographic orientation on the mechanical properties of hcp single crystals has been realised during the time of this work and is available in [72]. The investigation in [72] shows for example that the more c-axis is tilted out of the 3-direction, rotating around 1-direction (as it has been done here), the more the values of the stress component in 2-direction become small (in absolute value) as noted just before. This is due to an increasing contribution of basal slip to the plastic deformation. Rotating instead the c-axis around 2-direction away from 3-direction affects the values of the stress component in 1-direction, they tend to get small (in absolute value) the more the c-axis is tilted away from 3-direction.
The two examples of biaxial tests presented above emphasize the strong dependence of the yield surface shape on the crystallographic orientation with respect to the c-axis.

7.2.2 Yield Surfaces Depending on Material Parameters

In this section, biaxial tests of a hcp single crystal with c-axis orientated again in 3-direction are simulated under the same conditions as described at the beginning of the present chapter. The direct hardening parameters displayed in Table 5.2 are introduced into the crystal plasticity model but the interaction parameters in Table 5.3 are not, they are put equal to zero instead. The evolution of the yield surfaces resulting from these biaxial tests, see Figure 7.6, are to be compared to those of Figure 7.2, which emphasizes the influence of the material parameters onto the yield surface shape of hcp single crystals. Indeed, both figures show yield surfaces of very different shapes.

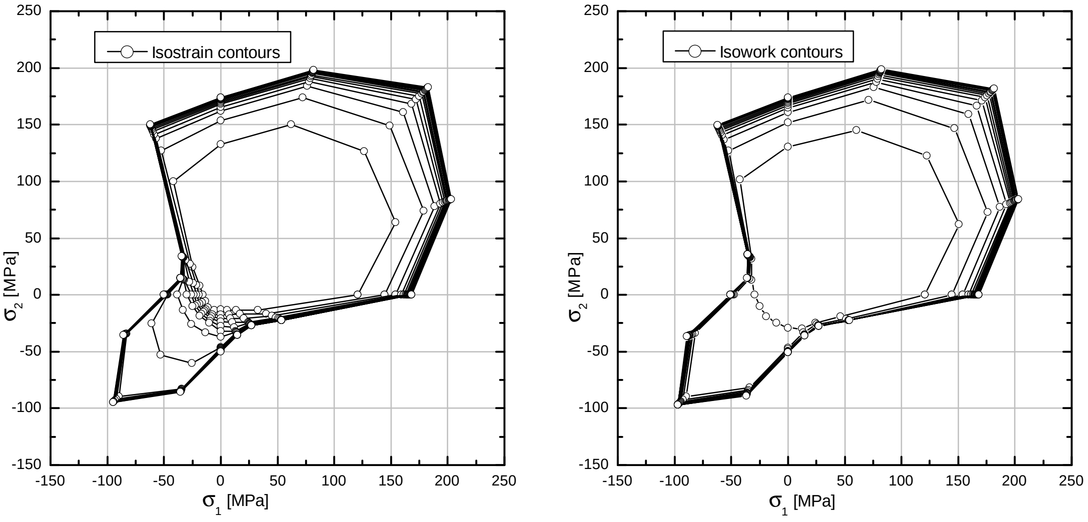

Figure 7.6: *Yield Surface of a single crystal with c-axis orientated in 3-direction with increasing von Mises equivalent plastic strain (*$\epsilon_p = 0.01, 0.15$*) (left) and with increasing plastic work (right), obtained by simulations of biaxial tests on RVEs in the (1,2)-plane*

Beside the obvious difference in the yield surfaces' shapes, the stresses reached at 0.15 strain in Figure 7.6 are far lower than reached in Figure 7.2. Some similarities between both figures nevertheless exist. From the early stage of plastic deformation to approximately 0.10 plastic strain, the yield surface shape changes much and rapidly. After 0.10 plastic strain it remains unchanged. The non-convexity of the yield surface for $\rho = 135\,^\circ$ and $315\,^\circ$ is less sharp in Figure 7.6 but still exists and it is still due to the transition between prismatic and twinning deformation modes which dominates plastic deformation, see Figure 7.7. This figure displays the contribution of the 4 deformation modes considered to the overall plastic deformation of the sample, in terms of the relative accumulated shear strain.

According to Figure 7.7, and similarly to observations made in Figure 7.3, basal slip is not activated in these calculations. This is again due to the Schmid factor $\mu = 0$ of the respective crystallographic orientation and loading directions. Differently to Figure 7.3, in Figure 7.7 pyramidal slip is more active in the first quadrant, for $\rho \in [0\,^\circ, 90\,^\circ]$, but not anymore in the third one, except for $\rho = 225\,^\circ$. Here, prismatic slip overtakes plastic deformation after mechanical twinning has saturated, instead of pyramidal slip which was observed many times in this and previous chapters.

Regarding the enormous dissimilarity of Figures 7.6 and Figure 7.2, as well as of Figures 7.7 and Figure 7.3, it can be concluded that the identification step of the material parameters is of crucial importance.

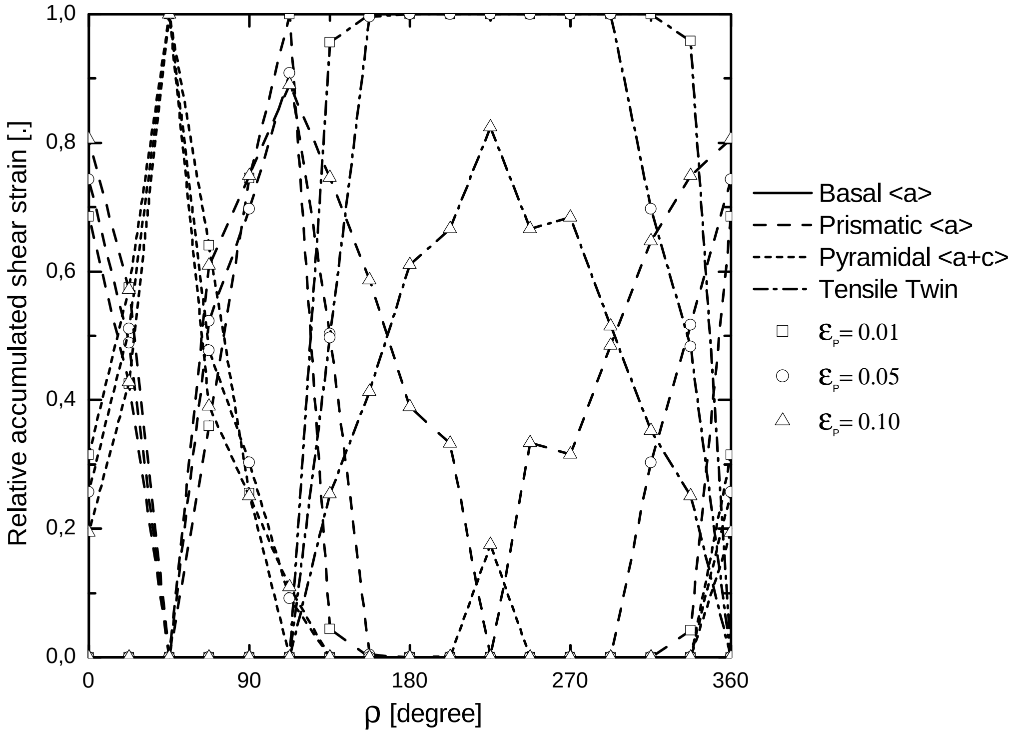

Figure 7.7: *Relative accumulated shear strain for the 4 considered deformation modes at 0.01, 0.05 and 0.10 equivalent plastic strain for biaxial tests in the (1,2)-plane on a Mg single crystal with c-axis orientated in 3-direction*

7.3 Yield Surface of Polycrystalline Aggregates

7.3.1 Non-Textured Material

A non-textured polycrystalline material is characterized by the absence of preferred crystallographic orientations. Billet materials for example, generally do not show any preferred crystallographic orientation because they are not subjected to any external deformation during their fabrication process. The discrete crystallographic orientations, representing a non-textured material and introduced into the RVE which subjected to biaxial tests, are generated via the procedure described in Appendix A. The corresponding stereographic pole figure of the virtual material thus created is shown in Figure 7.8. The yield surface describing the mechanical behavior of this material and its evolution with increasing plastic strain and plastic work is displayed in Figure 7.9.

Concerning both plots of Figure 7.9 one can first notice that they show very similar features. It is even difficult to differentiate them from each other. The elliptic yield surfaces shapes observed at the small strain $\epsilon_p = 0.01$ and at higher strains $\epsilon \geqslant 0.10$ are typical for an isotropic von Mises material. This indicates that the non-textured material behaves almost isotropically at these strains. It means thus that the initial yield surface is isotrope and that the hardening is isotropic too since the yield surface is centered on the origin and its extension is relatively homogeneous and independant on the loading paths.

Similarly to previous calculations in this work, saturation in the hardening behavior is almost reached at 0.15 strain.

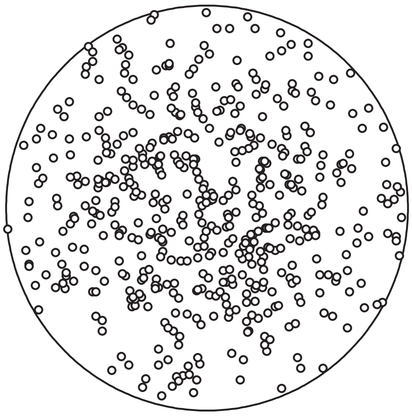

Figure 7.8: *(0001) pole figure of a non-textured material in stereographic projection*

The isotropic mechanical behavior described just above nevertheless does not strictly hold for the strain range 0.02 to 0.10. In this range, and on the axes of principal stresses σ_1 and σ_2, a noticeable yielding asymmetry in tension and compression is apparant. This effect is particularly strong when comparing the loading paths for $\rho = 45^\circ$ and $\rho = 225^\circ$ in Figure 7.9. A non neglectable asymmetry in the material's mechanical behavior, observable in the range 0.02 to almost 0.10 plastic strain, seems thus to be induced.

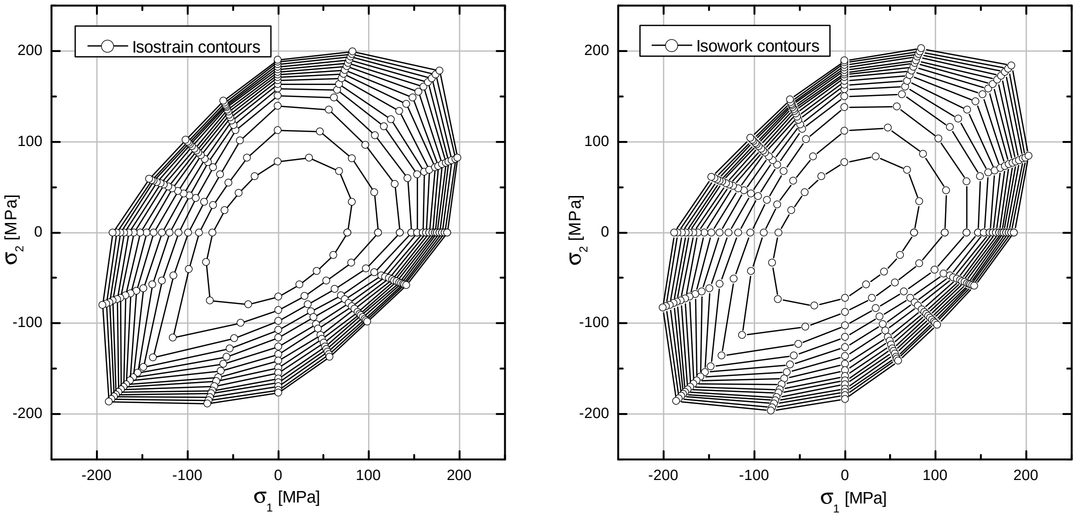

Figure 7.9: *Yield Surface of a non-textured Mg polycrystalline aggregate evolving with increasing von Mises equivalent plastic strain ($\epsilon_p = 0.01, 0.15$) (left) and with increasing plastic work (right), obtained by simulations of biaxial tests on RVEs in the (1,2)-plane*

The deformation modes' relative activity in dependence on the loading path is displayed in Figure 7.10. Relative activity describes the contribution of the 4 deformation modes considered to the overall plastic deformation of the sample, and this reveals surprisingly that mechanical twinning in not responsible for the induced asymmetry observed. This was actually expected by the author regarding all previous calculations in this work which were showing twinning to be the main deformation mode contributing to plastic deformation in the case of biaxial compression, $\rho \in [180\,°, 270\,°]$. After Figure 7.10 twinning contributes almost equally and for less than 10% to the increase of plastic strain, in the whole range $\rho = [0\,°, 360\,°]$. As plastic strain increases the contribution of mechanical twinning becomes even less. The relative activity of pyramidal slip show that this deformation mode may also not explain the induced anisotropy since it is also almost equally distributed in the whole range $\rho = [0\,°, 360\,°]$ for the three values of plastic strain ϵ_p =0.01, 0.05 and 0.10.

The activity of basal and prismatic slip in Figure 7.10 show more interesting features instead. Both oscillate and this happens in opposite phase which emphasizes the competition between both deformation modes for participating to plastic deformation. Indeed, both family of slip systems allow for plastic deformation in a-direction and compete therefore. The CRSS of basal slip is much smaller than the one of prismatic slip, see Table 5.2, which explains why the relative activity of basal slip is higher than prismatic slip on the whole range $\rho = [0\,°, 360\,°]$. The higher activity of basal slip and comparatively lower activity of prismatic slip for $\rho = 180°$ and 270°, compared to $\rho = 0°$ and 90°, may explain well the unlike yielding behavior between tension and compression which has been noticed previously at strains from 0.02 to 0.10. The same observations concerning the unlike stress levels for $\rho = 45\,°$ and $225\,°$ hold, see Figure 7.10.

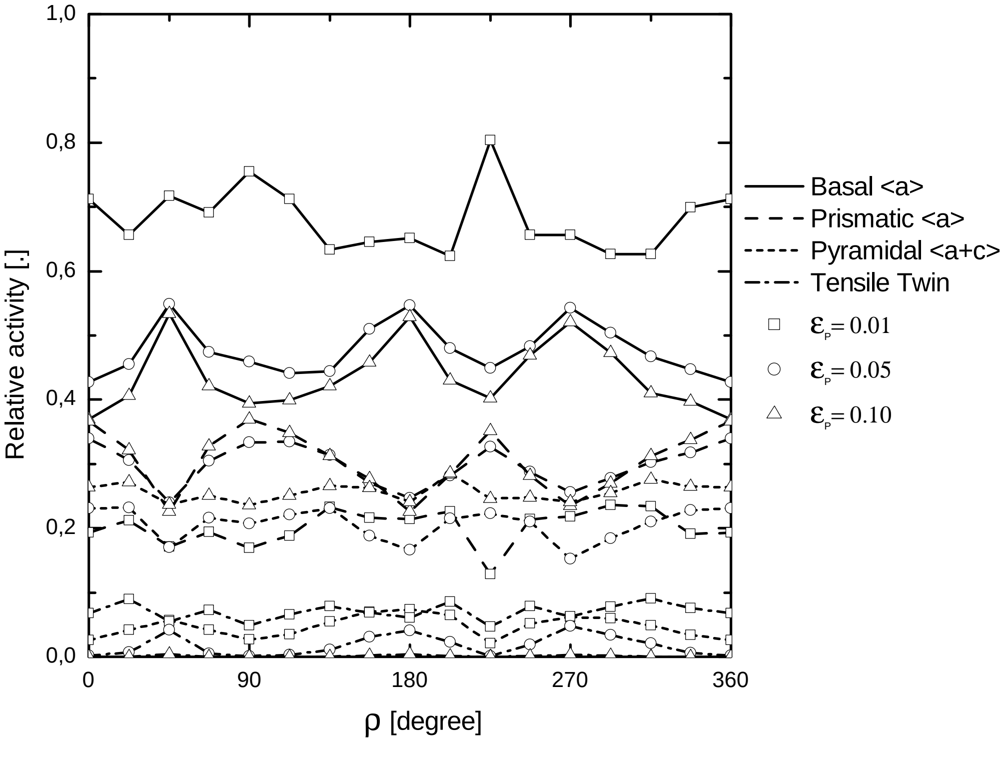

Figure 7.10: *Relative activity of the 4 considered deformation modes at 0.01, 0.05 and 0.10 equivalent plastic strain for biaxial tests in the (1,2)-plane on a non-textured Mg polycrystalline aggregate*

In the case of hcp metals, the strong asymmetry observed at single crystal scale is not compensated completely by the fact that the material is non-textured. It seems that a certain asymmetry, induced here by the competition between basal and prismatic slip, can still be noticed at macroscopic level.

7.3.2 Textured Rolled Plates

Kelley and Hosford [44] have determined yield loci in the (L,T)-plane of rolled plates experimentally for varying levels of the largest principal strain ϵ_I, as 1, 5, 10%, using the experimental results presented in Figure 5.5 as well as uniaxial tension and compression tests in L-,T- and S-direction. A comparison of test and simulation results of the uniaxial tests is presented in Table 7.1.

As in the biaxial loading case of this chapter, the simulations of uniaxial tension and compression tests of polycrystalline aggregates in L, T and S-direction were performed on RVEs of 8 × 8 × 8 solid elements, one finite element represents one physical grain, having the same discrete crystallographic orientations as presented in the pole figure of Figure 5.2. Periodic boundary conditions were also applied on the surfaces of the RVE to ensure the microstructure periodicity.

	1% principal strain		5% principal strain		10% principal strain	
	Exp.	Sim.	Exp.	Sim.	Exp.	Sim.
L-tens. [MPa]	68.3	75.0	100.0	153.9	–	169.9
S-comp. [MPa]	66.2	65.9	127.6	97.5	147.5	108.7
T-tens. [MPa]	129.6	105.2	173.7	176.0	194.4	188.1
L-comp. [MPa]	26.9	30.2	54.5	89.1	146.2	164.2
T-comp. [MPa]	28.3	53.4	71.7	109.4	172.4	204.1

Table 7.1: *Yield stresses of textured polycrystalline specimens in L-, T-, and S-orientation at three strain levels under uniaxial tension and compression; comparison of test results from Kelly and Hosford [44] with results of RVE simulations*

The simulated stresses in Table 7.1 overestimate the experimental ones for **L-tens**, **L-comp**, and **T-comp** while the experimental stresses are underestimated for **S-comp** and at 1% principal strain for **T-tens**. Nevertheless, the levels of stresses, which is very different depending on the test considered, is qualitatively well reproduced. The two most notable aspects of the yield behavior for magnesium plates are thus satisfactory reproduced by the simulations, namely anisotropy and tension-compression asymmetry. In view of a number of approximations and imponderabilities in the simulations, particularly with respect to the parameter identification and the mapping of the texture, as well as possible uncertainties in the evaluation of the test data, the coincidence of experimental and numerically simulated tests is satisfying and encouraging for the generation of qualitatively realistic yield surfaces of the rolled plate material.

Figure 7.11 shows subsequent yield surfaces for mesoscopic stresses under increasing equivalent plastic strain from ϵ_p =0.01 to 0.10 with an increment $\Delta\epsilon_p$ = 0.01. At low values of plastic strain the RVE exhibits a strong anisotropy and a high asymmetry of yielding between tension and compression while, with increasing plastic strain the anisotropy and yielding asymmetry reduce considerably.

As in previous representations of yield surfaces in this chapter, the isocontours of plastic work are also displayed in Figure 7.11. It can be noticed again on Figure 7.11 that the yield surface is not convex at low values of dissipated work. As in the single crystalline case the main differences in the isoline shapes is located at the early stage of deformation where twinning is activated. This observation emphasizes again that neither the equivalent plastic strain nor the dissipated work are adequate quantities to qualify the degree of plasticity in such a material, and this neither at single crystal level (see Figure 7.2) nor at polycrystalline level.

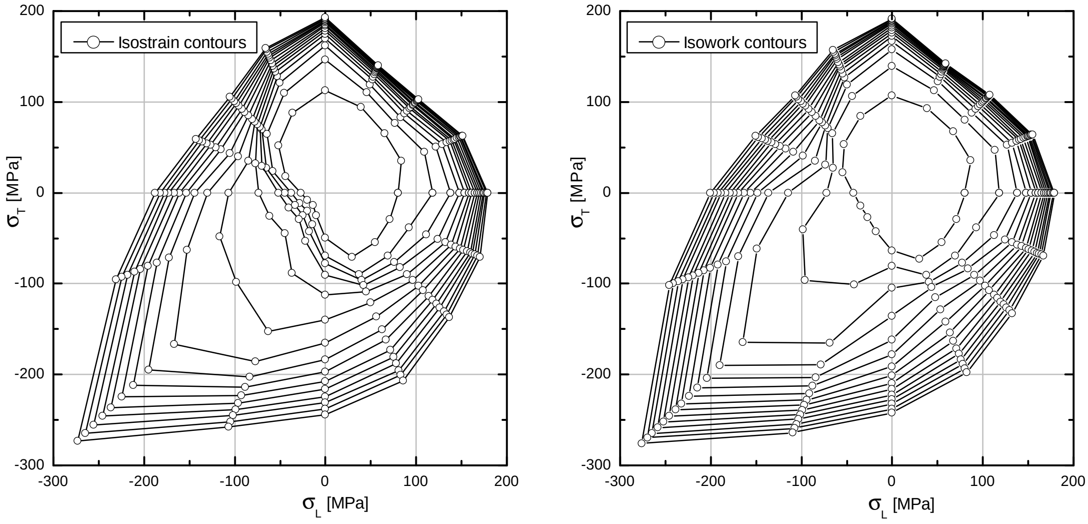

Figure 7.11: *Yield surface of textured Mg rolled plate material evolving with increasing von Mises equivalent plastic strain* ($\epsilon_p = 0.01$ *to 0.15) (left) and with increasing plastic work (right), obtained by simulations of biaxial tests on RVEs in the (L,T)-plane*

The evolution of the relative accumulated shear strain of the 4 deformation modes considered in the calculations is presented in Figure 7.12 in dependence on the angle ρ of the loading path. The contributions of basal and prismatic slip oscillate with a period of approximately $180\,^\circ$ and a phase shift of about $90\,^\circ$ to each other. Both deformation modes act equally in tension and compression. The phase shift of $90\,^\circ$ points out that both, basal and prismatic slip, which act in $\langle a \rangle$ direction, compete with each other. This phenomenon has already been observed in previous section and it has been identified to be at the origin of induced anisotropy in the material.

Even though the texture of a rolled plate is not actually the most favorable for basal slip, it is, in average over the whole range $\rho \in [0\,^\circ, 360\,^\circ]$, the most active deformation mode due to its extremely low CRSS. Interestingly, the relative contribution of basal slip to the accumulated shear strain tends to decrease with increasing strain while that of the prismatic slip tends to increase. This is probably also related to the difference in CRSS for both deformation mechanisms implying that basal slip is more active at the beginning of the deformation, where stresses are lower, than at the end, and prismatic slip becomes more active at higher strains.

As expected, tensile twin is activated for $\rho \in [120\,^\circ, 330\,^\circ]$ only, where compression is present and, due to the texture, elongation in c-direction is favored. The highest twinning activity is concentrated in the range $\rho \in [180\,°, 270\,°]$, where compression states exist in both longitudinal and transverse direction of the plate. Pyramidal slip is significantly active in the range $\rho \in [0\,°, 90\,°]$, where shortening along the c-axis is favored. Following the same principle as in orientations **E** and **F** in Figure 5.3, as well as **LS** and **TS** in Figure 5.5, pyramidal slip $\langle a + c \rangle$ for $\rho \in [120\,°, 330\,°]$ is absent at low strains and activated at higher strains once twinning saturates.

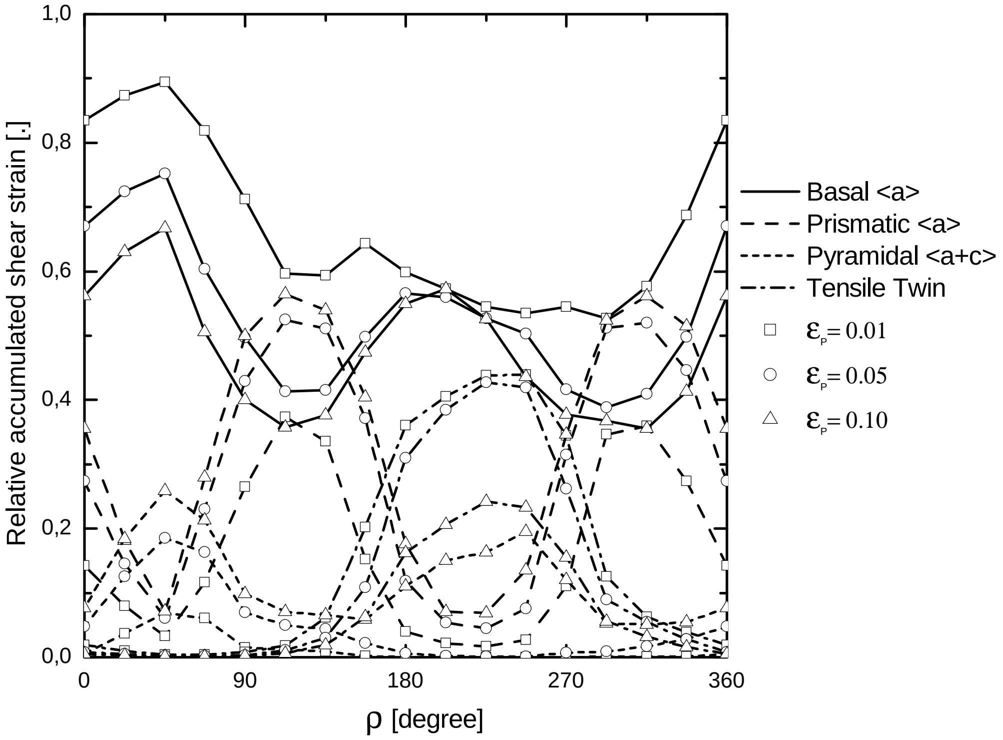

Figure 7.12: *Relative accumulated shear strain for the 4 considered deformation modes at 0.01, 0.05 and 0.10 equivalent plastic strain for biaxial tests in an Mg textured rolled plate plane*

7.4 Influence of Texture on the Yield Surface of Rolled Plates

The previous section has shown that the mechanical properties of Mg rolled plates can be well captured by the crystal plasticity model together with the material parameters of Tables 5.2 and 5.3. In the present section yield surfaces for rolled plates having a texture slightly different than in previous section are generated. The purpose of this investigation is to get some information about the sensitivity of the generated yield surfaces shapes of the RVEs regarding variations in the rolled plate texture.

In section 7.2.1 of this chapter it was shown that even small changes in the crystallograhic orientation of single crystals, with respect to the plane of principal stresses, influenced considerably the resulting yield surfaces' shapes, and thus the mechanical properties, of the sample tested. In case observations similar to those made at single crystal level hold at polycrystalline level these would be of high interest for improving the mechanical properties of Mg rolled sheets, see [42]. Indeed, parameters like the thickness reduction for each path or the final reduction in thickness may be tuned during the sheet fabrication process in order to obtain a desired specific texture, which has itself being predicted to have specific desired mechanical properties.

The RVEs which are subjected to biaxial loading tests in this section are attributed the discrete crystallographic orientations of the pole figures shown in Figure 7.13. These textures are slightly different from the rolled plate texture of Figure 5.2, used in previous section as well as in chapter 5. In this section also the discrete crystallographic orientations are generated after the description in Appendix A, for a rolled plate texture. But compared to the texture in the previous section, the centers of the two texture components (assumed in Appendix A) in Figure 7.13, are chosen to be at a greater distance d from the pole figure origin. The standard deviation σ_{sd}, also defined in Appendix A, is chosen smaller in this section than in the previous one, see Figure 5.2.

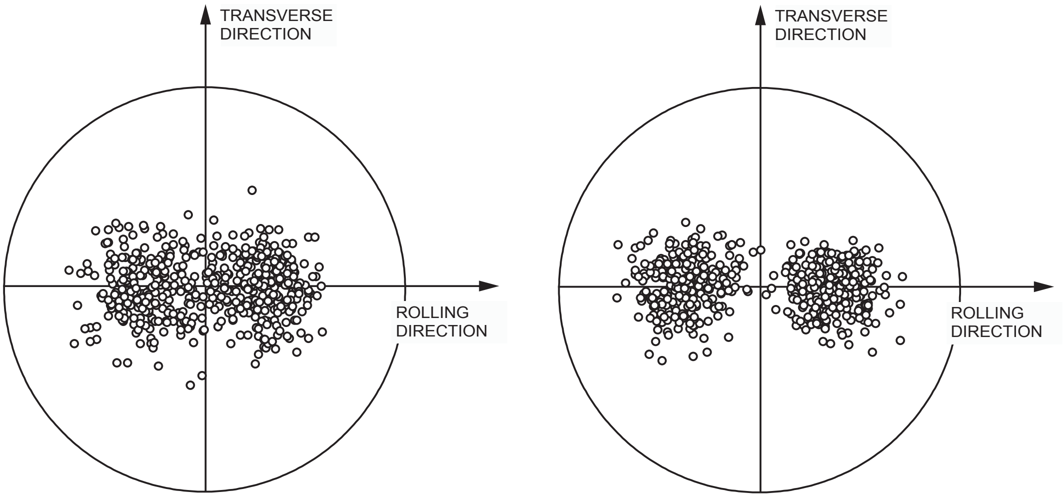

Figure 7.13: *(0001) pole figures of two rolled plate textures differing sligthly from that of Figure 5.2*

For both pole figures of Figure 7.13, the Figures 7.14 and 7.15 compare the yield surfaces resulting from the biaxial tests and the relative accumulated shear strain of the 4 deformation modes considered depending on the loading path, respectively. The material parameters introduced into the crystal plasticity model are the one listed in Tables 5.2 and 5.3.

After Figure 7.14, at small strains, the variations in the proposed virtual textures tend to reduce the unlike yielding in tension and compression in directions L and T of the plate. The anisotropy regarding each of these directions increases instead. Indeed, the ratio of yield stresses in tension for $\rho = 0\,°$ and $90\,°$, and in compression for $\rho = 180\,°$ and $270\,°$, tends to move away from 1. At relatively high strains $\epsilon_p = 0.15$, the stress levels (in absolute value) tend to increase for $\rho = 90\,°$ and $270\,°$ and to decrease for $\rho = 0\,°$ and $180\,°$. These differences in the stress levels are nevertheless small in the tension cases

($\rho = 0\,^\circ$ and $90\,^\circ$) while in the compression cases it is about 50 MPa in both L and T directions ($\rho = 180\,^\circ$ and $270\,^\circ$) of the plate, which is significant.

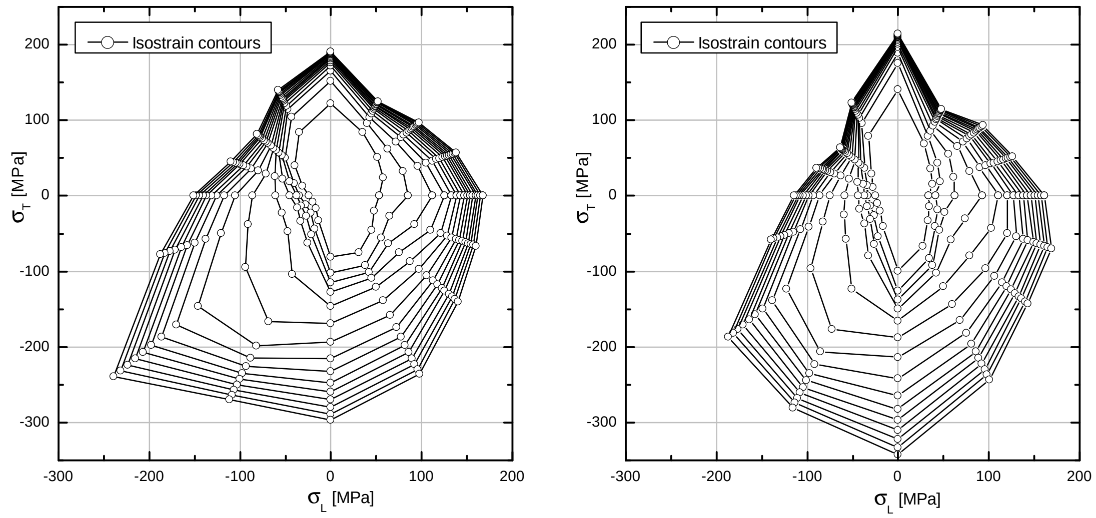

Figure 7.14: *Yield surface of the two Mg polycrystalline aggregates, with textures of Figure 7.13, evolving with increasing von Mises equivalent plastic strain (*$\epsilon_p = 0.01, 0.15$*) and are obtained by simulations of biaxial tests on RVEs in the (L,T)-plane*

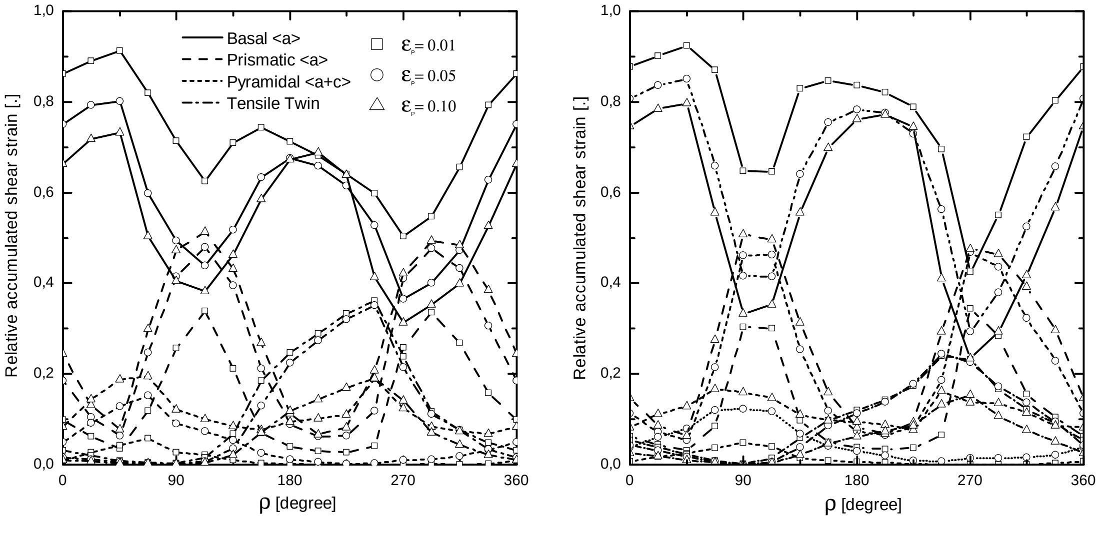

Figure 7.15: *Relative accumulated shear strain for the 4 considered deformation modes at 0.01, 0.05 and 0.10 equivalent plastic strain for biaxial tests of two Mg textured rolled plates with textures of Figure 7.13*

The curves of relative accumulated shear strain in Figure 7.15, compared to those of Figure 7.12, indicate that the deformation modes activated in the different loading paths of the biaxial tests are not variing much except in the range $\rho \in [180\,^\circ, 270\,^\circ]$ where the activity of twinning tends to decrease and is compensated by an increase of basal slip. This observation explains well the reduction of asymmetry in yielding between tension and compression tests, in both L and T directions of the plate, which was noticed previously. The variations in the rolled plate texture tend to be profitable for the activation of basal slip on almost the whole range $\rho \in [0\,°, 360\,°]$, whether that of prismatic slip tends to decrease slightly. This phenomenon has already been observed in section 7.2.1 of this chapter. The activity of pyramidal slip remains relatively small for all loading paths.

The investigations in this section seem to indicate that variations in the rolled plate texture lead to non neglectable changes in the plate's mechanical properties. The variation of the plate mechanical properties under tension loadings seem nevertheless to be restricted to small strains. The ductility and ultimate stress of Mg plates, while subjected to tensile loads, may thus not be improved substantially in variing the plate's texture.

Chapter 8

Phenomenological Modeling: a Yield Criterion for Mg Plates

Simulations of the deformation behavior of structures with length scales far above that of crystallographic grains cannot be performed effectively with crystal plasticity models but require phenomenological constitutive equations for yielding and hardening under multiaxial stress states. The transportation industry is especially interested in thin products, sheet metals, which are fabricated via a rolling process. Due to the metals crystallographic structures and the characteristics of this process, which generates large plastic deformations, the mechanical properties of sheet metals are usually affected by an important anisotropy. This has already been observed in chapter 7 of this work while considering the case of Mg rolled plates. The anisotropy of the mechanical properties is of two natures: the anisotropy of the yield stress and that of the plastic strain. While the anisotropy of the yield stress for magnesium plates and its dependence on the material's texture has already been well observed and discussed in chapter 7, both the anisotropy of yield stress and plastic strain are discussed in the present chapter.

8.1 Definition of the Yield Criterion

As illustrated in Figure 7.11 the yield locus of magnesium plates is far from being isotropic but shows strong anisotropy and yielding asymmetry between tension and compression. As demonstrated in chapter 4, yield criteria like those of Tresca and von Mises can thus not be adapted to phenomenological modeling of the yielding behavior of magnesium plates. Accounting for the asymmetric yielding in tension and compression shown in Figure 7.11 which shifts the center of the yield surface out of the origin of the deviatoric plane, requires including the third invariant of the stress tensor, see Drucker [24]. The yield criterion proposed by Cazacu and Barlat [19] which includes the third invariant,

$$\Phi = \left(J_2^o\right)^{\frac{3}{2}} - J_3^o - {\tau_Y}^3 = 0, \tag{8.1}$$

has been shown to be suited to model yielding behavior of hcp metals [20] and especially magnesium and its alloys [19]. Please note that the scalar model parameter c introduced in [19] in front of J_3^o is omitted here since it can be distributed inside J_3^o. In the above equation τ_Y is the yield stress in pure shear and the quantities J_2^o and J_3^o are the generalization to orthotropy of the second and third invariants of the deviatoric stress tensor, respectively. They are expressed as functions of the stress components as,

$$J_2^o = \frac{a_1}{6}\big(\sigma_x - \sigma_y\big)^2 + \frac{a_2}{6}\big(\sigma_y - \sigma_z\big)^2 + \frac{a_3}{6}\big(\sigma_x - \sigma_z\big)^2 + a_4\sigma_{xy}^2 + a_5\sigma_{xz}^2 + a_6\sigma_{yz}^2, \tag{8.2}$$

and

$$\begin{aligned} J_3^o = {} & \frac{1}{27}\big(b_1 + b_2\big)\sigma_x^3 + \frac{1}{27}\big(b_3 + b_4\big)\sigma_y^3 + \frac{1}{27}\Big[2\big(b_1 + b_4\big) - b_2 - b_3\Big]\sigma_z^3 \\ & -\frac{1}{9}\big(b_1\sigma_y + b_2\sigma_z\big)\sigma_x^2 - \frac{1}{9}\big(b_3\sigma_z + b_4\sigma_x\big)\sigma_y^2 - \frac{1}{9}\Big[\big(b_1 - b_2 + b_4\big)\sigma_x + \big(b_1 - b_3 + b_4\big)\sigma_y\Big]\sigma_z^2 \\ & +\frac{2}{9}\big(b_1 + b_4\big)\sigma_x\sigma_y\sigma_z + 2b_{11}\sigma_{xy}\sigma_{xz}\sigma_{yz} - \frac{\sigma_{xz}^2}{3}\Big[2b_9\sigma_y - b_8\sigma_z - \big(2b_9 - b_8\big)\sigma_x\Big] \\ & -\frac{\sigma_{xy}^2}{3}\Big[2b_{10}\sigma_z - b_5\sigma_y - \big(2b_{10} - b_5\big)\sigma_x\Big] - \frac{\sigma_{yz}^2}{3}\Big[\big(b_6 + b_7\big) - b_6\sigma_y - b_7\sigma_x\Big]. \end{aligned} \tag{8.3}$$

The indices x, y, z, correspond to the coordinate system associated with orthotropy. For the magnesium rolled sheets considered in this work, the coordinate system (O, x, y, z) corresponds to (O, L, T, S) where L, T, S, represent the plates longitudinal, tranverse, and short direction. The latter indices will be used in the following mathematical notations. The yield criterion of equation 8.1 reduces to von Mises [83] yield criterion as the model parameters $a_i = 1$ and $b_i = 0$.

In the three dimensional case, 17 model parameters are necessary for a full description of the yield criterion of equation 8.1, which is a great number that one can hardly pretend to fit accurately. Nevertheless, in the plane stress case the number of model parameters reduces to 10 and the quantities J_2^o and J_3^o can be rewritten as,

$$J_2^o = \frac{a_1}{6}\big(\sigma_L - \sigma_T\big)^2 + \frac{a_2}{6}\sigma_T^2 + \frac{a_3}{6}\sigma_L^2 + a_4\sigma_{LT}^2, \tag{8.4}$$

and

$$\begin{aligned} J_3^o = {} & \frac{1}{27}\big(b_1 + b_2\big)\sigma_L^3 + \frac{1}{27}\big(b_3 + b_4\big)\sigma_T^3 - \frac{1}{9}b_1\sigma_T\sigma_L^2 - \frac{1}{9}b_4\sigma_L\sigma_T^2 \\ & -\frac{\sigma_{LT}^2}{3}\Big[-b_5\sigma_T - \big(2b_{10} - b_5\big)\sigma_L\Big]. \end{aligned} \tag{8.5}$$

Since the identification of the model parameters will be realised in this work using the yield locii of Figure 7.11 resulting from biaxial tests in the (O, L, T) plane and since no information on the influence of the component σ_{LT} is available for such tests, model parameters a_4, b_5, b_{10} are chosen to be equal to $1, 0$, and 0, respectively. These values are chosen because they correspond to an isotropic material with von Mises yield criterion. The quantities J_2^o and J_3^o are finally rewritten as,

$$J_2^o = \frac{a_1}{6}\big(\sigma_L - \sigma_T\big)^2 + \frac{a_2}{6}\sigma_T^2 + \frac{a_3}{6}\sigma_L^2 + \sigma_{LT}^2, \tag{8.6}$$

and

$$J_3^o = \frac{1}{27}\big(b_1 + b_2\big)\sigma_L^3 + \frac{1}{27}\big(b_3 + b_4\big)\sigma_T^3 - \frac{1}{9}b_1\sigma_T\sigma_L^2 - \frac{1}{9}b_4\sigma_L\sigma_T^2. \tag{8.7}$$

The yield criterion in the plane stress case is thus defined by 7 model parameters only: $\{a_1, a_2, a_3, b_1, b_2, b_3, b_4\}$. The yield stress in pure shear τ_Y will be expressed by the yield strength σ_{YL} as measured from the uniaxial tension test in L-direction. The yield condition of this uniaxial test simplifies to,

$$\Phi = \sigma_{YL}^3\left(\left[\frac{1}{6}\big(a_1 + a_3\big)\right]^{\frac{3}{2}} - \frac{1}{27}\big(b_1 + b_2\big)\right) - \tau_Y^3 = 0, \tag{8.8}$$

which gives the following formulation for τ_Y,

$$\tau_Y = \sigma_{YL}\left(\left[\frac{1}{6}\big(a_1 + a_3\big)\right]^{\frac{3}{2}} - \frac{1}{27}\big(b_1 + b_2\big)\right)^{\frac{1}{3}}. \tag{8.9}$$

Because of its quadratic form, making yielding independent of the sign of σ_{ij}, J_2^o cannot describe the unlike yielding in tension and compression but is able to describe anisotropic yielding behavior if any $a_i \neq 1$, see Figure 8.1. The quantity J_3^o is therefore responsible for allowing to model the asymmetric yielding in tension and compression, as $b_i \neq 0$, because of its non quadratic form, see Figure 8.2 and Drucker [24].

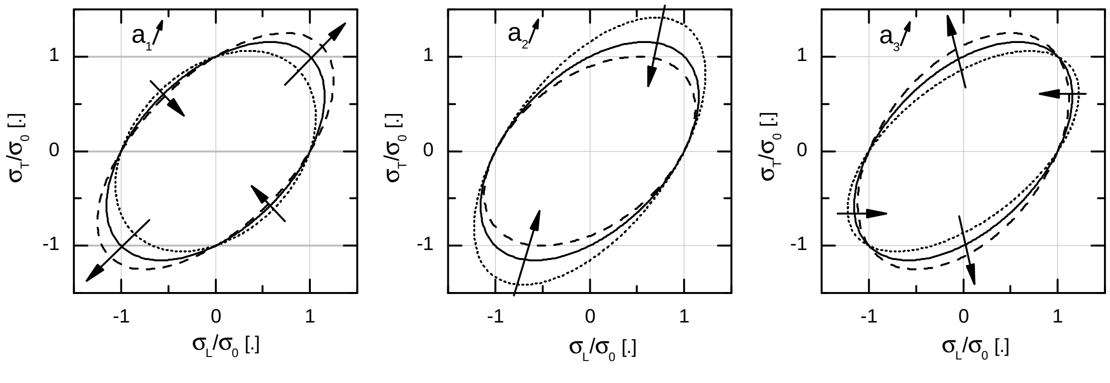

Figure 8.1: *Influence of model parameters a_i onto the yield surface shape. σ_0 is the yield stress for uniaxial tension in L-direction. Continous line represents von Mises yield locus ($a_i = 1$ and $b_i = 0$)*

Beside anisotropy and yielding asymmetry of the initial yield locus, Figure 7.11 also shows the yield locus changing its shape as the material hardens. As illustrated in Figure 4.2 of chapter 4, neither isotropic nor kinematic nor even a combination of both is able to account for this evolution of the shape of the yield surface in the course of hardening.
Another concept for strain-hardening therefore needs to be developed. In order to allow for the modeling of this phenomenon, a strain-hardening concept is adopted in this work in which the remaining model parameters $\{a_1, a_2, a_3, b_1, b_2, b_3, b_4\}$, in the plane stress case, are functions of an internal variable which is defined as a positive scalar value, the equivalent plastic strain after von Mises. As it is discussed in chapter 7 scalar values seems

not to be adequate candidates to describe the state of plastic deformation in Mg but the equivalent plastic strain is still chosen here for the sake of convenience.
In this concept, which is displayed in Figure 8.3, a yield locus defined for any given value of the equivalent plastic strain ϵ_p^n must be entirely inside the yield surface defined for another value of this plastic strain ϵ_p^{n+1} greater than ϵ_p^n. This condition of the yield locii is also satisfied in the case of isotropic hardening, but a uniform growth of the yield locus with increasing plastic strain, which is an additionnal property of isotropic hardening, is not required in the concept presented here.

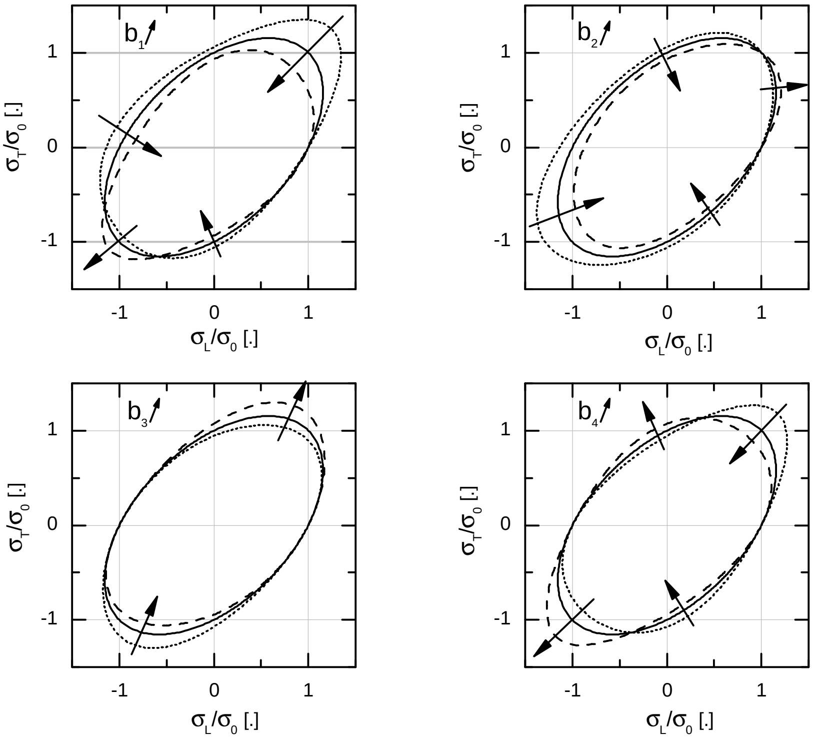

Figure 8.2: *Influence of model parameters b_i onto the yield surface shape. σ_0 is the yield stress for uniaxial tension in L-direction. Continous line represents von Mises yield locus ($a_i = 1$ and $b_i = 0$)*

Since this strain-hardening concept allows for considering yield surfaces evolving with increasing plastic strain, mechanical behavior like deformation-induced anisotropy may be modeled and phenomena like flow localisation may be predicted more reliably. These features are extremely attractive in modeling plastic deformations for engineering applications. This advantage is nevertheless restricted to applications in which the material point is subjected to monotonic loading since no strain-hardening similar to kinematic hardening is considered here.

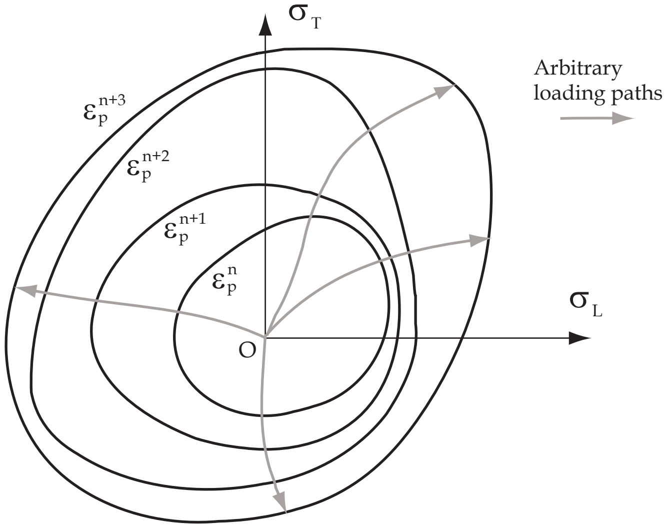

Figure 8.3: *Evolution of the strain-hardening concept with model parameters depending on plastic strain for arbitrary loading paths*

8.2 Mathematical Existence of the Yield Function and Yield Surface Convexity

The identification of model parameters for the yield surface of equation 8.1 has to be done ensuring the mathematical existence and convexity of the yield surface. Since the model parameters $\{a_i, b_i\}$ are functions of the scalar internal variable ϵ_p, the equivalent plastic strain after von Mises, the existence and convexity of the yield surface has to be checked for all values of the plastic strain.

It is first assumed that τ_Y is a positive monotonic function increasing with plastic strain. Since the relation $\tau_Y > 0$ must be true for all values of plastic strain it implies that,

$$\tau_Y = \left[\left(J_2^o \right)^{\frac{3}{2}} - J_3^o \right]^{\frac{1}{3}} \geq 0 \tag{8.10}$$

and therefore,

$$\left(J_2^o \right)^{\frac{3}{2}} - J_3^o \geq 0; \tag{8.11}$$

which requires that $J_2^0 \geq 0$ resulting in the condition,

$$J_2^o = \frac{a_1}{6} \left(\sigma_L - \sigma_T \right)^2 + \frac{a_2}{6} \sigma_T^2 + \frac{a_3}{6} \sigma_L^2 + \sigma_{LT}^2 \geq 0 \tag{8.12}$$

in the plane stress case. Both conditions 8.11 and 8.12 have hence to be fulfilled to ensure the existence of the yield function, and the model parameters have to be chosen appropriately for all values of the plastic strain $\epsilon_p \in [0, \infty[$.

After Rockafellar [67], in order to ensure convexity of the yield surface the Hessian matrix of the yield function Φ must be positive semi-definite with respect to the principal stresses. The Hessian $\mathbf{H}$ of a function $f\left(x_1, x_2, ..., x_n\right)$ with respect to $x_1, x_2, ..., x_n$ is the Jacobian matrix of the derivatives $\Big(\dfrac{\partial f}{\partial x_1}, \dfrac{\partial f}{\partial x_2}, ..., \dfrac{\partial f}{\partial x_n}\Big)$, i.e.,

$$\mathbf{H} = \left(\begin{array}{ccccc} \dfrac{\partial^2 f}{\partial {x_1}^2} & \dfrac{\partial^2 f}{\partial x_1 \partial x_2} & \dfrac{\partial^2 f}{\partial x_1 \partial x_3} & \cdots & \dfrac{\partial^2 f}{\partial x_1 \partial x_n} \\ \dfrac{\partial^2 f}{\partial x_2 \partial x_1} & \dfrac{\partial^2 f}{\partial {x_2}^2} & \dfrac{\partial^2 f}{\partial x_2 \partial x_3} & \cdots & \dfrac{\partial^2 f}{\partial x_2 \partial x_n} \\ \vdots & \vdots & \vdots & \ddots & \vdots \\ \dfrac{\partial^2 f}{\partial x_n \partial x_1} & \dfrac{\partial^2 f}{\partial x_n \partial x_2} & \dfrac{\partial^2 f}{\partial x_n \partial x_3} & \cdots & \dfrac{\partial^2 f}{\partial {x_n}^2} \end{array} \right). \tag{8.13}$$

In the plane stress case with biaxial loading in the (L, T)-plane, along L- and T-directions, the yield surface is a function of σ_L and σ_T only, which are the principal stresses. The Hessian matrix for this problem is therefore defined as,

$$\mathbf{H} = \left(\begin{array}{cc} H_{11} & H_{12} \\ H_{21} & H_{22} \end{array} \right) = \left(\begin{array}{cc} \dfrac{\partial^2 \Phi}{\partial {\sigma_L}^2} & \dfrac{\partial^2 \Phi}{\partial \sigma_L \partial \sigma_T} \\ \dfrac{\partial^2 \Phi}{\partial \sigma_T \partial \sigma_L} & \dfrac{\partial^2 \Phi}{\partial {\sigma_T}^2} \end{array} \right). \tag{8.14}$$

The components of the Hessian matrix are calculated as follows,

$$\left\{ \begin{array}{l} H_{11} = -\dfrac{2}{9}\big(b_1 + b_2\big)\sigma_L + \dfrac{2}{9} b_1 \sigma_T + \dfrac{3\Big(\dfrac{a_3}{3}\sigma_L + \dfrac{a_1}{3}\big(\sigma_L - \sigma_T\big)\Big)^2}{4\sqrt{\dfrac{a_3}{6}{\sigma_L}^2 + \dfrac{a_1}{6}\big(\sigma_L - \sigma_T\big)^2 + \dfrac{a_2}{6}{\sigma_T}^2}} \\ \qquad\qquad + \dfrac{1}{2}\big(a_1 + a_3\big)\sqrt{\dfrac{a_3}{6}{\sigma_L}^2 + \dfrac{a_1}{6}\big(\sigma_L - \sigma_T\big)^2 + \dfrac{a_2}{6}{\sigma_T}^2} \\ \\ H_{22} = \dfrac{2}{9} b_4 \sigma_L - \dfrac{2}{9}\big(b_3 + b_4\big)\sigma_T + \dfrac{3\Big(\dfrac{a_3}{3}\sigma_T + \dfrac{a_1}{3}\big(\sigma_L - \sigma_T\big)\Big)^2}{4\sqrt{\dfrac{a_3}{6}{\sigma_L}^2 + \dfrac{a_1}{6}\big(\sigma_L - \sigma_T\big)^2 + \dfrac{a_2}{6}{\sigma_T}^2}} \\ \qquad\qquad + \dfrac{1}{2}\big(a_1 + a_2\big)\sqrt{\dfrac{a_3}{6}{\sigma_L}^2 + \dfrac{a_1}{6}\big(\sigma_L - \sigma_T\big)^2 + \dfrac{a_2}{6}{\sigma_T}^2} \\ \\ H_{12} = H_{21} = \dfrac{2}{9} b_1 \sigma_L + \dfrac{2}{9} b_4 \sigma_T + \dfrac{3\dfrac{a_3}{3}\sigma_L + \dfrac{a_1}{3}\big(\sigma_L - \sigma_T\big)\Big(\dfrac{a_2}{3}\sigma_T - \dfrac{a_1}{3}\big(\sigma_L - \sigma_T\big)\Big)}{4\sqrt{\dfrac{a_3}{6}{\sigma_L}^2 + \dfrac{a_1}{6}\big(\sigma_L - \sigma_T\big)^2 + \dfrac{a_2}{6}{\sigma_T}^2}} \\ \qquad\qquad + \dfrac{a_1}{2}\sqrt{\dfrac{a_3}{6}{\sigma_L}^2 + \dfrac{a_1}{6}\big(\sigma_L - \sigma_T\big)^2 + \dfrac{a_2}{6}{\sigma_T}^2} \end{array} \right. .$$

(8.15)

To ensure the existence of each component H_{ij} the following condition has to be fullfilled,

$$\frac{a_3}{6}{\sigma_L}^2 + \frac{a_1}{6}\big(\sigma_L - \sigma_T\big)^2 + \frac{a_2}{6}{\sigma_T}^2 > 0, \tag{8.16}$$

which is equivalent to the condition described in equation 8.12 as $\sigma_{LT} = 0$. From the equation, $det\big(\mathbf{H} - \lambda\mathbb{I}\big) = 0$, the eigenvalues of the Hessian matrix are calculated as,

$$\lambda_\pm = \frac{1}{2}\left[\big(H_{11} + H_{22}\big) \pm \sqrt{\big(H_{11} + H_{22}\big)^2 - 4\big(H_{11}H_{22} - {H_{12}}^2\big)}\right] \tag{8.17}$$

and the existence of the eigenvalues $\lambda_\pm$ is thus controlled by the condition,

$$\big(H_{11} + H_{22}\big)^2 - 4\big(H_{11}H_{22} - {H_{12}}^2\big) \geq 0. \tag{8.18}$$

As a resume, the three conditions described in equations 8.11, 8.12 and 8.18 need to be fullfilled in order to obtain a physically meaningfull yield surface. Additionally, the conditions $\lambda_- \geq 0$ and $\lambda_+ \geq 0$ assure the yield surface to be convex in the (L, T)-plane. Since the model parameters are assumed to be functions of the equivalent plastic strain ϵ_p, all these restrictions must be taken into consideration for the identification of model parameters in the whole range of plastic strains $\epsilon_p \in [0, \infty[$.

8.3 Numerical Implementation of the Yield Criterion

8.3.1 Kinematics

In continuum mechanics the deformation gradient $\mathbf{F}$ as basic kinematic variable is defined by

$$\mathbf{F} = \frac{\partial \mathbf{x}}{\partial \mathbf{X}} \tag{8.19}$$

where $\mathbf{x}$ and $\mathbf{X}$ are the position vectors of the material point in the current and reference configuration, respectively. The velocity gradient tensor $\mathbf{L}$ in the current configuration is defined as,

$$\mathbf{L} = \dot{\mathbf{F}}\mathbf{F}^{-1} = \mathbf{D} + \boldsymbol{\Omega}, \tag{8.20}$$

where $\mathbf{D}$ and $\boldsymbol{\Omega}$ denote the symmetric and antisymmetric part of $\mathbf{L}$, respectively. These tensors are obtained from,

$$\mathbf{D} = \frac{1}{2}\big(\mathbf{L} + \mathbf{L}^T\big) \quad \text{and} \quad \boldsymbol{\Omega} = \frac{1}{2}\big(\mathbf{L} - \mathbf{L}^T\big) \tag{8.21}$$

where $\mathbf{L}^T$ denotes the transposed of tensor $\mathbf{L}$. Since the rate of the deformation tensor $\mathbf{D}$ is an objective tensor it is taken as strain measure in the constitutive relations. During elastic-plastic deformation the elastic strains are assumed to be small compared to the plastic ones which makes the additive decomposition of the strain rates into an elastic and plastic part acceptable. The strain rate tensor is therefore written as,

$$\mathbf{D} = \mathbf{D}^e + \mathbf{D}^p \tag{8.22}$$

where $\mathbf{D}^e$ and $\mathbf{D}^p$ are the elastic and plastic parts of the strain rate tensor, respectively. The stress measures used in the constitutive relations are the Cauchy stress tensor,

$$\boldsymbol{\sigma} = \sigma_{ij}\mathbf{e}_i \otimes \mathbf{e}_j \quad \text{and its Jaumann rate} \quad \overset{\nabla}{\boldsymbol{\sigma}} = \overset{\nabla}{\sigma}_{ij}\mathbf{e}_i \otimes \mathbf{e}_j. \tag{8.23}$$

The symbol $\mathbf{e}_k$ denotes the unit vectors of the Cartesian coordinate system related to the current configuration. The spin tensor $\boldsymbol{\Omega}$ links the Cauchy stress and its Jaumann rate through the equation,

$$\overset{\nabla}{\boldsymbol{\sigma}} = \dot{\boldsymbol{\sigma}} - \boldsymbol{\Omega}\boldsymbol{\sigma} + \boldsymbol{\sigma}\boldsymbol{\Omega} \tag{8.24}$$

where $\dot{\boldsymbol{\sigma}}$ is the time derivative of the Cauchy stress tensor.

8.3.2 Constitutive relations

Depending on the value of the yield function Φ, a material volument element may deform elastically $\Phi < 0$, or elasto-plastically, $\Phi = 0$. In both cases, the elastic part of the deformation rate is assumed to follow Hooke's law. The Jaumann rate of the Cauchy stress tensor is thus,

$$\overset{\nabla}{\boldsymbol{\sigma}} = \mathbb{C}^e : \mathbf{D}^e \tag{8.25}$$

where $\mathbb{C}^e$ is the fourth order tensor of elastic moduli. The integration of equation 8.25 is performed in a corotational way as described in [38] which allows for writing the strain tensor $\mathbf{E}$ as

$$\mathbf{E} = \mathbf{E}^e + \mathbf{E}^p \tag{8.26}$$

where $\mathbf{E}^e$ and $\mathbf{E}^p$ are the elastic and plastic parts of the strain tensor, respectively. The Cauchy stress tensor is thus given as

$$\boldsymbol{\sigma} = \mathbb{C}^e : \mathbf{E}^e = \mathbb{C}^e : \big(\mathbf{E} - \mathbf{E}^p\big). \tag{8.27}$$

Plastic deformation is assumed to be governed by an associated flow rule, see equation 4.6 in chapter 4. By assuming that plastic deformation can be reduced to a single scalar value derived from Odqvist's parameter p [60] defined as,

$$p = \int_0^t \sqrt{\mathbf{D}^p : \mathbf{D}^p}dt \quad \text{where} \quad \dot{p} = \sqrt{\mathbf{D}^p : \mathbf{D}^p}, \tag{8.28}$$

the equivalent plastic strain rate $\dot{\epsilon_p}$ of expression,

$$\dot{\epsilon_p} = \sqrt{\frac{2}{3}}\big(\mathbf{D}^p : \mathbf{D}^p\big)^{\frac{1}{2}} \tag{8.29}$$

is introduced into the constitutive equations. This definition of the equivalent plastic strain rate is traditionally used in J_2-plasticity in order to express plastic dissipation in terms of the equivalent von Mises stress and plastic strain. This definition is chosen here for the sake of convenience because of the lack of a better one adapted to anisotropic yielding. By combining now equations 4.6 and 8.29 we can write,

$$\dot{\epsilon}_p = \dot{\lambda}\sqrt{\frac{2}{3}}\left(\frac{\partial\Phi}{\partial\boldsymbol{\sigma}} : \frac{\partial\Phi}{\partial\boldsymbol{\sigma}}\right)^{\frac{1}{2}}. \tag{8.30}$$

Finally, the plastic multiplier is eliminated from the contitutive equations by inserting equation 8.30 into equation 4.6 such that the plastic strain rate tensor becomes,

$$\mathbf{D}^p = \frac{\dfrac{\partial\Phi}{\partial\boldsymbol{\sigma}}\dot{\epsilon}_p}{\sqrt{\dfrac{2}{3}}\left(\dfrac{\partial\Phi}{\partial\boldsymbol{\sigma}} : \dfrac{\partial\Phi}{\partial\boldsymbol{\sigma}}\right)^{\frac{1}{2}}}. \tag{8.31}$$

The yield condition and the related consistency condition can be written in a general form as,

$$\Phi(\boldsymbol{\sigma}, \epsilon_p) = f(\boldsymbol{\sigma}, \epsilon_p) - h(\epsilon_p) = 0 \tag{8.32}$$

and

$$\dot{\Phi} = \frac{\partial f}{\partial\boldsymbol{\sigma}} : \overset{\nabla}{\boldsymbol{\sigma}} + \frac{\partial f}{\partial\epsilon_p}\dot{\epsilon}_p - \frac{dh}{d\epsilon_p}\dot{\epsilon}_p = 0, \tag{8.33}$$

respectively. Here f is a function of the stress tensor $\boldsymbol{\sigma}$ and the equivalent plastic strain ϵ_p while h is a function of the equivalent plastic strain only. For the yield criterion of equation 8.1 the functions f and h are defined as,

$$f = (J_2^o)^{\frac{3}{2}} - J_3^o \quad \text{and} \quad h = \tau_Y^3 \tag{8.34}$$

where the quantities J_2^o, J_3^o and τ_Y are defined in equations 8.2, 8.3 and 8.9, respectively. In these equations the model parameters a_i and b_i are functions of the equivalent plastic strain ϵ_p.

Rewriting the consistency equation 8.33 including Hooke's law 8.25, the strain rate decomposition 8.22 as well as equations 4.6 and 8.30, and using $\dfrac{\partial\Phi}{\partial\boldsymbol{\sigma}} = \dfrac{\partial f}{\partial\boldsymbol{\sigma}}$ following from equation 8.32, the expression below is obtained,

$$\frac{\partial f}{\partial\boldsymbol{\sigma}} : \left[\mathbb{C}^e : \left(\mathbf{D} - \dot{\lambda}\frac{\partial f}{\partial\boldsymbol{\sigma}}\right)\right] + \frac{\partial f}{\partial\epsilon_p}\dot{\lambda}\sqrt{\frac{2}{3}}\left(\frac{\partial f}{\partial\boldsymbol{\sigma}} : \frac{\partial f}{\partial\boldsymbol{\sigma}}\right)^{\frac{1}{2}} - \frac{dh}{d\epsilon_p}\dot{\lambda}\sqrt{\frac{2}{3}}\left(\frac{\partial f}{\partial\boldsymbol{\sigma}} : \frac{\partial f}{\partial\boldsymbol{\sigma}}\right)^{\frac{1}{2}} = 0. \tag{8.35}$$

From this expression the plastic multiplier can be identified as,

$$\dot{\lambda} = \frac{\dfrac{\partial f}{\partial\boldsymbol{\sigma}} : [\mathbb{C}^e : \mathbf{D}]}{\left[\dfrac{\partial f}{\partial\boldsymbol{\sigma}} : \left(\mathbb{C}^e : \dfrac{\partial f}{\partial\boldsymbol{\sigma}}\right) - \sqrt{\dfrac{2}{3}}\left(\dfrac{\partial f}{\partial\boldsymbol{\sigma}} : \dfrac{\partial f}{\partial\boldsymbol{\sigma}}\right)^{\frac{1}{2}}\left[\dfrac{\partial f}{\partial\epsilon_p} - \dfrac{dh}{d\epsilon_p}\right]\right]}. \tag{8.36}$$

Inserting now equation 8.36 for the plastic multiplier into Hooke's law 8.25 the following expression is obtained,

$$\overset{\nabla}{\boldsymbol{\sigma}} = \mathbb{C}^e : \left[\mathbf{D} - \frac{\dfrac{\partial f}{\partial \boldsymbol{\sigma}} : [\mathbb{C}^e : \mathbf{D}]}{\left[\dfrac{\partial f}{\partial \boldsymbol{\sigma}} : \left(\mathbb{C}^e : \dfrac{\partial f}{\partial \boldsymbol{\sigma}} \right) - \sqrt{\dfrac{2}{3}} \left(\dfrac{\partial f}{\partial \boldsymbol{\sigma}} : \dfrac{\partial f}{\partial \boldsymbol{\sigma}} \right)^{\frac{1}{2}} \left[\dfrac{\partial f}{\partial \epsilon_p} - \dfrac{dh}{d\epsilon_p} \right] \right]} \frac{\partial f}{\partial \boldsymbol{\sigma}} \right]. \tag{8.37}$$

After some manipulations this last expression can be rewritten as,

$$\overset{\nabla}{\boldsymbol{\sigma}} = \left[\mathbb{C}^e - \frac{\mathbb{C}^e : \dfrac{\partial f}{\partial \boldsymbol{\sigma}} \otimes \dfrac{\partial f}{\partial \boldsymbol{\sigma}} : \mathbb{C}^e}{\left[\dfrac{\partial f}{\partial \boldsymbol{\sigma}} : \left(\mathbb{C}^e : \dfrac{\partial f}{\partial \boldsymbol{\sigma}} \right) - \sqrt{\dfrac{2}{3}} \left(\dfrac{\partial f}{\partial \boldsymbol{\sigma}} : \dfrac{\partial f}{\partial \boldsymbol{\sigma}} \right)^{\frac{1}{2}} \left[\dfrac{\partial f}{\partial \epsilon_p} - \dfrac{dh}{d\epsilon_p} \right] \right]} \right] : \mathbf{D}. \tag{8.38}$$

Finally, the elastic-plastic tangent modulus can be identified from the latter expression as,

$$\mathbb{C}^{ep} = \mathbb{C}^e - \frac{\mathbb{C}^e : \dfrac{\partial f}{\partial \boldsymbol{\sigma}} \otimes \dfrac{\partial f}{\partial \boldsymbol{\sigma}} : \mathbb{C}^e}{\dfrac{\partial f}{\partial \boldsymbol{\sigma}} : \left(\mathbb{C}^e : \dfrac{\partial f}{\partial \boldsymbol{\sigma}} \right) - \sqrt{\dfrac{2}{3}} \left(\dfrac{\partial f}{\partial \boldsymbol{\sigma}} : \dfrac{\partial f}{\partial \boldsymbol{\sigma}} \right)^{\frac{1}{2}} \left[\dfrac{\partial f}{\partial \epsilon_p} - \dfrac{dh}{d\epsilon_p} \right]}. \tag{8.39}$$

8.3.3 Numerical Integration of the Constitutive Equations

The algorithm for the numerical integration of the constitutive equations presented in the previous section is summarised in Figure 8.4 and described in detail in the following:

Step A

A strain-controlled problem is assumed in which the strain increment tensor $\Delta\mathbf{E}$ between time t and $t + \Delta t$ is known. Also known are the state of all stress and strain quantities at time t. The aim of the numerical integration is to solve for the values of all stress and strain quantities at time $t + \Delta t$.

Due to the complexity of simultaneously integrating the evolution equations presented in previous section, a numerical technique is used here. A fully implicit Euler backward scheme is chosen for this integration because of its unconditional stability which allows for the use of relatively large time increments compared to an explicit integration method. This consists in establishing all the equations constituing the problem with unknown expressed only at time $t + \Delta t$. The stresses and strains at time $t + \Delta t$ are expressed as,

$$^{t+\Delta t}\boldsymbol{\sigma} = {}^{t}\boldsymbol{\sigma} + {}^{t}\Delta\boldsymbol{\sigma}, \quad ^{t+\Delta t}\mathbf{E} = {}^{t}\mathbf{E} + {}^{t}\Delta\mathbf{E} \quad \text{and} \quad ^{t+\Delta t}\mathbf{E}^p = {}^{t}\mathbf{E}^p + {}^{t}\Delta\mathbf{E}^p. \tag{8.40}$$

where the tensors ${}^{t}\boldsymbol{\sigma}$, ${}^{t}\mathbf{E}$ and ${}^{t}\mathbf{E}^p$ are expressed in the current configuration.

Step B
It is assumed first that the deformation increment is of pure elastic nature which leads after equation 8.25 and 8.26 to the trial predictor stress,

$$ {}^{t+\Delta t}\boldsymbol{\sigma}^{tr} = {}^{t}\boldsymbol{\sigma} + \mathbb{C}^{e} : \left({}^{t+\Delta t}\mathbf{E} - {}^{t}\mathbf{E}^{p} \right) \tag{8.41} $$

and to the expressions for the trial plastic strains,

$$ {}^{t+\Delta t}{\epsilon_p}^{tr} = {}^{t}\epsilon_p \quad \text{and} \quad {}^{t+\Delta t}\mathbf{E}^{ptr} = {}^{t}\mathbf{E}^{p}. \tag{8.42} $$

For these trial values of stresses and plastic strain at time $t + \Delta t$ the yield condition of equation 8.32 is then evaluated. In the following steps almost all quantities are expressed at time $t+\Delta t$ and the corresponding superscripts ${}^{t+\Delta t}$ are omitted to simplify the notation.

Step C
If the inequation,

$$ \Phi^{tr} = f\left(\boldsymbol{\sigma}^{tr}, {\epsilon_p}^{tr}\right) - h\left({\epsilon_p}^{tr}\right) \leq 0, \tag{8.43} $$

is true then the strain increment is accepted as purely elastic and the variables at time $t + \Delta t$ are updated to $\boldsymbol{\sigma} = \boldsymbol{\sigma}^{tr}$ and $\epsilon_p = {\epsilon_p}^{tr}$. The elastic-plastic tangeant modulus is also updated to the elastic modulus $\mathbb{C}^{ep} = \mathbb{C}^{e}$.

Step D
If the inequation 8.43 is not satisfied the strain increment is not of purely elastic nature and plastic deformation occurs, which requires that the relations $\Phi_{n+1} = 0$ and $\boldsymbol{\sigma} = \mathbb{C}^{e} : \mathbf{E}^{e}$ are satisfied. The following system of equations needs thus to be solved,

$$ \left\{ \begin{array}{l} \Phi = f\left(\boldsymbol{\sigma}, \epsilon_p\right) - h\left(\epsilon_p\right) = 0 \\ \boldsymbol{\Gamma} = \boldsymbol{\sigma} - \ \mathbb{C}^{e} : \left(\mathbf{E} - \dfrac{\dfrac{\partial f}{\partial \boldsymbol{\sigma}} \epsilon_p}{\sqrt{\dfrac{2}{3}} \left[\dfrac{\partial f}{\partial \boldsymbol{\sigma}} : \dfrac{\partial f}{\partial \boldsymbol{\sigma}} \right]^{\frac{1}{2}}} \right) = 0 \end{array} \right. , \tag{8.44} $$

where the plastic strain tensor $\mathbf{E}^{p}$ has been replaced by the following expression after corotationnal integration of equation 8.31,

$$ \mathbf{E}^{p} = \frac{\dfrac{\partial f}{\partial \boldsymbol{\sigma}} \epsilon_p}{\sqrt{\dfrac{2}{3}} \left(\dfrac{\partial f}{\partial \boldsymbol{\sigma}} : \dfrac{\partial f}{\partial \boldsymbol{\sigma}} \right)^{\frac{1}{2}}}. \tag{8.45} $$

The variable $\boldsymbol{\Gamma}$ is introduced to simplify future notations. The total increment of strain $\mathbf{E}$ is known since a strain controlled problem is assumed. Since the hardening state is assumed to be described by a single scalar value ϵ_p, the number of unknown for the system of equations to be solve at time $t + \Delta t$ is reduced to the equivalent plastic strain ϵ_p and the components σ_{ij} of stress tensor $\boldsymbol{\sigma}$. This system of nonlinear equations is solved

```
A. Initial desired values defined in the current configuration
        $\mathbb{C}^e, \quad {}^t\boldsymbol{\sigma}, \quad {}^t\epsilon_p, \quad {}^t\mathbf{E}, \quad {}^t\mathbf{E}^p$
B. Compute trial values for plastic strain, stresses and yield potential
        ${}^{t+\Delta t}{\epsilon_p}^{tr} = {}^t\epsilon_p$
        ${}^{t+\Delta t}\boldsymbol{\sigma}^{tr} = \mathbb{C}^e : \left({}^{t+\Delta t}\mathbf{E} - {}^t\mathbf{E}^p\right)$
        ${}^{t+\Delta t}\Phi^{tr} = f\left({}^{t+\Delta t}\boldsymbol{\sigma}^{tr}, {}^{t+\Delta t}{\epsilon_p}^{tr}\right) - h\left({}^{t+\Delta t}{\epsilon_p}^{tr}\right)$
In the following steps all quantities are expressed at time $t + \Delta t$ and the
corresponding superscripts ${}^{t+\Delta t}$ are omitted to simplify the notation
C. If $\Phi^{tr} \leq 0$, than elastic range
    C.1 Update equivalent plastic strain and stresses
        $\epsilon_p = {\epsilon_p}^{tr}$ and $\boldsymbol{\sigma} = \boldsymbol{\sigma}^{tr}$
    C.2 Update tangeant modulus
        $\mathbb{C}^{ep} = \mathbb{C}^e$ and go to E
D. If $\Phi^{tr} > 0$, than plastic range and $\Phi = 0$ and $\boldsymbol{\sigma} = \mathbb{C}^e : \mathbf{E}^e$ must be fullfilled
    D.1 Start values for Newton-Raphson iteration ($m = 0$)
        ${\epsilon_p}^{(0)} = {\epsilon_p}^{tr}$ and $\boldsymbol{\sigma}^{(0)} = \boldsymbol{\sigma}^{tr}$
    D.2 Compute the stress residues
        $\Phi^{(m)} = f\left(\boldsymbol{\sigma}^{(m)}, {\epsilon_p}^{(m)}\right) - h\left({\epsilon_p}^{(m)}\right)$
        $\boldsymbol{\Gamma}^{(m)} = \boldsymbol{\sigma}^{(m)} - \left[ \mathbb{C}^e : \left( \mathbf{E} - \frac{\frac{\partial f}{\partial \boldsymbol{\sigma}^{(m)}} {\epsilon_p}^{(m)}}{\sqrt{\frac{2}{3}} \left[ \frac{\partial f}{\partial \boldsymbol{\sigma}^{(m)}} : \frac{\partial f}{\partial \boldsymbol{\sigma}^{(m)}} \right]^{\frac{1}{2}}} \right) \right]$
    D.3 Compute the partial derivatives
        $\frac{\partial \boldsymbol{\Gamma}^{(m)}}{\partial \boldsymbol{\sigma}^{(m)}}, \quad \frac{\partial \boldsymbol{\Gamma}^{(m)}}{\partial {\epsilon_p}^{(m)}}, \quad \frac{\partial \Phi^{(m)}}{\partial \boldsymbol{\sigma}^{(m)}} \quad \text{and} \quad \frac{\partial \Phi^{(m)}}{\partial {\epsilon_p}^{(m)}}$
    D.4 Solve the system of nonlinear equations for ${}^t\Delta\boldsymbol{\sigma}^{(m)}$ and ${}^t\Delta{\epsilon_p}^{(m)}$
        $\begin{bmatrix} \frac{\partial \boldsymbol{\Gamma}^{(m)}}{\partial \boldsymbol{\sigma}^{(m)}} & \frac{\partial \boldsymbol{\Gamma}^{(m)}}{\partial {\epsilon_p}^{(m)}} \\ \frac{\partial \Phi^{(m)}}{\partial \boldsymbol{\sigma}^{(m)}} & \frac{\partial \Phi^{(m)}}{\partial {\epsilon_p}^{(m)}} \end{bmatrix} \begin{pmatrix} {}^t\Delta\boldsymbol{\sigma}^{(m)} \\ {}^t\Delta{\epsilon_p}^{(m)} \end{pmatrix} = \begin{pmatrix} -\boldsymbol{\Gamma}^{(m)} \\ -\Phi^{(m)} \end{pmatrix}$
    D.5 Update equivalent plastic strain and stresses
        ${\epsilon_p}^{(m+1)} = {\epsilon_p}^{(m)} + {}^t\Delta{\epsilon_p}^{(m)}$ and $\boldsymbol{\sigma}^{(m+1)} = \boldsymbol{\sigma}^{(m)} + {}^t\Delta\boldsymbol{\sigma}^{(m)}$
    D.6 If $\Phi^{(m+1)}$ >Tolerance, than iterate again
        $m = m + 1$ and go to D.2
    D.7 If $\Phi^{(m+1)}$ <Tolerance, than update tangeant modulus
        $\mathbb{C}^{ep} = \mathbb{C}^e - \frac{\mathbb{C}^e : \frac{\partial f}{\partial \boldsymbol{\sigma}^{(m+1)}} \otimes \frac{\partial f}{\partial \boldsymbol{\sigma}^{(m+1)}} : \mathbb{C}^e}{\frac{\partial f}{\partial \boldsymbol{\sigma}^{(m+1)}} : \left( \mathbb{C}^e : \frac{\partial f}{\partial \boldsymbol{\sigma}^{(m+1)}} \right) - \sqrt{\frac{2}{3}} \left( \frac{\partial f}{\partial \boldsymbol{\sigma}^{(m+1)}} : \frac{\partial f}{\partial \boldsymbol{\sigma}^{(m+1)}} \right)^{\frac{1}{2}} \left[ \frac{\partial f}{\partial {\epsilon_p}^{(m+1)}} - \frac{dh}{d{\epsilon_p}^{(m+1)}} \right]}$
E. All desired values are defined at $t + \Delta t$, return results
```

Figure 8.4: *Algorithm for the numerical integration of the yield criterion described in equation 8.1 with strain-hardening concept presented in this chapter between time t and* $t + \Delta t$

numerically by use of an iterative Newton-Raphson method. This method is chosen because of its desired properties when iteration is started relatively close to the solution. Indeed, its order of convergence is two.

The Newton-Raphson method consists in solving the following new system of equations for ${}^t\Delta\boldsymbol{\sigma}$ and ${}^t\Delta\epsilon_p$,

$$\begin{bmatrix} \dfrac{\partial\boldsymbol{\Gamma}^{(m)}}{\partial\boldsymbol{\sigma}^{(m)}} & \dfrac{\partial\boldsymbol{\Gamma}^{(m)}}{\partial{\epsilon_p}^{(m)}} \\ & \\ \dfrac{\partial\Phi^{(m)}}{\partial\boldsymbol{\sigma}^{(m)}} & \dfrac{\partial\Phi^{(m)}}{\partial{\epsilon_p}^{(m)}} \end{bmatrix} \begin{pmatrix} {}^t\Delta\boldsymbol{\sigma}^{(m)} \\ \\ {}^t\Delta{\epsilon_p}^{(m)} \end{pmatrix} = \begin{pmatrix} -\boldsymbol{\Gamma}^{(m)} \\ \\ -\Phi^{(m)} \end{pmatrix}. \tag{8.46}$$

The superscript ${}^{(m)}$ indicates the m^{th} iteration of the Newton-Raphson scheme. The initial values for the Newton-Raphson scheme ($m = 0$) are,

$$\boldsymbol{\Gamma}^{(0)} = \boldsymbol{\Gamma}^{tr} = 0 \quad \text{and} \quad \Phi^{(0)} = \Phi^{tr} \neq 0$$

with

$$\boldsymbol{\sigma}^{(0)} = \boldsymbol{\sigma}^{tr} \quad \text{and} \quad {\epsilon_p}^{(0)} = {\epsilon_p}^{tr}.$$

Since the terms resulting from the derivations in equation 8.46 are especially long they are not presented here but developed in detail in Appendix B.

This new system of equations is solved with the help of the Gauss-Jordan method for ${}^t\Delta\boldsymbol{\sigma}$ and ${}^t\Delta\epsilon_p$ and the variables are updated to,

$$\begin{cases} \boldsymbol{\sigma}^{(m+1)} = \boldsymbol{\sigma}^{(m)} + {}^t\Delta\boldsymbol{\sigma} \\ {\epsilon_p}^{(m+1)} = {\epsilon_p}^{(m)} + {}^t\Delta\epsilon_p \end{cases} \tag{8.47}$$

If the yield condition of equation 8.32 evaluated at time $t + \Delta t$ is satisfied within a tolerance, the new variables values are accepted otherwise an additionnal iteration of the Newton-Raphson scheme is started until the yield condition is satisfied. When the yield condition is satisfied the elastic-plastic tangeant modulus at time $t + \Delta t$ is updated after equation 8.39 to,

$$\mathbb{C}^{ep} = \mathbb{C}^e - \frac{\mathbb{C}^e : \frac{\partial f}{\partial\boldsymbol{\sigma}^{(m+1)}} \otimes \frac{\partial f}{\partial\boldsymbol{\sigma}^{(m+1)}} : \mathbb{C}^e}{\frac{\partial f}{\partial\boldsymbol{\sigma}^{(m+1)}} : \left(\mathbb{C}^e : \frac{\partial f}{\partial\boldsymbol{\sigma}^{(m+1)}}\right) - \sqrt{\frac{2}{3}}\left(\frac{\partial f}{\partial\boldsymbol{\sigma}^{(m+1)}} : \frac{\partial f}{\partial\boldsymbol{\sigma}^{(m+1)}}\right)^{\frac{1}{2}} \left[\frac{\partial f}{\partial{\epsilon_p}^{(m+1)}} - \frac{dh}{d{\epsilon_p}^{(m+1)}}\right]}. \tag{8.48}$$

8.4 Plastic Strain Anisotropy and Lankford Parameters

For a sheet the anisotropy of plastic deformation with loading direction is generally quantified with Lankford parameters or, also called, anisotropy coefficients. The Lankford parameter, R, is determined by uniaxial tension tests in the (L,T)-plane of the sheet for various values of θ, the angle between the specimen tensile direction and the longitudinal direction of the sheet. The Lankford parameter is defined as

$$R = \frac{\epsilon_w}{\epsilon_t} \quad \text{where} \quad \epsilon_w = ln\Big(\frac{w_1}{w_0}\Big) \quad \text{and} \quad \epsilon_t = ln\Big(\frac{t_1}{t_0}\Big), \tag{8.49}$$

after ASTM Standards [9]. The character w and t denote the width and thickness, respectively, of the tested sample. And the subscripts $_0$ and $_1$ denote their initial and current dimensions, respectively.

An isotropic material corresponds to a Lankford parameter equal to 1. Usually, the sheets destined to forming processes are desired to show high Lankford coefficients. Indeed high R values denote higher plastic deformation in the sheet's width than in its thickness, which avoids failure of the sheet during the forming process.

8.5 Identification of Model Parameters for the Yield Criterion

In this section we would like to identify model parameters for the yield surface of equation 8.1. The simulation results of biaxial tests presented in Figure 7.11 constitute the reference yield surfaces for the identification of the desired model parameters. In order to obtain the best correspondance between deformation and stress tensors $\big(\mathbf{E}^p, \boldsymbol{\sigma}\big)$, the identified model parameters should reproduce simultaneously the shapes of the reference yield surfaces in the (L, T)-plane for different values of the equivalent plastic strain, and the anisotropy of plastic deformation in the (L, T)-plane. The identification problem is defined as the minimization of a target function Υ. This target function which has to be minimized, has hence to include not only stress levels $\bar{\sigma}$ but also plastic strain ratios $\bar{r}$, and is expressed as,

$$\Upsilon = \sum_j \sum_k \Big[{}^{jk}\mu^{\bar{\sigma}} \big({}^{jk}\bar{\sigma}^{set} - {}^{jk}\bar{\sigma}^{ref} \big)^2 + {}^{jk}\mu^{\bar{r}} \big({}^{jk}\bar{r}^{set} - {}^{jk}\bar{r}^{ref} \big)^2 \Big], \tag{8.50}$$

where ${}^{jk}\mu^{\bar{\sigma}}$ and ${}^{jk}\mu^{\bar{r}}$ are weight factors. The superscripts ^{ref} and ^{set} denote the couple of stresses belonging to the reference yield surfaces, generated via biaxial tests, and those belonging to a given set of model parameters generated by the optimisation procedure, respectively. The superscripts ^{j} and ^{k} denote the different values of plastic strain considered for the isocontours and the different loading paths considered in biaxial testing, respectively. For each combination of ^{j} and ^{k} a strain ratio ${}^{jk}\bar{r}$ as well as a stress value ${}^{jk}\bar{\sigma}$ are considered in order to define the target function to be minimized. The stress values ${}^{jk}\bar{\sigma}^{ref}$ and ${}^{jk}\bar{\sigma}^{set}$ in 8.50 are defined as,

$${}^{jk}\bar{\sigma}^{ref} = \sqrt{{}^{jk}\sigma_L{}^{ref^2} + {}^{jk}\sigma_T{}^{ref^2}} \quad \text{and} \quad {}^{jk}\bar{\sigma}^{set} = \sqrt{{}^{jk}\sigma_L{}^{set2} + {}^{jk}\sigma_T{}^{set2}}, \tag{8.51}$$

where $\big\{{}^{jk}\sigma_L, {}^{jk}\sigma_T\big\}$ is the couple of stresses in L- and T-directions corresponding to the j^{th} isocontour and the k^{th} loading path. The strain ratios ${}^{jk}\bar{r}^{ref}$ and ${}^{jk}\bar{r}^{set}$ denote the anisotropy of plastic deformation in the (L, T)-plane, corresponding to the j^{th} isocontour and the k^{th} loading path, and are defined as,

$$^{jk}\bar{r}^{ref} = \frac{{E^p}_{LL}{}^{ref}}{{E^p}_{TT}{}^{ref}} \quad \text{and} \quad ^{jk}\bar{r}^{set} = \frac{{E^p}_{LL}{}^{set}}{{E^p}_{TT}{}^{set}}. \tag{8.52}$$

The quantities ${E^p}_{LL}$ and ${E^p}_{TT}$ are the plastic parts of the deformation in L- and T-direction, respectively, see equation 8.26. $^{jk}\bar{r}^{set}$ is thus defined as,

$$^{jk}\bar{r}^{set} = \int_0^t \frac{\partial \Phi}{\partial {}^{jk}\sigma_L} / \frac{\partial \Phi}{\partial {}^{jk}\sigma_T} dt \tag{8.53}$$

after equation 8.31. The ratio of plastic strain $^{jk}\bar{r}$ retained in the optimization procedure is different from the Lankford parameter R. Nevertheless, it is expected that the Lankford parameters predicted by the phenomenological model will be similar to those obtained with the crystal plasticity model due to volume constance of the plastic deformation.

A set of model parameters in the plane stress case is $\{a_1, a_2, a_3, b_1, b_2, b_3, b_4\}$ and is denoted $\bar{c}$ in the following. Each component $\bar{c}_i$ of this model parameter set is assumed to be a saturating exponential function of the plastic strain ϵ_p through equation,

$$\bar{c}_i(\epsilon_p) = A_i + B_i\Big(1 - e^{-C_i \epsilon_p}\Big). \tag{8.54}$$

In general, optimization problems can be solved by either deterministic or stochastic procedures, in which the target function is identical, see [15]. The problem of minimizing the target function Υ is not trivial as it exhibits multiple local minima. Thus the result of deterministic optimization procedures like Newton's method or gradient methods will depend on the starting model parameter set $\{a_1, a_2, a_3, b_1, b_2, b_3, b_4\}$ considered. A stochastic procedure is therefore necessary in the present case to minimize Υ. Such methods unfortunately result in high numerical costs because the target function is evaluated frequently.

In this work a stochastic optimization procedure specifically adapted to the present problem and based on a Monte-Carlo search has been developed. The optimization scheme is presented in Figure 8.5 and described in detail in the following:

Step A

At first some variables controling the optimization scheme are defined. Variables *GenMaxB* and *GenMaxD* defines the number of randomly generated parameter sets in step B and step D, respectively. Since the components $\bar{c}_i(\epsilon_p)$ of a model parameter set are assumed to be saturating exponential functions of the equivalent plastic strain, each defined by three constants A_i, B_i and C_i, the parameter set $\bar{c}(\epsilon_p)$ is fitted for only three values of the plastic strain $\epsilon_p(1)$, $\epsilon_p(2)$, $\epsilon_p(3)$. The values $\epsilon_p(1)$ and $\epsilon_p(3)$ should represent the greatest possible range, therefore the smallest and largest values available in Figure 7.11 should be chosen. $\epsilon_p(2)$ is an intermediate value which has to be defined. Variable N_B is an integer and identifies which of the plastic strains $\epsilon_p(1)$, $\epsilon_p(2)$, $\epsilon_p(3)$ is currently considered by the optimization procedure. Its initial value is put equal to zero. Variable *SavMax* is an integer defining the maximum number of parameter sets to be saved in next steps, as the given sets fulfil the restrictions of convexity developed previously.

Step B

The number of generated parameter sets $GenB$ is initialized to 1, variable N_B is incremented by 1 and vectors $\{\Lambda(\epsilon_p)\}$ and $\{\bar{c}(\epsilon_p)\}$ of length $SavMax$ are created.
The quantity $\{\Lambda(\epsilon_p)\}$ is another target function to minimize, similar to Υ, but for a constant value ϵ_p and is defined as,

$$\Lambda(\epsilon_p) = \sum_k \left[{}^k\mu^{\bar{\sigma}} \left({}^k\bar{\sigma}^{set} - {}^k\bar{\sigma}^{ref} \right)^2 + {}^k\mu^{\bar{r}} \left({}^k\bar{r}^{set} - {}^k\bar{r}^{ref} \right)^2 \right]. \tag{8.55}$$

A random model parameter set ${}^{GenB}\bar{c}(\epsilon_p)$ is than generated and the convexity of the corresponding yield surface is checked. Indeed, for a finite number of couples $\big(\sigma_L, \sigma_T\big)$, belonging to the yield surface, it this checked that the three conditions described in equations 8.11, 8.12 and 8.18 are fullfilled. Additionnaly it is checked that the eigenvalues of the yield condition's Hessian matrix are positive which ensures the yield surface to be convex in the (L, T)-plane, see previously in this chapter. If this yield surface is convex, the function ${}^{GenB}\Lambda(\epsilon_p)$ is evaluated and compared to the largest saved value up to now, ${}^{max}\Lambda(\epsilon_p) = max[\{\Lambda(\epsilon_p)\}]$. If the new value ${}^{GenB}\Lambda(\epsilon_p)$ is smaller than ${}^{max}\Lambda(\epsilon_p)$, then the model parameter set and the corresponding function value are updated to ${}^{max}\Lambda(\epsilon_p) = {}^{GenB}\Lambda(\epsilon_p)$ and ${}^{max}\bar{c}(\epsilon_p) ={}^{GenB}\ \bar{c}(\epsilon_p)$. As long as $GenMaxB$ is not reached, variable $GenB$ is incremented and step B is repeated except that the variables are not initialized anymore. This step is also repeated for all three values $\epsilon_p(1)$, $\epsilon_p(2)$ and $\epsilon_p(3)$, such that for each of the three values of plastic strain a number $SavMax$ of model parameter sets $\bar{c}$ and the corresponding values of the target function Λ are saved.

Step C

The coefficients $\{A_i, B_i, C_i\}$ are calculated for each of the possible combination of the sets components $\{\bar{c}_i(\epsilon_p(1))\}$, $\{\bar{c}_i(\epsilon_p(2))\}$ and $\{\bar{c}_i(\epsilon_p(3))\}$, saved in step B. This is $CombMax = SavMax^3$ combinations. For each of the combinations the convexity of the yield surfaces corresponding to the coefficients ${}^{Comb}\{A_i, B_i, C_i\}$ of the combination ${}^{Comb}\bar{c}_i$ checked for a number of values of $\epsilon_p \in [0, \epsilon_p(3)]$. If the yield surfaces are convex for all values of $\epsilon_p \in [0, \epsilon_p(3)]$ tested, the coefficients are accepted ${}^{Accp}\{A_i, B_i, C_i\}$, the corresponding target function ${}^{Comb}\Upsilon$ is evaluated and accepted ${}^{Accp}\Upsilon$, and the number of accepted combinations is incremented $Accp = Accp + 1$.

Step D

For each of the accepted combinations ${}^{Accp}\{A_i, B_i, C_i\}$ a certain number $GenD$ of parameters sets are generated randomly, with coefficients values ${}^{GenD}\{A_i, B_i, C_i\}$ in the neighborhood of ${}^{Accp}\{A_i, B_i, C_i\}$. This is realized in order to eventually get smaller values of the corresponding target function Υ, and to obtain thus an improved parameter set. As in step C the convexity of the yield surfaces corresponding to the coefficients ${}^{GenD}\{A_i, B_i, C_i\}$ is checked for a number values of $\epsilon_p \in [0, \epsilon_p(3)]$. If the yield surfaces are convex for all values of $\epsilon_p \in [0, \epsilon_p(3)]$ tested, the corresponding target function ${}^{GenD}\Upsilon$ is evaluated and compared to ${}^{Accp}\Upsilon$. If ${}^{GenD}\Upsilon$ is smaller than ${}^{Accp}\Upsilon$, then ${}^{Accp}\Upsilon$ and ${}^{Accp}\{A_i, B_i, C_i\}$ are both updated to ${}^{GenD}\Upsilon$ and ${}^{GenD}\{A_i, B_i, C_i\}$, respectively.

Step E

Finally, the optimal parameter set is chosen to be the one corresponding to the smallest value of the accepted target functions ${}^{min}\Upsilon = min[\{{}^{Accp}\Upsilon\}]$.

```
A. Define values for the whole optimization scheme
   $GenMaxB, \quad GenMaxD, \quad N_B = 0, \quad \epsilon_p(1), \quad \epsilon_p(2), \quad \epsilon_p(3), \quad SavMax$
B. Initialize values for step B
   $GenB = 1, \quad N_B = N_B + 1, \quad \epsilon_p = \epsilon_p(N_B),$
   $\{\Lambda(\epsilon_p)\} = \{{}^{1}\Lambda(\epsilon_p), \cdots, {}^{SavMax}\Lambda(\epsilon_p)\}, \quad \{\bar{c}(\epsilon_p)\} = \{{}^{1}\bar{c}(\epsilon_p), \cdots, {}^{SavMax}\bar{c}(\epsilon_p)\}$
   B.1 Generation of a random set of model parameters ${}^{GenB}\bar{c}(\epsilon_p)$
   B.2 Check convexity for ${}^{GenB}\bar{c}(\epsilon_p)$
   B.3 If yield surface convex, than accept ${}^{GenB}\bar{c}(\epsilon_p)$
      Evaluate ${}^{GenB}\Lambda(\epsilon_p)$
      ${}^{max}\Lambda(\epsilon_p) = max[\{\Lambda(\epsilon_p)\}]$
      B.3.1 If ${}^{GenB}\Lambda(\epsilon_p) < {}^{max}\Lambda(\epsilon_p)$, than update ${}^{max}\Lambda(\epsilon_p)$ and ${}^{max}\bar{c}(\epsilon_p)$
         ${}^{max}\Lambda(\epsilon_p) = {}^{GenB}\Lambda(\epsilon_p)$
         ${}^{max}\bar{c}(\epsilon_p) ={}^{GenB} \bar{c}(\epsilon_p)$
   B.4 If $GenB < GenMaxB$, than $GenB = GenB + 1$ and go to B.1
   B.5 If ($GenB = GenMaxB$ and $N_B \leq 2$), than go to B
C. Initialize values for step C
   $CombMax = SavMax^3, \quad Comb = 1, \quad Accp = 0$
   C.1 Calculate all components ${}^{Comb}\{A_i, B_i, C_i\}$ of ${}^{Comb}\bar{c}_i$
   C.2 Check convexity for ${}^{Comb}\{A_i, B_i, C_i\}$ at several $\epsilon_p \in [0, \epsilon_p(3)]$
   C.3 If yield surfaces convex for all $\epsilon_p$ checked, than accept combination
      Evaluate ${}^{Comb}\Upsilon$
      $Accp = Accp + 1$
      ${}^{Accp}\Upsilon = {}^{Comb}\Upsilon$
      ${}^{Accp}\{A_i, B_i, C_i\} = {}^{Comb}\{A_i, B_i, C_i\}$
   C.4 If $Comb < CombMax$, than $Comb = Comb + 1$ and go to C.1
D. Initialize values for step D
   $Accp = 1, \quad GenD = 1$
   D.1 Generate ${}^{GenD}\{A_i, B_i, C_i\}$ near to ${}^{Accp}\{A_i, B_i, C_i\}$
   D.2 Check convexity for ${}^{GenD}\{A_i, B_i, C_i\}$ at several $\epsilon_p \in [0, \epsilon_p(3)]$
   D.3 If yield surfaces convex for all $\epsilon_p$ checked, than variation accepted
      Evaluate ${}^{GenD}\Upsilon$
      D.3.1 If ${}^{GenD}\Upsilon < {}^{Accp}\Upsilon$, than update $\Upsilon$ and $\{A_i, B_i, C_i\}$
         ${}^{Accp}\Upsilon = {}^{GenD}\Upsilon$
         ${}^{Accp}\{A_i, B_i, C_i\} = {}^{GenD}\{A_i, B_i, C_i\}$
   D.4 If $GenD < GenMaxD$, than $GenD = GenD + 1$ and go to D.1
E. The optimal model parameter set is ${}^{min}\Upsilon = min[\{{}^{Accp}\Upsilon\}]$
```

Figure 8.5: *Optimisation scheme for identification of model parameters for the yield criterion of equation 8.1*

8.6 Optimisation of Model Parameters and Yield Surfaces

The optimisation procedure, described in the previous chapter, was not able to deliver satisfying results in terms of model parameter sets, which were able to predict both similar yield surfaces, ${}^{jk}\bar{\sigma}^{ref}$ values, and strain ratios, ${}^{ij}\bar{r}^{ref}$ values. This is discussed in the present chapter. The discussion is based on two model parameter sets, **Set1**, and **Set2** resulting from optimization procedures fitting only ${}^{jk}\bar{r}^{ref}$ and ${}^{jk}\bar{\sigma}^{ref}$, respectively. The weight coefficients, ${}^{jk}\mu^{\bar{\sigma}}$ and ${}^{jk}\mu^{\bar{r}}$ used in the optimisation procedure for **Set1** and **Set2** are given in Appendix C. The weight coefficients for **Set1** were chosen such that the Lankford parameters of a sheet may be reproduced. Since Lankford parameters are resulting from uniaxial tensile tests, weight coefficients were chosen different from zero only for the loading paths in the first quadrant of the (L, T)-plane, see Appendix C. The weight coefficients for **Set2** were chosen such that the beginning and the end of yielding may be well reproduced. In order to reproduce the complicated yield surfaces shapes of Figure 7.11 the weight coefficients were chosen higher, but different from each others, on the axes of the (L, T)-plane as well as on the four bisectrices, see Appendix C.
The values of the coefficients A, B, and C for both model parameter sets are listed in Tables 8.1 and 8.2, respectively, and the resulting yield surfaces are illustrated in Figure 8.6. The reference yield surfaces, already presented in Figure 7.11, are denoted **CP** in this chapter for Crystal Plasticity results. Table 8.3 reports the tabular data of the sheet's yielding behaviour in L-direction as a function of the equivalent plastic strain.

	a_1	a_2	a_3	b_1	b_2	b_3	b_4
A	1.1317	1.7154	7.2440	10.2247	2.7922	3.5075	0.2587
B	0.	0.	-5.7079	-12.1859	0.	0.	0.
C	0.	0.	164.7487	127.2557	0.	0.	0.

Table 8.1: *Coefficients A, B, and C of* **Set1** *describing model parameters as an exponential saturating function of the equivalent plastic strain, after equation 8.54*

	a_1	a_2	a_3	b_1	b_2	b_3	b_4
A	1.5499	1.9647	2.4252	3.6640	4.6835	4.8854	-5.0087
B	-1.5309	0.	0.	0.	-8.4050	-7.8393	6.0329
C	60.5688	0.	0.	0.	29.3242	20.0047	44.7950

Table 8.2: *Coefficients A, B, and C of* **Set2** *describing model parameters as an exponential saturating function of the equivalent plastic strain, after equation 8.54*

The yield surfaces of the material described by **Set1**, see on the lefthandside of Figure 8.6, are far away from the reference values, especially concerning the biaxial stress states. Almost only the stress levels for uniaxial tension in L- and T-direction are well reproduced. The yield surfaces of the material described by **Set2** on the righthandside instead, show a quite good agreement with the reference values. Almost only the stress levels at low strains, in uniaxial tension along T-direction, are far from the reference data. Both the yield surfaces from **Set1** and **Set2** do not describe accurately the stress levels at small strains in the third quadrant, which is due to the choice of the weight coefficients ${}^{jk}\mu^{\bar{\sigma}}$ and ${}^{k}\mu^{\bar{\sigma}}$ of equations 8.50 and 8.55, see Appendix C.

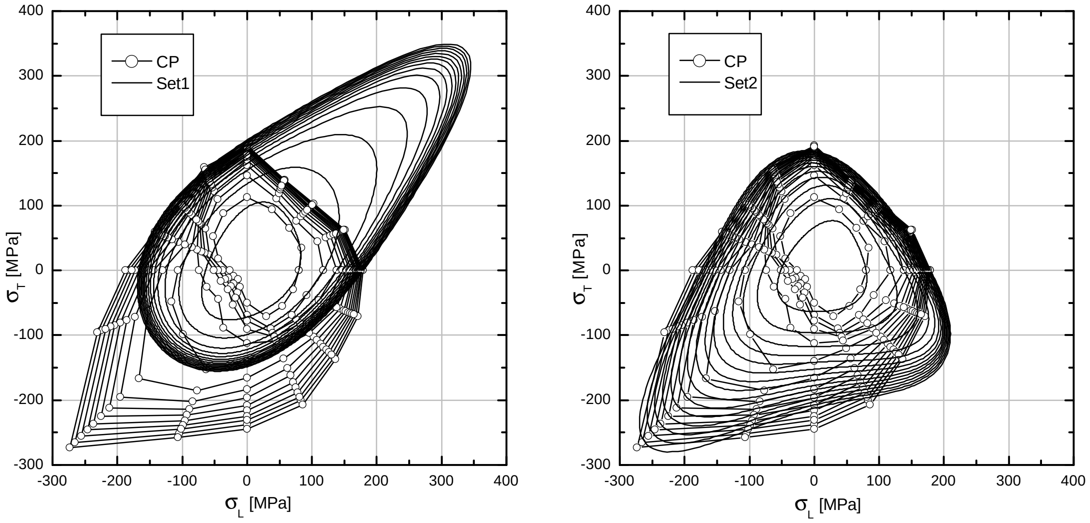

Figure 8.6: *Yield Surface of the textured Mg rolled plate of Figure 7.11* (**CP**) *and the yield surfaces of the corresponding optimised model parameter sets,* **Set1** *(left) and* **Set2** *(right)*

A slight non-convexity at high strains for compression along T-direction is also to be noticed, the optimisation procedure obviously did not reject this set. Nevertheless, this slight non-convexity is assumed not to be of high importance for the investigations made in this and the following chapter.

All attemps which have been performed with the optimization procedure in order to reproduce both the stress levels ${}^{jk}\bar{\sigma}^{ref}$ and the strain ratios ${}^{jk}\bar{r}^{ref}$ did not deliver satisfying results. The yield criterion and the hardening concept seems thus not to be adequate to describe accurately both the stress levels ${}^{jk}\bar{\sigma}^{ref}$ and the strain ratios ${}^{jk}\bar{r}^{ref}$. The detailled investigations in next section help to understand why it is so.

ϵ_p	0.0	0.01	0.02	0.03	0.04	0.05	0.06
σ_L $[MPa]$	40.0	79.773	117.982	138.144	147.671	153.358	158.128

ϵ_p	0.07	0.08	0.09	0.10	0.11	0.12	0.13
σ_L $[MPa]$	161.471	164.635	167.314	169.381	171.546	173.663	175.607

ϵ_p	0.14	0.15	1.
σ_L $[MPa]$	177.306	179.070	300.

Table 8.3: *Yielding behavior in L-direction as a function of the equivalent plastic strain for the reference yield surfaces, see Figure 7.11*

8.7 Plastic Anisotropy: Uniaxial Tensile Tests

The anisotropy of Mg sheets is investigated here by performing uniaxial tensile tests in the sheet's plane and by analysing the resulting stress levels and Lankford parameters. The calculations performed with the crystal plasticity model in considering the rolled plate texture in Figure 5.2b and the material parameters of Tables 5.2 and 5.3 are taken here as reference, **CP**. These calculations were performed in longitudinal and tranverse direction, as well as at loading orientations, θ, every $15\,^\circ$ from longitudinal direction towards tranverse direction. θ is the angle to longitudinal of the tensile direction.
The mechanical response of a magnesium plate described by model parameter set **Set1** in term of the Lankford parameters and stress levels is displayed in Figure 8.7 and compared with the reference results **CP** obtained with the crystal plasticity model. This comparison is made at three different values of true strains, 0.05, 0.10, and 0.15 on the range $\theta \in [0\,^\circ, 90\,^\circ]$. The same comparison is made for model parameter set **Set2** and is shown in Figure 8.8. In order to allow for the calculation of the Lankford parameters 3D simulations are necessary. Thus, When no other specification is indicated in Figures 8.7 and 8.8, the default value of the model parameters a_4 to a_6 is 1, and the default value of model parameters b_5 to b_{11} is 0. As discussed in first section of chapter 8 these values are those corresponding to a von Mises material. The influence of these model parameters on the simulation results will be discussed at the end of this chapter.
The reference simulations **CP** in Figure 8.7 show values of the Lankford parameters R which are almost constant with increasing strain and which vary between 2.5 and 3.2 depending on the angle θ. The stresses instead increase with increasing strain as the material hardens. This increase in the stress levels is almost linear with θ between longitudinal and transverse direction.

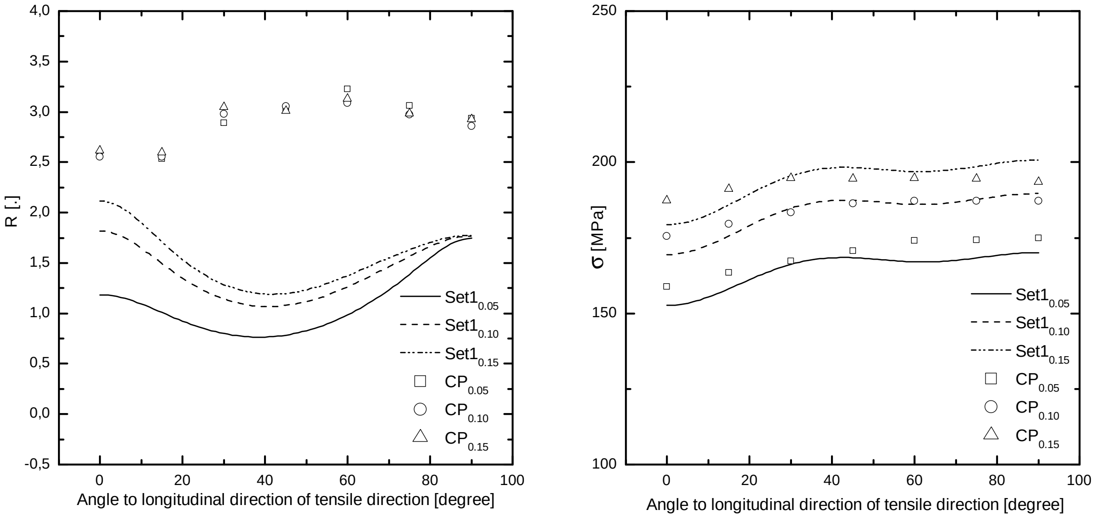

Figure 8.7: *Mechanical response of a Mg plate described by* **Set1** *and subjected to uniaxial tensile tests in the plate's plane, in terms of Lankford parameters* R *and stresses* σ

The Lankford parameters R, in Figure 8.7, are not well reproduced. The R values predicted by **Set1** are first not constant with increasing strain and secondly, they are only

almost half that of the reference one on the whole range $\theta \in [0\,°, 90\,°]$. These observations are a little surprising, since **Set1** has been obtained in fitting the strain ratios ${}^{jk}\bar{r}^{ref}$ of the biaxial tests which was thought to imply a better coincidence with Lankford parameters R. Lankford parameters are indeed themself nothing else but strain ratios. Figure 8.7 also shows that the stresses issued from **Set1** fit the reference data **CP** very well for all three values of strains, 0.05, 0.10, and 0.15 in the whole range $\theta \in [0\,°, 90\,°]$. It was already observed in Figure 8.6 that **Set1** reproduces the stresses well in both uniaxial tensile tests in longitudinal and transverse direction, but the really good agreement in the whole range $\theta \in [0\,°, 90\,°]$ was unexpected. This is actually due to the values chosen for a_4, b_5 and b_{10} which will be discussed in the context of the results presented in Figure 8.9 below.
The Lankford parameters and stress levels resulting from **Set2**, which are shown in Figure 8.8, are even much worse than those resulting from **Set1**. Optimizing the model parameter sets in accounting for the ratios ${}^{jk}\bar{r}^{ref}$ in the reference biaxial tests, as it was done for **Set1**, seems thus still to be effective and improves considerably the prediction of R values.

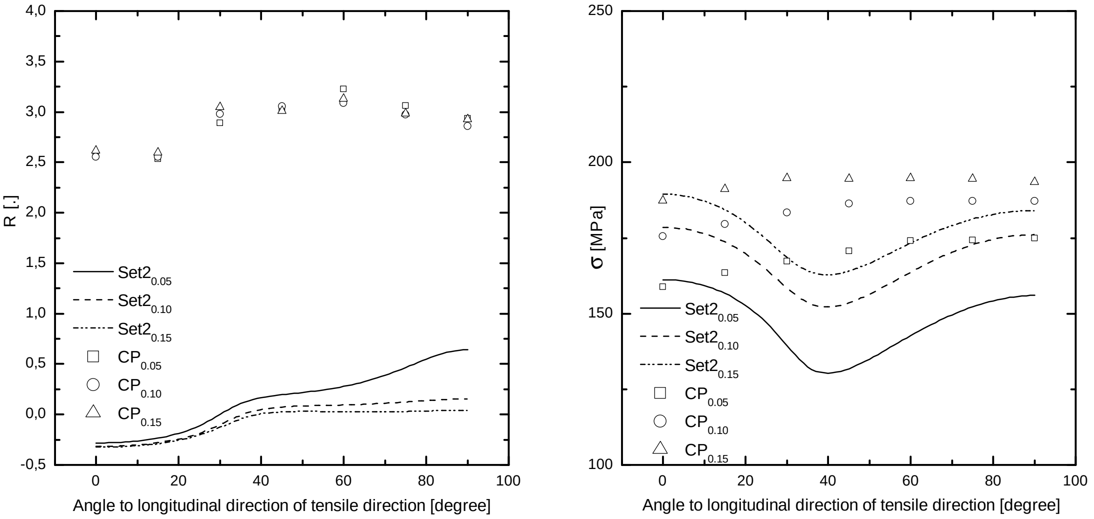

Figure 8.8: *Mechanical response of a Mg plate described by* **Set2** *and subjected to uniaxial tensile tests in the plate's plane, in term of Lankford parameters R and stresses σ*

The R values predicted by **Set2** are near to zero compared to the crystal plasticity results **CP** from about 2.5 to 3.2. They take even negative values which indicates that one of the directions of the tested specimen, width or thickness, becomes thicker. Such a behavior is unusual but is not necessary contrary to the assumption of volume constancy for plastic deformation. As it was already noted in Figure 8.7 the R values in Figure 8.8, are again not constant with increasing strain. It seems thus that neither optimizing the model parameters in accounting for both ${}^{jk}\bar{\sigma}^{ref}$ and ${}^{jk}\bar{r}^{ref}$ nor optimizing the model parameters in accounting for only one of these quantities leads to R values constant with increasing strain. The concept of hardening by model parameters depending on the equivalent plastic strain, ϵ_p, appears to be inappropriate for predicting correct Lankford parameters. Assuming an exponential function of ϵ_p for the model parameters, saturation would have to occur at low strains below 5%, if the Lankford coefficients are considered, and at about

15%, if the yield surfaces are examined, at the same time, which is obviously contradictory.

The stress levels resulting from **Set2** in Figure 8.8, are also far from the reference one **CP** compared to the one resulting from **Set1** in Figure 8.7. This may be considerably improved in changing the values of the model parameters a_4, b_5 and b_{10}, see Figure 8.9. These model parameters are related to the shear component σ_{LT}, see equation 8.2 and equation 8.3, and thus act on the material's yield behavior, see equation 8.1. The stress state for uniaxial tension in some angle θ is,

$$\sigma_{LL} = \sigma_\theta \cos^2\theta, \quad \sigma_{TT} = \sigma_\theta \sin^2\theta, \quad \text{and} \quad \sigma_{LT} = \sigma_\theta \sin\theta\cos\theta, \tag{8.56}$$

where σ_θ is the uniaxial stress under this angle. The stress component σ_{LT} is thus not zero in the range $\theta \in]0\,°, 90\,°[$. For the calculations displayed in Figure 8.9 the values of model parameters b_5 and b_{10} were chosen to remain equal to zero for simplicity, and only a_4 is varied from 1, 2 and 3.

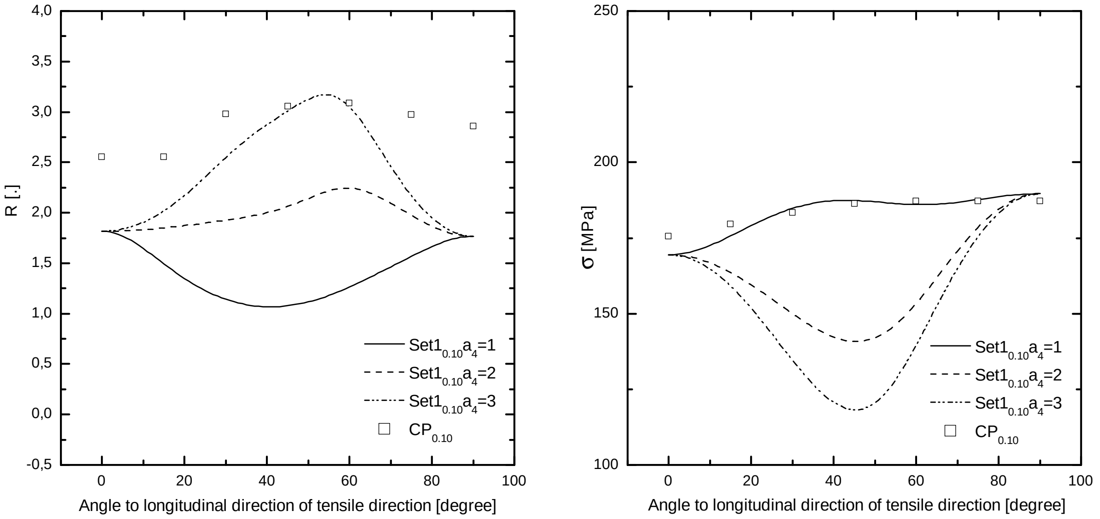

Figure 8.9: *Influence of model parameter a_4 onto the mechanical response of a Mg plate described by* **Set1** *and subjected to uniaxial tensile tests in the plate's plane, in terms of Lankford parameters R and stresses σ*

The influence of model parameter a_4, varying from 1 to 3, on the mechanical response of a Mg plate described by **Set1** at 0.10 strain is high since the R value for $\theta \simeq 50\,°$ has been almost doubled and the stress level for $\theta \simeq 45\,°$ has been reduced by more than 50 MPa. These results, shown in Figure 8.9, emphasize the fact that model parameters acting together with shear stress components may be well fitted while accounting for the Lankford parameters of uniaxial tension tests in the sheet's plane at different angles θ to the longitudinal direction. The variations of R values and stresses σ in Figure 8.9 with a_4 are opposite and dicted by the flow rule, here an associated flow rule see equation 4.6. In both cases, considering **Set1** and **Set2** in Figure 8.7 and 8.8, respectively, this opposite variation of the R values and stresses σ, as model parameter a_4 changes, would not lead to an improvement of the predicted strains and stresses. Indeed, for both **Set1** and **Set2** higher a_4 values would be needed to obtain higher R values but the consequence would be a bad prediction of the yield stresses σ for **Set1**, which was actually satisfactory, and an even worse prediction of the yield stresses σ for **Set2**, which was already not satisfying. This observation thus seems to indicate that an associated flow rule may definitely not be adapted to describe such an anisotropic mechanical behavior and hardening behavior like that of magnesium sheets. This is especially true as it seems impossible to obtain good R values and stress levels simultaneously.

Chapter 9

Phenomenological Modeling: Deep Drawing of a Cup

One example of the deformation of structures is the drawing, or deep drawing, process which is widely used and consists in forming metal sheets into cylindrical or box shaped parts by pressing the metal sheet into a cavity using a punch. Beverage cans, pans or containers of different shape and sizes are typical components which are produced by drawing processes, but also car body panels.

9.1 Drawing Process

Many phenomena which are observed in the drawing process of complicated shapes, like springback, wrinkling, necking, or earing can also be seen in drawing more simple shapes like cups. The simulation results presented in this chapter are therefore restricted to drawing of a circular blank. A schematic representation of the cup drawing process is shown in Figure 9.1. In this figure the so called blank is a circular metal sheet, with diameter D_b and thickness T, and is placed over a hollow die with inner diameter D_d and corner radius R_d. The blank is hold in place by the holder with corner radius R_h. During the process the punch, with diameter D_p and corner radius R_p, moves down under the action of force F. The action of the punch thus forms the desired cup.

In general, drawing of metals is an operation which consists in exerting tensile and associated compressive stresses over a large area of the blank. Plastic deformation develops therefore in large areas of the working piece being deformed. Moreover the stress state at a material point in the blank is multiaxial and depends on the area considered over the blank. This difference in stress state is displayed in Figure 9.2.

A material point situated in the flange region, which is the part of the blank that has not yet entered the die, is subjected to tensile stresses in radial direction, resulting from the punch pulling action, and to compression stresses in tangential direction, resulting themselves from the reduction of the flange diameter when moving in the direction of the die. A material point in the cup wall, portion of the cup being drawn in the die, is still subjected to tensile stresses in radial direction due to the punch pulling action. Moreover,

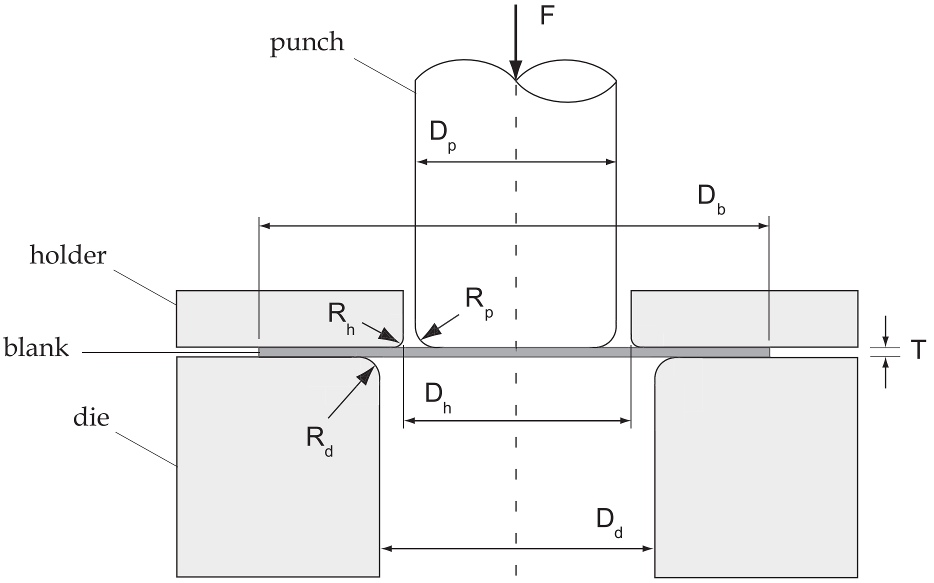

Figure 9.1: *Schematic representation of the cup drawing process*

tensile stresses in radial direction tend to induce contraction in tangential direction which is prevented by the punch geometry and thus tensile stresses in tangential direction result. A material point situated in the region where the blank is in contact with the punch bottom is often not subjected to high stresses. Because of the complicated stress states which may appear in this forming process it constitutes an adequate case for the study of sheets' structural responses depending on their mechanical properties.

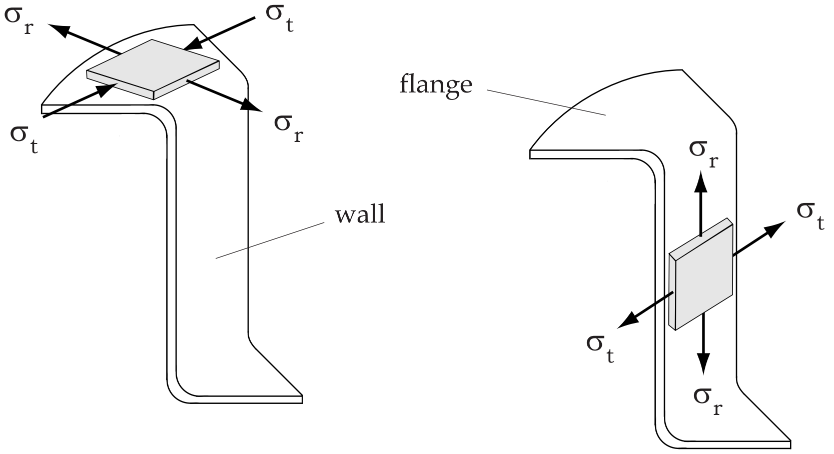

Figure 9.2: *Stress state developing during cup the drawing process*

The mechanical properties of the sheets studied in this chapter are introduced in the finite element model described in next section via the yield criterion of Cazacu and Barlat [19], introduced and described in chapter 8. The relation between textures and mechanical properties is realized with a crystal plasticity model, see chapter 7, and the model parameters for the yield criterion of [19] are calibrated with the optimisation procedure described in chapter 8. The resulting model parameters reproduce than, more or less well, the mechanical properties of the sheet with the considered texture. The influence of the magnesium rolled plates' texture onto their formability can finally be evaluated and studied in detail.

The finite element model used in the following calculations is presented in Figure 9.3. The blank consists of a disc of 8-nodes $3D$ brick finite elements with two layers of elements in the blank thickness. The three tools, die, holder and punch, are modeled by rigid surfaces.

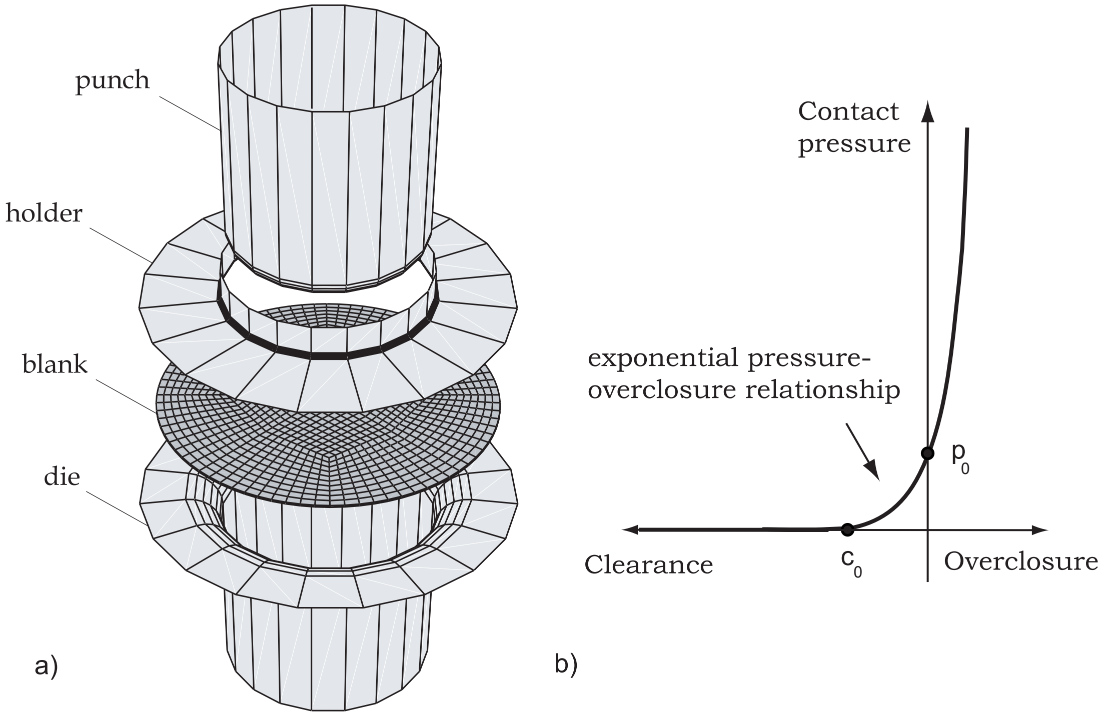

Figure 9.3: *Finite element model of a cup drawing process a) and exponential pressure-overclosure relationship for normal stress contact definition between two surfaces b)*

In this model the unitless dimensions of blank and tools are given in table 9.1. In the following simulation the punch displacement is strain driven and not force driven, as illustrated in Figure 9.1, and the contact between blank and all three tools, die, holder and punch is assumed not to be frictionless. The friction is assumed to be of Coulomb nature and is defined by the relation,

$$\tau = \mu \sigma_n \tag{9.1}$$

where the shear stress τ acting on the surface in contact is proportional to the normal stress σ_n acting between these surfaces through coefficient μ. The coefficients $\mu = 0.01$, 0.01, and 0.15 are chosen to describe frictional behavior between blank and die, blank and holder, as well as blank and punch, respectively. The contact definition between two surfaces, in term of the normal stress σ_n is defined through an exponential pressure-overclosure relationship with the parameters $p_0 = 2.0$ and $c_0 = 0.0005$ as shown in Figure 9.3. This relationship helps to avoid convergence problems in defining a continuous function for the contact normal stress σ_n from clearance to overclosure states.

D_b	T	D_d	R_d	D_h	R_h	D_p	R_p
20.	0.12	12.72	2.	12.5	0.25	12.	1.

Table 9.1: *Geometry, in dimensionless values, of the finite element model of the cup drawn process illustrated in Figure 9.1*

9.2 Cup Drawing Results using Different Sets of Model Parameters

As discussed in chapter 8 the phenomenological yield surface proposed by Cazacu and Barlat [19] is an appropriate candidate to describe the deformation behavior of magnesium alloys at phenomenological level since the plastic potential includes the third invariant of the stress tensor and hence accounts for anisotropy and unlike yielding in tension and compression. Its implementation, assuming first the equivalent plastic strain after von Mises as an internal variable to describe the state of plastic deformation, and secondly an associated flow rule to link stress and strain components, is however not fully satisfying, as discussed in chapter 8. In this section the influence of different hardening behaviors onto the resulting shapes of circular blanks subjected to the drawing process described previously is investigated.

The numerous model parameters have been identified using the optimisation procedure described in chapter 8 and based on the yield surfaces for rolled plates generated through virtual biaxial testing with the crystal plasticity model, see chapter 7. Since the yield surface shape changes with increasing plastic strain, the model parameters are defined as a function of the plastic strain and are thus, in general, not constant.

Figure 9.4 displays the distribution of the equivalent plastic strain in the deformed state of cups issued from the deep drawing process described in previous section, for four different model parameter sets: **Set1**, **Set2**, **Mises** and **Set1** ($\mathbf{a_4 = 3}$). The coefficients A_i, B_i, and C_i for **Set1** and **Set2**, describing the model parameters as a saturating exponential function of the equivalent plastic strain after equation 8.54, are given in Tables 8.1 and 8.2. In the case of **Set1** ($\mathbf{a_4 = 3}$) the coefficients A_i, B_i, and C_i are the same than those of **Set1** except that model parameter a_4 is defined as a constant equal to 3 instead of 1. The model parameters of the set **Mises** representing an isotropic von Mises material, are defined as constants with a_1 to a_6 being equal to 1 and b_4 to b_{11} being equal to 0, as discussed in the first section of chapter 8.

Figure 9.4 evidences that the cups' deformed configurations for the 4 sets are much different, and thus very sensitive to the model parameter sets used. The plate described by **Mises** a) shows for example a homogeneous distribution of the equivalent plastic strain ϵ_p over the cup circomference while the plate described by **Set1** ($\mathbf{a_4 = 3}$) d) shows a localisation of plastic deformation which leads to the constitution of four ears. Such an earing profile is typical for materials with anisotropic yielding behavior, it is even sort of a measure for anisotropy.

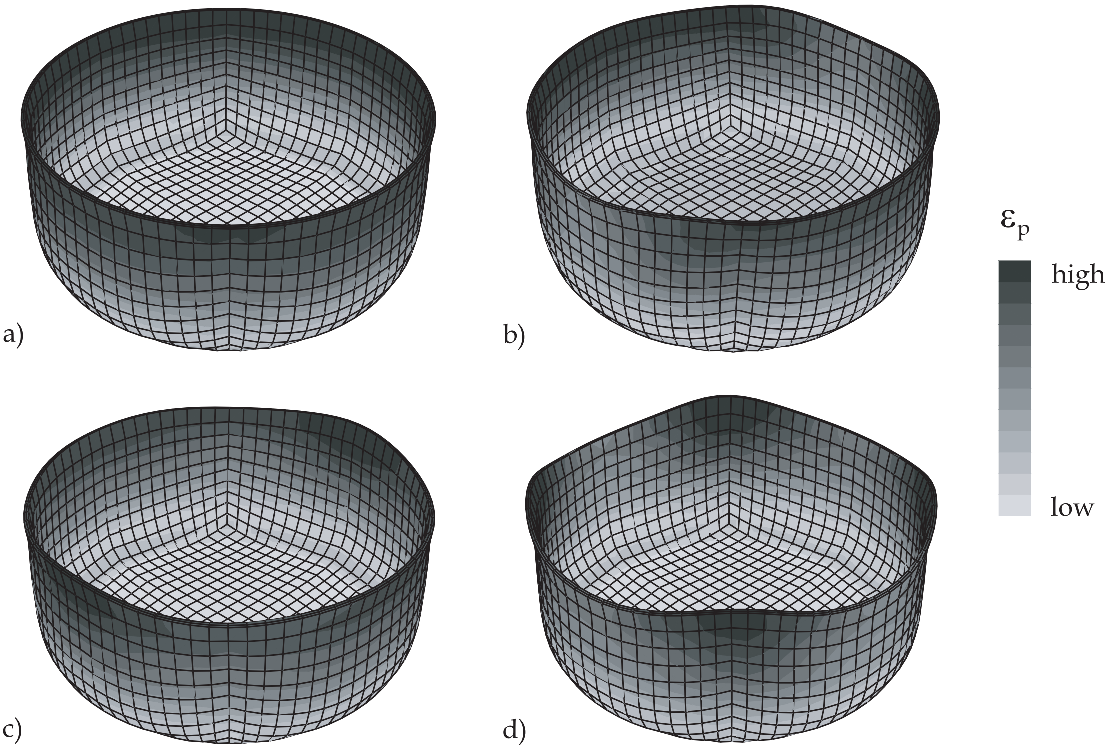

Figure 9.4: *Distribution of the equivalent plastic strain ϵ_p in the deformed state of cups issued from the deep drawing process described in previous section for four model parameter sets,* **Mises** a)*,* **Set2** b)*,* **Set1** c)*,* **Set1** ($a_4 = 3$) d)

Figure 9.5 allows for a more detailled analysis of the cup profile since the height of the deformed cup, normalized over the initial blank radius, is illustrated. As already recognized on Figure 9.4 the von Mises material, set **Mises**, deforms homogeneously, its normalized cup height is constant along the whole cup circumference. For this reason, the results of this simulation are taken as reference and the normalized cup height of the von Mises material is defined as the zero level. The normalized cup heights, over the blank initial radius, for the materials described by the other model parameter sets show deformations of about 3 to 4% above and below that of the von Mises material, set **Mises**. This level of deformations is far not neglectable if realistic results, comparable to experiments, are desired while modeling this process.

It appears also in Figure 9.5 that the earing profiles obtained with the different sets of model parameters are extremely different from each other in their shapes. The number of ears and their heights are obviously not the same. Due to these dissimilarities the choice of the most adequate parameter set has to be done regarding experimental data. With the implementation presented in this work the influence of yielding anisotropy, and thus of material texture, onto the mechanical properties of Mg sheets, as well as on the formability of these sheets, can be studied in detail in modeling this cup drawing process.

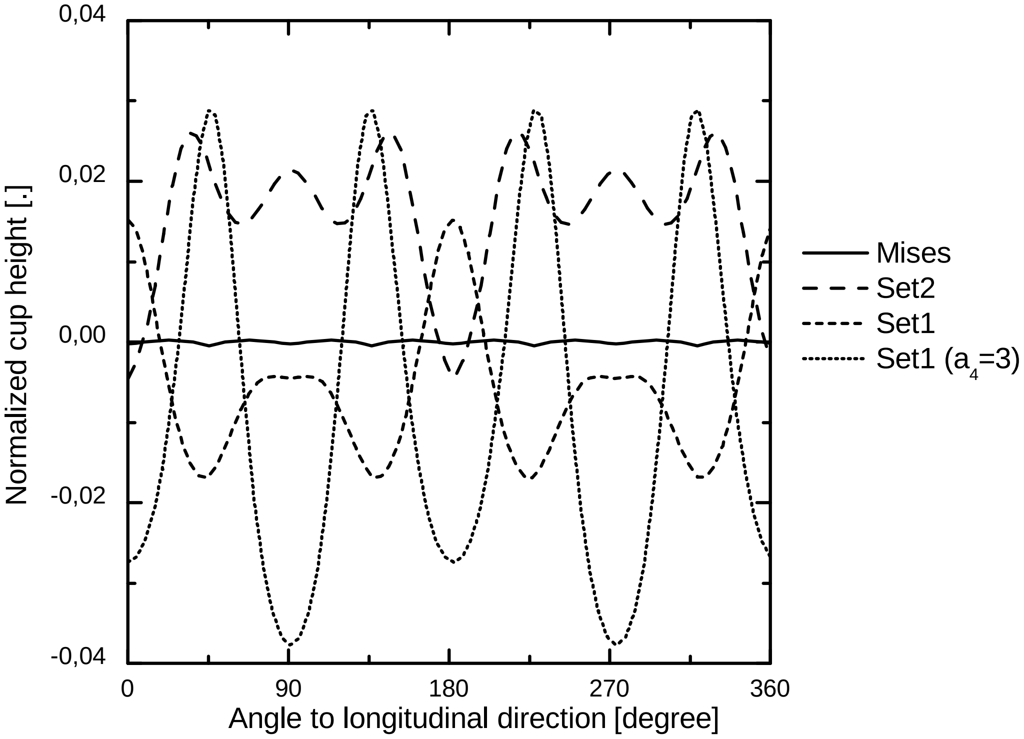

Figure 9.5: *Cup height, normalized over the initial blank radius, after deep drawing for the different model parameter sets of Figure 9.4*

Chapter 10

Summary and Conclusions

In the first part of the present thesis the mechanical behavior of pure magnesium at room temperature has been studied using a model for crystal plasticity without considering strain rate effects. The channel die experiments realized by Kelley and Hosford [43, 44] on single crystals and polycrystalline magnesium aggregates have been succesfully simulated. The experimental observations of a strong anisotropy, very different stress-strain curves, depending on the initial sample orientations could be reproduced accurately. This investigation revealed the active deformation modes in pure magnesium namely, basal slip $\langle a \rangle$ $\{0001\}$ $\langle 11\bar{2}0\rangle$, prismatic slip $\langle a \rangle$ $\{1\bar{1}00\}$ $\langle 11\bar{2}0\rangle$, pyramidal slip $\langle a + c\rangle$ $\{11\bar{2}2\}$ $\langle 11\bar{2}3\rangle$ and tensile twinning $\{10\bar{1}2\}$ $\langle 10\bar{1}1\rangle$, and even more, it was extremely usefull in identifying the numerous material parameters required by the crystal plasticity model.

This essential step permitted than to investigate the mechanical properties of extruded rods and rolled plates in mapping their corresponding textures into a finite element model. The experimentally observed macroscopic phenomena, like a strong anisotropy and an unlike yielding in tension and compression, of such rods and plates could be well reproduced. These phenomena could also be understood in detail in analyzing the level of activity of the different deformation modes compared to each other. For example, tensile twinning has been clearly identified to control the unlike yielding in tension and compression. Basal and prismatic slip were for example shown to compete with each other for the in-plane deformation of Mg rolled plates.

The yielding and the hardening behavior of Mg single crystals as well as polycrystalline aggregates have been generated in performing virtual biaxial test simulations. Their high sensitivity to crystallographic orientations and to the material parameters introduced into the model has been emphasized. These investigations revealed for example that, the yield surfaces of Mg single crystals are very much anisotropic and strongly non-convex at higher strains. The non-convexity is due to transition from one dominant deformation mode to another one and is particularly sharp because of the very disimilar hardening behavior of the corresponding deformation modes. But also, in non-textured samples, a yielding asymmetry in tension and compression is induced at strains of about 0.05 and 0.10, which explains the different mechanical behavior observed in tension and compression of Mg billet materials.

The approach, which consist in identifying the active deformation mechanisms of a hcp material with the channel die test, and extending afterwards to biaxial test simulations, appeared to be successful.

In order to perform simulations of forming processes, particularly the drawing of plates made of Mg alloys, the anisotropic yield potential of Cazacu and Barlat [19] was implemented and coupled with a hardening concept allowing for changes in the yield surface's shape during hardening. In this model the state of plasticity is represented by the von Mises equivalent plastic strain and an associated flow rule is assumed. Model parameters for this yield potential have been calibrated referring to computed biaxial test simulations and using an optimization procedure developed especially for this purpose. This phenomenological model revealed that plastic anisotropy for uniaxial tension in the plate's plane at different angles from the plate's longitudinal direction can be reproduced well in terms of yield stresses but badly in terms of strains (Lankford parameters). This investigation suggests that either an internal variable different from the equivalent plastic strain or more than one variable should be used to describe the state of plasticity. Moreover, this investigation suggests in particular that a non associated flow rule should be introduced. The structural behaviour of a circular blank subjected to deep drawing has been simulated with this model, which has shown that even a small yielding anisotropy and slightly different hardening behaviors have an important impact onto the cup deformed shape. Depending on the model parameter sets considered, the number and height of the resulting ears varied much. This underlines the importance of being able to control the initial texture of sheets which are destined to such fabrication processes. The phenomenological model developed here allows for interesting investigations linking plate texture, mechanical anisotropy, and structural deformation behavior.

The methodology presented here, starting from channel die tests of single crystals and polycrystalline aggregates and going to the simulation of drawing processes, leads to a profound understanding of the deformation behavior of magnesium and magnesium alloys, from microscopical to structural level. This methodology is well adapted to hcp metals and is therefore easily extendable to hcp metals other than Mg. It thus constitutes an attractive tool to be used for the improvement and optimisation of fabrication processes as well as for the development of hcp alloys with specific desired mechanical properties.

It would be of great interest for future work in this area to improve the modeling of tensile twinning in accounting for the lattice rotation. This would allow for the modeling of texture evolution and would permit thus an even more profound understanding of the underlying mechanisms controlling the deformation of hcp metals. Excellent contributions to this purpose are for example [4, 73, 75] and [86]. Very recently investigations of the mechanical response of magnesium sheets subjected to strain path changes and cyclic loading have been started, see [40, 52]. Both works emphasize the important role of mechanical twinning in defining the mechanical properties of Mg sheets. Another crucial aspect to be considered while developing or improving phenomenological models for magnesium is, that for a given final strain state different non-monotonic strain paths histories lead to different final stress states. Consequently, in order to allow for the development of a model able to reliably predict the mechanical behavior of magnesium and magnesium alloys sheets, future work should focus on the choice of an appropriate internal variable representing the state of plastic deformation, on the developement of an adequate non associated flow rule, and of a hardening concept accounting for strain path dependency.

Appendices

Appendix A

Definition of a Crystallographic Orientation

Usually either the Roe [68] or Bunge [17] system are used to define crystallographic orientations in space. Both systems use three so called Eulerian angles which define three succesive rotations around one of the axes of a coordinate system rotating under the action of the Eulerian angles. In the model for crystal plasticity used in this work and presented in chapter 3, which is implemented as a user-material (UMAT) subroutine for the finite element code ABAQUS, the possibility to use one of these systems is not given. Nevertheless, the possibility to use a system with angles $\big(\psi 1, \theta, \psi 2\big)$ defining three successive rotations around a global coordinate system $\big(X, Y, Z\big)$, which do not rotate under the action of the latter angles, is given.

The system used in this work, for describing crystallographic orientations, is still another one. The possibility, within the finite element code ABAQUS, to define local coordinate systems is used here. Indeed, using a system where three angles are to be defined implies that the material properties, in the ABAQUS input file, are to be defined for each crystallographic orientation considered. This may be a huge number in case of simulations of polycrystalline aggregates. Instead it was found more convinient by the author to define many local coordinate systems, in the ABAQUS input file, rather than material properties.

Figure 10.1 shows a hcp structure in the coordinate system of the crystal $\big(1, 2, 3\big)$ and an arbitrary representation of the hcp structure where the coordinate system of the crystal $\big(1, 2, 3\big)$ does not coincide with the global $\big(X, Y, Z\big)$ one.

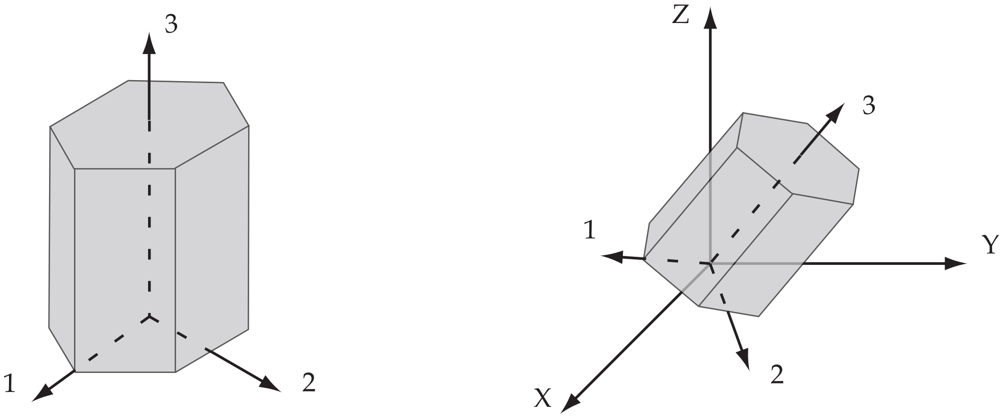

Figure 10.1: *hcp structure in the coordinate system of the crystal* $\big(1, 2, 3\big)$ *(left) and an example of crystallographic orientation where local* $\big(1, 2, 3\big)$ *and global* $\big(X, Y, Z\big)$ *coordinate systems are different (right)*

The problem of reproducing the real texture of a real material into a virtual model is complex because of the reduced orientations mapped in the model but not only, see for example [1, 48, 81, 76, 14]. Since almost no mesured experimental textures are available in this work the different texture types generated in this work, in the manner described just after, are destined to reproduce the billet material, extruded rod, and rolled texture

texture in a qualitative way only. A qualitative reproduction of the texture is assumed to capture well enough the mechanical behavior of the material.
The pole figures presented in this work all correspond to crystallographic orientation $\big(0001\big)$, in the Miller-Bravais coordinate system, indicating the c-axis of the hexagonal structure (axe 3 in Figure 10.1) and are represented via the stereographic projection method shown in Figure 10.2. In this method point P is the projection of point I, intersection point of the hexagon c-axis with the unit sphere, on the pole figure plane while the projection pole is at the sphere bottom.

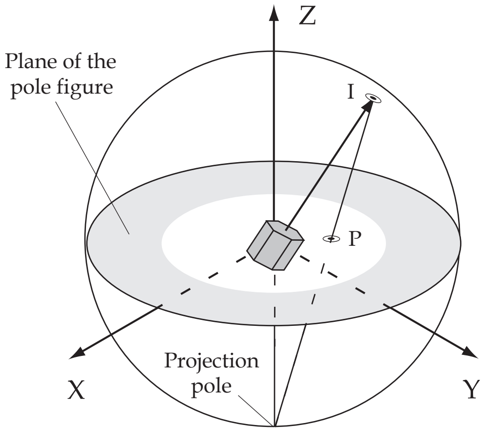

Figure 10.2: *Principle of the stereographic projection for the representation of pole figures*

Non-textured Material

A non textured material is characterised by a homogeneous repartition of crystallographic orientations over the surface of the unit sphere already shown in Figure 10.2. Only the orientations in space of the hexagon c-axis are of interest in this work and only those are therefore generated using the procedure described just after. As shown in Figure 10.3 where the angles θ and ϕ define the c-axis orientation in space, the infinitesimal surface element dS corresponding to this orientation may be written as,

$$dS = r^2 \sin\theta \, d\theta \, d\phi \tag{10.1}$$

where r is the unit sphere radius, 1. The surface S of the semi-sphere is then,

$$S = \int_0^{2\pi} \int_0^{\pi/2} \sin\theta \, d\theta \, d\phi = \int_0^{2\pi} d\phi \int_0^{\pi/2} \sin\theta \, d\theta = 2\pi \int_0^{\pi/2} \sin\theta \, d\theta = 2\pi. \tag{10.2}$$

The cumulative distribution function P, corresponding to the integrated probability density function p of a crystallographic orientation, is identified to the equation of the semi-sphere surface but has to be equal to 1, instead of 2π. The related probability density function and cumulative distribution function of a crystallographic orientation, which realise the desired homogeneous repartition of c-axis, is therefore,

$$p = \frac{\sin\theta}{2\pi} \quad \text{and} \quad P = \int_0^{2\pi} \int_0^{\pi/2} \frac{\sin\theta}{2\pi} \, d\theta \, d\phi = 1. \tag{10.3}$$

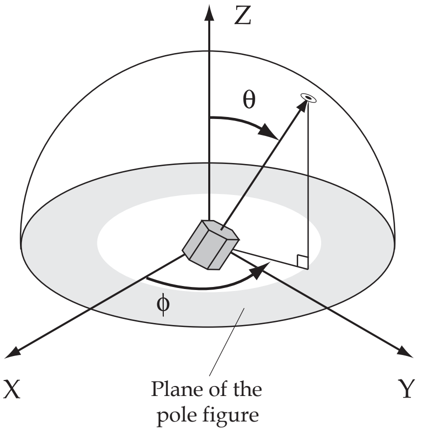

Figure 10.3: *Definition of crystallographic (0001) orientation for a non textured material*

The variables ϕ and θ are independent and are thus treated independently in the following.
One can recognize first that p is independent of ϕ, and P varies thus linearly with ϕ. This indicates that the values of angle ϕ may simply be generated randomly in the range $\big[0,1\big]$ and multiplied by its domain size 2π. In this way, the variable ϕ defining partly the orientation of discrete c-axis orientations in space is generated easily for a non textured material.
The usual way to generate values which follow a certain probability density function is to generate random values in the range $\big[0,1\big]$ and to consider the transformation issued from the inverse function of the cumulative distribution function. In the case of variable θ the inverse function of the cumulative distribution function is $\theta = \arccos\big(val\big)$ with $val \in \big[0,1\big]$. Following this method the variable θ defining partly the orientation of discrete c-axis orientations in space is also generated easily for a non textured material.
An additionnal random rotation around the c-axis, axis 3 of the hcp crystal coordinate system, is defined in order to avoid prefered orientations (other than c-axis) and thus any kind of texture in the virtual material.

Extruded Rod Texture

Extruded rod textures of magnesium are characterized by a strong prefered orientation of the grains' crystallographic orientation (c-axis) in the rod radial plane. A schematic representation of the model of a rod texture used in this work is displayed in Figure 10.4.
First, the direction of the c-axis in the radial plane is arbitrary and thus defined randomly while generating the discrete orientations needed in the numerical calculations of this work. The certain deviation of the c-axis direction from the radial plane, towards extrusion direction, is reproduced via a normal distribution centered on the radial plane along the pole figure circomference and with standard deviation σ_{sd}, see Figure 10.4. The characterization of this model, for generating a magnesium extruded rod texture, is thus realised in defining one single parameter σ_{sd}.

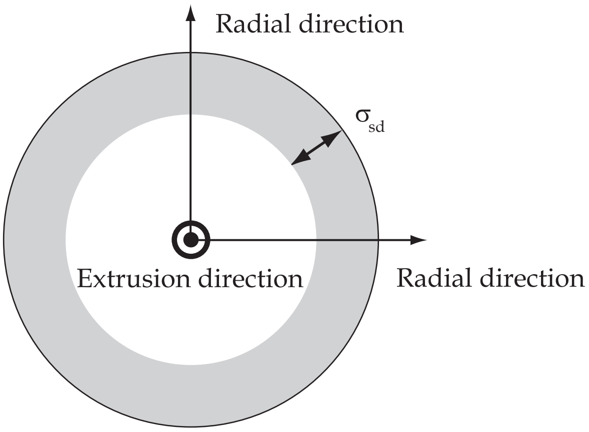

Figure 10.4: *Simple model of a (0001) pole figure corresponding to a Mg extruded rod texture*

Rolled Plate Texture

Rolled plate textures of magnesium are caracterised by a strong prefered orientation of the grains' crystallographic orientation (c-axis) in the plate thickness direction. Usually a certain deviation from the thickness direction, towards rolling and tranverse direction, is observed. This deviation is generally slightly higher in rolling than in transverse direction. Crystallographic orientations, other than c-axis orientation, usually do not show strong prefered orientations. In order to model a rolled plate texture, it is assumed to be composed of two main texture components representing the c-axis orientations, see Figure 10.5. These two components consist each in a two dimensional multinormal law defining the probability density function of the crystallographic orientations (c-axis) in the pole figure of Figure 10.5.

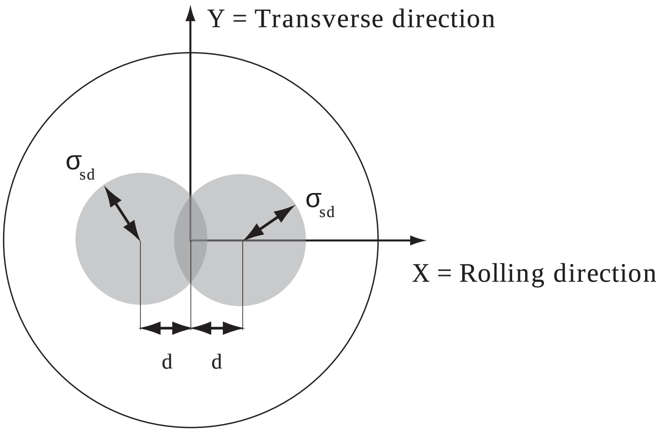

Figure 10.5: *Simple model of a (0001) pole figure corresponding to a Mg rolled plate texture*

Each probability density function p is defined as,

$$p(X,Y) = \frac{1}{4{\sigma_{sd}}^2}\left[exp\left(-\frac{\left(X-d\right)^2+Y^2}{2{\sigma_{sd}}^2}\right)+exp\left(-\frac{\left(X+d\right)^2+Y^2}{2{\sigma_{sd}}^2}\right)\right], \tag{10.4}$$

where X and Y are coordinates in the pole figure plane, d is the distance to the origin of the texture components' centers with respect to direction X, and σ_{sd} is the standard deviation of the multinormal law. The standard deviation is taken identical in both directions X and Y which actually correspond to rolling and transverse direction, respectively. After the principle of the stereographic projection shown in Figure 10.2 the two texture components are represented by a disc in the pole figure as illustrated in Figure 10.5. Additionnaly, in order to avoid prefered orientations for other crystallographic orientations than c-axis, a random rotation around the c-axis, axis 3 of the hcp crystal coordinate system, is defined. In this work, the characterisation of the model for generating a magnesium rolled plate texture is thus realised in defining only two parameters, d and σ_{sd}.

Appendix B

The partial derivatives of the quantities $\Phi^{(m)}$ and $\boldsymbol{\Gamma}^{(m)}$ with respect to the equivalent plastic strain $\epsilon_p^{(m)}$ and the stress tensor $\boldsymbol{\sigma}^{(m)}$, which appear in the system of equations 8.46, are developed in detail in this appendix. These derivatives are required for the numerical integration of the yield criterion of equation 8.1. The mathematical expression of the quantities to be derivated are defined in the system of equations 8.44 which reads,

$$\begin{cases} \Phi^{(m)} = f\big(\boldsymbol{\sigma}^{(m)}, {\epsilon_p}^{(m)}\big) - h\big({\epsilon_p}^{(m)}\big) = 0 \\ \boldsymbol{\Gamma}^{(m)} = \boldsymbol{\sigma}^{(m)} - \left[\mathbb{C}^e : \left(\mathbf{E} - \dfrac{\dfrac{\partial f}{\partial \boldsymbol{\sigma}^{(m)}} {\epsilon_p}^{(m)}}{\sqrt{\dfrac{2}{3}} \left[\dfrac{\partial f}{\partial \boldsymbol{\sigma}^{(m)}} : \dfrac{\partial f}{\partial \boldsymbol{\sigma}^{(m)}} \right]^{\frac{1}{2}}} \right) \right] = 0 \end{cases} .$$

The superscripts $^{(m)}$ in the system of equations 8.44 and 8.46 are omitted here for the sake of simplicity. The expression of the desired partial derivatives with respect to ϵ_p and $\boldsymbol{\sigma}$ are decomposed as:

- $$\frac{\partial \Phi}{\partial \epsilon_p} = \frac{\partial f}{\partial \epsilon_p} - \frac{dh}{d\epsilon_p} = \sum_i \frac{\partial f}{\partial J_2^o} \frac{\partial J_2^o}{\partial a_i} \frac{\partial a_i}{\partial \epsilon_p} + \sum_j \frac{\partial f}{\partial J_3^o} \frac{\partial J_3^o}{\partial b_j} \frac{\partial b_j}{\partial \epsilon_p} - \frac{dh}{d\epsilon_p}$$
- $$\frac{\partial \Phi}{\partial \boldsymbol{\sigma}} = \frac{\partial f}{\partial \boldsymbol{\sigma}} = \frac{\partial f}{\partial J_2^o} \frac{\partial J_2^o}{\partial \boldsymbol{\sigma}} + \frac{\partial f}{\partial J_3^o} \frac{\partial J_3^o}{\partial \boldsymbol{\sigma}}$$
- $$\frac{\partial \boldsymbol{\Gamma}}{\partial \epsilon_p} = \frac{\left[\mathbb{C}^e : \dfrac{\partial f}{\partial \boldsymbol{\sigma}} \right]}{\sqrt{\dfrac{2}{3}} \left[\dfrac{\partial f}{\partial \boldsymbol{\sigma}} : \dfrac{\partial f}{\partial \boldsymbol{\sigma}} \right]^{\frac{1}{2}}}$$
- $$\frac{\partial \boldsymbol{\Gamma}}{\partial \boldsymbol{\sigma}} = \frac{\partial \boldsymbol{\sigma}}{\partial \boldsymbol{\sigma}} + \left[\mathbb{C}^e : \frac{\partial}{\partial \boldsymbol{\sigma}} \left(\frac{\dfrac{\partial f}{\partial \boldsymbol{\sigma}} \epsilon_p}{\sqrt{\dfrac{2}{3}} \left[\dfrac{\partial f}{\partial \boldsymbol{\sigma}} : \dfrac{\partial f}{\partial \boldsymbol{\sigma}} \right]^{\frac{1}{2}}} \right) \right]$$

$$= \frac{\partial \boldsymbol{\sigma}}{\partial \boldsymbol{\sigma}} + \epsilon_p \sqrt{\frac{3}{2}} \left[\mathbb{C}^e : \left(\underbrace{\frac{\partial}{\partial \boldsymbol{\sigma}} \left(\left[\frac{\partial f}{\partial \boldsymbol{\sigma}} : \frac{\partial f}{\partial \boldsymbol{\sigma}} \right]^{-\frac{1}{2}} \right)}_{\Xi} \frac{\partial f}{\partial \boldsymbol{\sigma}} + \left[\frac{\partial f}{\partial \boldsymbol{\sigma}} : \frac{\partial f}{\partial \boldsymbol{\sigma}} \right]^{-\frac{1}{2}} \frac{\partial}{\partial \boldsymbol{\sigma}} \left(\frac{\partial f}{\partial \boldsymbol{\sigma}} \right) \right) \right]$$

$$= \frac{\partial \boldsymbol{\sigma}}{\partial \boldsymbol{\sigma}} + \epsilon_p \sqrt{\frac{3}{2}} \left[\mathbb{C}^e : \left(\Xi \frac{\partial f}{\partial \boldsymbol{\sigma}} + \left[\frac{\partial f}{\partial \boldsymbol{\sigma}} : \frac{\partial f}{\partial \boldsymbol{\sigma}} \right]^{-\frac{1}{2}} \frac{\partial^2 f}{\partial \boldsymbol{\sigma} \partial \boldsymbol{\sigma}} \right) \right].$$

The term Ξ may be further developed as

$$\Xi = -\frac{1}{2} \left[\frac{\partial f}{\partial \boldsymbol{\sigma}} : \frac{\partial f}{\partial \boldsymbol{\sigma}} \right]^{-\frac{3}{2}} \frac{\partial}{\partial \boldsymbol{\sigma}} \left(\sum_{\substack{k=1,3 \\ l=1,3}} \left(\frac{\partial f}{\partial \sigma_{kl}} \right)^2 \right)$$

In the previous expression the summation is realised over all the components of the stress tensor denoted by the subscript $_{kl}$. The second derivatives of function f with respect to the stress tensor σ may be rewritten as,

$$\begin{aligned}
\frac{\partial^2 f}{\partial \boldsymbol{\sigma} \partial \boldsymbol{\sigma}} &= \frac{\partial}{\partial \boldsymbol{\sigma}}\left(\frac{\partial f}{\partial \boldsymbol{\sigma}}\right) \\
&= \frac{\partial}{\partial \boldsymbol{\sigma}}\left(\frac{\partial f}{\partial J_2^o}\frac{\partial J_2^o}{\partial \boldsymbol{\sigma}} + \frac{\partial f}{\partial J_3^o}\frac{\partial J_3^o}{\partial \boldsymbol{\sigma}}\right) \\
&= \frac{\partial}{\partial \boldsymbol{\sigma}}\left(\frac{\partial f}{\partial J_2^o}\right) \otimes \frac{\partial J_2^o}{\partial \boldsymbol{\sigma}} + \frac{\partial f}{\partial J_2^o}\frac{\partial}{\partial \boldsymbol{\sigma}}\left(\frac{\partial J_2^o}{\partial \boldsymbol{\sigma}}\right) \\
&\qquad + \frac{\partial}{\partial \boldsymbol{\sigma}}\left(\frac{\partial f}{\partial J_3^o}\right) \otimes \frac{\partial J_3^o}{\partial \boldsymbol{\sigma}} + \frac{\partial f}{\partial J_3^o}\frac{\partial}{\partial \boldsymbol{\sigma}}\left(\frac{\partial J_3^o}{\partial \boldsymbol{\sigma}}\right) \\
&= \left(\frac{\partial^2 f}{\partial {J_2^o}^2}\frac{\partial J_2^o}{\partial \boldsymbol{\sigma}}\right) \otimes \frac{\partial J_2^o}{\partial \boldsymbol{\sigma}} + \frac{\partial f}{\partial J_2^o}\frac{\partial^2 J_2^o}{\partial \boldsymbol{\sigma} \partial \boldsymbol{\sigma}} + \frac{\partial f}{\partial J_3^o}\frac{\partial^2 J_3^o}{\partial \boldsymbol{\sigma} \partial \boldsymbol{\sigma}}.
\end{aligned}$$

In the above expression the term $\frac{\partial}{\partial \boldsymbol{\sigma}}\left(\frac{\partial f}{\partial J_2^o}\right)$ is reformulated as $\frac{\partial^2 f}{\partial {J_2^o}^2}\frac{\partial J_2^o}{\partial \boldsymbol{\sigma}}$, and $\frac{\partial}{\partial \boldsymbol{\sigma}}\left(\frac{\partial f}{\partial J_3^o}\right) = 0$ after equation 8.1 is used.

The derivatives are now expressed as functions of the following quantities:

$$\frac{\partial f}{\partial J_2^o} \quad \frac{\partial f}{\partial J_3^o} \quad \frac{\partial J_2^o}{\partial a_i} \quad \frac{\partial J_3^o}{\partial b_j} \quad \frac{\partial a_i}{\partial \epsilon_p} \quad \frac{\partial b_j}{\partial \epsilon_p} \quad \frac{dh}{d\epsilon_p} \quad \frac{\partial J_2^o}{\partial \boldsymbol{\sigma}} \quad \frac{\partial J_3^o}{\partial \boldsymbol{\sigma}} \quad \frac{\partial^2 f}{\partial {J_2^o}^2} \quad \frac{\partial^2 J_2^o}{\partial \boldsymbol{\sigma} \partial \boldsymbol{\sigma}} \quad \frac{\partial^2 J_3^o}{\partial \boldsymbol{\sigma} \partial \boldsymbol{\sigma}}.$$

Since most of these derivatives are vectorial and tensorial quantities having many components, a detailed development of each of these quantities would be very long and is therefore not presented here. Moreover, these derivatives can be obtained from equations 8.34, 8.2, 8.3 and 8.9, the variables a_i and b_j appearing in equations 8.2 and 8.3 as well as σ_L in equation 8.9 being functions of the equivalent plastic strain.

Appendix C

In both Tables in this Appendix the 16 lines denotes the biaxial loading paths of the yield surfaces in the (L,T)-planes (indice k in chapter 8), starting from uniaxial tension in longitudinal direction. The 15 rows denotes the isocontours of plastic strain (indice j in chapter 8), from $\epsilon = 0.01$ to 0.15.

	$j = 1$	2	3	4	5	6	7	8	9	10	11	12	13	14	15
$k = 1$	20.	20.	20.	20.	20.	20.	20.	20.	20.	20.	20.	20.	20.	20.	20.
2	1.	1.	1.	1.	1.	1.	1.	1.	1.	1.	1.	1.	1.	1.	1.
3	20.	20.	20.	20.	20.	20.	20.	20.	20.	20.	20.	20.	20.	20.	20.
4	1.	1.	1.	1.	1.	1.	1.	1.	1.	1.	1.	1.	1.	1.	1.
5	20.	20.	20.	20.	20.	20.	20.	20.	20.	20.	20.	20.	20.	20.	20.
6	0.	0.	0.	0.	0.	0.	0.	0.	0.	0.	0.	0.	0.	0.	0.
7	0.	0.	0.	0.	0.	0.	0.	0.	0.	0.	0.	0.	0.	0.	0.
8	0.	0.	0.	0.	0.	0.	0.	0.	0.	0.	0.	0.	0.	0.	0.
9	0.	0.	0.	0.	0.	0.	0.	0.	0.	0.	0.	0.	0.	0.	0.
10	0.	0.	0.	0.	0.	0.	0.	0.	0.	0.	0.	0.	0.	0.	0.
11	0.	0.	0.	0.	0.	0.	0.	0.	0.	0.	0.	0.	0.	0.	0.
12	0.	0.	0.	0.	0.	0.	0.	0.	0.	0.	0.	0.	0.	0.	0.
13	0.	0.	0.	0.	0.	0.	0.	0.	0.	0.	0.	0.	0.	0.	0.
14	0.	0.	0.	0.	0.	0.	0.	0.	0.	0.	0.	0.	0.	0.	0.
15	0.	0.	0.	0.	0.	0.	0.	0.	0.	0.	0.	0.	0.	0.	0.
16	0.	0.	0.	0.	0.	0.	0.	0.	0.	0.	0.	0.	0.	0.	0.

Table 10.1: *Weight coefficients* ${}^{jk}\mu^{\bar{\sigma}}$ *used in the optimisation procedure for* **Set1** *in chapter 8, the coefficients* ${}^{jk}\mu^{\bar{r}}$ *all set to zero*

	$j = 1$	2	3	4	5	6	7	8	9	10	11	12	13	14	15
$k = 1$	25.	25.	25.	25.	25.	0.	0.	0.	0.	0.	25.	25.	25.	25.	25.
2	1.	1.	1.	1.	1.	0.	0.	0.	0.	0.	1.	1.	1.	1.	1.
3	500.	500.	500.	500.	500.	0.	0.	0.	0.	0.	500.	500.	500.	500.	500.
4	1.	1.	1.	1.	1.	0.	0.	0.	0.	0.	1.	1.	1.	1.	1.
5	25.	25.	25.	25.	25.	0.	0.	0.	0.	0.	25.	25.	25.	25.	25.
6	1.	1.	1.	1.	1.	0.	0.	0.	0.	0.	1.	1.	1.	1.	1.
7	1.	1.	1.	1.	1.	0.	0.	0.	0.	0.	1.	1.	1.	1.	1.
8	1.	1.	1.	1.	1.	0.	0.	0.	0.	0.	1.	1.	1.	1.	1.
9	10.	10.	10.	10.	10.	0.	0.	0.	0.	0.	10.	10.	10.	10.	10.
10	1.	1.	1.	1.	1.	0.	0.	0.	0.	0.	1.	1.	1.	1.	1.
11	5.	5.	5.	5.	5.	0.	0.	0.	0.	0.	5.	5.	5.	5.	5.
12	1.	1.	1.	1.	1.	0.	0.	0.	0.	0.	1.	1.	1.	1.	1.
13	10.	10.	10.	10.	10.	0.	0.	0.	0.	0.	10.	10.	10.	10.	10.
14	1.	1.	1.	1.	1.	0.	0.	0.	0.	0.	1.	1.	1.	1.	1.
15	1.	1.	1.	1.	1.	0.	0.	0.	0.	0.	1.	1.	1.	1.	1.
16	1.	1.	1.	1.	1.	0.	0.	0.	0.	0.	1.	1.	1.	1.	1.

Table 10.2: *Weight coefficients* ${}^{jk}\mu^{\bar{r}}$ *used in the optimisation procedure for* **Set2** *in chapter 8, the coefficients* ${}^{jk}\mu^{\bar{\sigma}}$ *all set to zero*

Bibliography

[1] Adams B., Olson T., The mesostructure-properties linkage in polycrystals, *Prog. Mater. Sci.* **43**, p.1, 1998

[2] Agnew S.R., Duygulu Ö., Plastic anisotropy and the role of non-basal slip in magnesium alloy AZ31B, *Int. J. Plasticity* **21**, p.1161, 2005

[3] Agnew S.R., Tomé C.N., Brown D.W., Holden T.M., Vogel S.C., Study of slip mechanisms in magnesium alloy by neutron diffraction and modeling, *Scripta Mater.* **48**, p.1003, 2003

[4] Agnew S.R., Yoo M.H., Tomé C.N., Application of texture simulation to understanding mechanical behavior of Mg and solid solution alloys containing Li or Y, *Acta Mater. 49*, p.4277, 2001

[5] Anand L., Kothari M., A computational procedure for rate independent crystal plasticity, *J. Mech. Phys. Solids* **44**, p.525, 1996

[6] Ando S., Tonda H., Non-basal slip in magnesium-lithium alloy single crystals, *Mater. T. JIM* **41**, p.1188, 2000

[7] Asaro R.J., Micromechanics of crystals and polycrystals, *Adv. Appl. Mech.* **23**, p.1, 1983

[8] Asaro R.J., Crystal plasticity, *J. Appl. Mech.* **50**, p.921, 1983

[9] ASTM, Metal Test Methods and Analytical Procedures, *Annual Book of ASTM Standards*, West Conshohocken, PA, 3.01, p.481, 1996

[10] Banabic D., Bunge H.-J., Pöhland K., Tekkaya A.E., Formability of Metallic Materials, (ed. Banabic D.), *Springer-Verlag: Berlin Heidelberg New York*, 2000

[11] Bassani J.L., Wu T., Latent hardening in single crystals, Part II, Analytical characterisation and predictions, *P. Roy. Soc. A, in press*, 1991

[12] Bauschinger J., Über die Veränderung der Elastizitätsgrenze und des Elastizitätsmoduls verschiedener Metalle, *Der Civilingenieur*, p.289, 1881

[13] Beck A., Magnesium und seine Legierungen, *Springer-Verlag: Berlin*, 1939

[14] Böhlke T., Haus U.-U., Schulze V., Crystallographic texture approximation by quadratic programming, *Acta Mater.* **54**, p.1359, 2006

[15] Brocks W., Steglich D., Hybrid Methods. In: Comprehensive Structural Integrity - Fracture of Materials from Nano to Macro, *Mechanical Characterization of Structural Materials, Elsevier*, **11**, to be published

[16] Brown D.W., Agnew S.R., Bourke M.A.M., Holden T.M., Vogel S.C., Tomé C.N., Internal strain and texture evolution during deformation twinning in magnesium, *Mater. Sci. Eng. A* **399**, p.1, 2005

[17] Bunge H.J., Zur Darstellung allgemeiner Texturen, *Z. Metallkd.* **56**, p.872, 1965

[18] Burke E.C., Hibbard W.R., Plastic deformation of magnesium single crystals, *T. Metall. Soc. AIME* **194**, p.295, 1952

[19] Cazacu O., Barlat F., A criterion for description of anisotropy and yield differential effects in pressure insensitive materials, *Int. J. Plasticity* **20**, p.2027, 2004

[20] Cazacu O., Plunkett B., Barlat F., Orthotropic yield criterion for hexagonal closed packed metals, *Int. J. Plasticity* **22**, p.1171, 2006

[21] Cottrell A.H., Dislocations and plastic flow of crystals, *Oxford University Press: London*, 1953

[22] Cuitiñio A.M., Ortiz M., Computational modelling of single crystals, *Model. Simul. Mater. Sci.* **1**, p.225, 1992

[23] Diard O., Leclercq S., Rousselier G., Gailletaud G., Evaluation of finite element based analysis of 3D multicrystalline aggregates plasticity Application to crystal plasticity model identification and the study of stress and strain fields near grain boundaries, *Int. J. Plasticity* **21**, p.691, 2005

[24] Drucker D.C., Relation of experiments to mathematical theories of plasticity, *J. Appl. Mech.* **16**, p.349, 1949

[25] Drucker D.C., On the postulate of stability of material in the mechanics of continua, *J. Mécanique* **3**, p.235, 1964

[26] Garcés G., Pérez P., Adeva P., Effect of the extrusion texture on the mechanical behaviour of Mg-SiC$_p$ composites, *Scripta Mater.* **52**, p.615, 2005

[27] Garcés G., Rodríguez, Pérez P., Adeva P., Effect of volume fraction and particle size on the microstructure and plastic deformation of Mg-Y$_2$O$_3$ composites, *Mater. Sci. Eng. A* **419**, p.357, 2006

[28] Göken J., Bohlen J., Letzig D., Brockmeier H.-G., Kainer K.U., In: Kaufmann H., Uggowitzer J.P., Wahlen A., (ed.), 2 Ranshofener Leichtmetalltage 2002 - Vom Werkstoff zum Bauteilsystem, *LKR-Verlag*, p.229, 2002

[29] Hauser F.E., Landon P.R., Dorn J.E., Deformation and fracture mechanisms of polycrystalline magnesium at low temperatures, *Transactions of the ASM* **48**, p.986, 1956

[30] Hauser F.E., Starr C.D., Tietz L., Dorn J.E., Deformation mechanisms in polycrystalline aggregates of magnesium, *Transaction of the ASM* **47**, p.102, 1955

[31] Hill R., A theory of the yielding and plastic flow of anisotropic metals, *P. Roy. Soc. Lond. A* **193**, p.281, 1948

[32] Hill R., The Mathematical Theory of Plasticity, *Oxford University Press*, Chapter XII, 1950

[33] Hill R., Generalized constitutive relations for incremental deformation of metal crystals by multislip, *J. Mech. Phys. Solids* **20**, p.401, 1966

[34] Hill R., Rice J.R., Constitutive analysis of elastic-plastic crystals at arbitrary strain, *J. Mech. Phys. Solids* **20**, p.401, 1972

[35] Hornbogen E., Werkstoffe Aufbau und Eigenschaften, 8. Auflage, Springer, 2006

[36] Hosford W.F., Mechanical behavior of materials, *Cambridge University Press*, 2005

[37] Huang Y., A user-material subroutine incorporating single crystal plasticity in the ABAQUS finite element program, *Report MECH-178, Div. Applied Science, Harvard University*, Cambridge (MA), 1991

[38] Hughes T.J.R., Winget J., *Int. J. Numer. Meth. Eng.* **15**, p.1862, 1980

[39] Hutchinson J.W., Bounds and self-consistent estimates for creep of polycrystalline materials, *P. Roy. Soc. Lond. A* **348**, p.101, 1976

[40] Jain A., Agnew S.R., Effect of twinning on the mechanical behavior of a magnesium alloy sheet during strain path changes, *Magnesium Technology 2006*, Lou A.A., Neelameggham N.R., Beals R.S., (Ed.), TMS (The Minerals, Metals & Materials Society), 2006

[41] Kainer K.U. (ed.), Magnesium Alloys and Their Applications, *Wiley-VCH*, Weinheim, 2003

[42] Kaiser F., Bohlen J., Letzig D., Kainer K.U., Styczynski A., Hartig C., Influence of rolling conditions on the microstructure and mechanical properties of magnesium sheet AZ31, *Adv. Eng. Mater.* **5**, p.891, 2003

[43] Kelley E.W., Hosford W.F., Plane-strain compression of magnesium and magnesium alloy crystals, *T. Metall. Soc. AIME* **242**, p.5, 1968

[44] Kelley E.W., Hosford W.F., The deformation characteristics of textured magnesium, *T. Metall. Soc. AIME* **242**, p.654, 1968

[45] Kleiner S., Uggowitzer P.J., Mechanical anisotropy of extruded Mg-6% Al-1% Zn alloy, *Mater. Sci. and Eng. A* **379**, p.258, 2004

[46] Kocks U.F., A statistical theory of flow stress and work-hardening, *Phil. Mag.* **13**, p.541, 1966

[47] Kocks U.F., The theory of an obstacle-controlled yield strength-report after an international workshop, *Mater. Sci. Eng.* **27**, p.291, 1977

[48] Kocks U.F., Kallend J.S., Biondo A.C., Accurate representation of general textures by a set of weighted grains, *Texture. Microstruct.* **14-18**, p.199, 1991

[49] Kröner E., Zur plastischen Verformung des Vielkristalls, *Acta metall. Mater.* **9**, p.155, 1961

[50] Lebensohn R.A., Tomé C.N., A self-consistent anisotropic approach for the simulation of plastic deformation and texture development of polycrystals: application to zirconium alloys, *Acta Metall. Mater.* **41**, p.2611, 1993

[51] Letzig D., Swiostek J., Bohlen J., Beaven P.B., Extrusion of AZ-series magnesium alloys, *Materials Science Forum, in press*, Proc. of "Magnesium Technology in the Global Age", Montreal, 2006

[52] Lou X., Li M., Boger R.K., Agnew S.R., Wagoner R.H., Deformation of O-temper AZ31B Mg sheet under monotonic and cyclic loading, *Magnesium Technology 2006*, Lou A.A., Neelameggham N.R., Beals R.S., (Ed.), TMS (The Minerals, Metals & Materials Society), 2006

[53] Mahnken R., Identification of material parameters for constitutive equations. In: Encyclopedia of Computational Mechanics (ed. Stein E., de Borst R. and Hughes Th.J.R.), *John Wiley & Sons, Chichester*, p.637, 2004

[54] Mandel J., Plasticité Classique et Viscoplasticité, *CISM Courses and Lectures No. 97, Springer-Verlag: Berlin*, 1972

[55] Miehe C., Exponential map algorithm for stress updates in anisotropic multiplicative elastoplasticity for single crystals, *Int. J. Numer. Meth. Eng.* **39**, p.3367, 1996

[56] Miehe C., Schotte J., Crystal plasticity and evolution of polycrystalline microstructure. In: Encyclopedia of Computational Mechanics (ed. Stein E., de Borst R. and Hughes Th.J.R.), *John Wiley & Sons, Chichester*, p.267, 2004

[57] Needleman A., Asaro R.J., Lemonds J., Peirce D., Finite element analysis of crystalline solids, *Comput. Method. Appl. M.* **52**, p.689, 1985

[58] Neelameggham N.R., Kaplan H.I., Powell B.R., (ed.), Magnesium Technology 2005, *Publication of TMS*

[59] Obara T., Yoshinga H., Morozumi S., $\{11\bar{2}2\}$ $\langle\bar{1}\bar{1}23\rangle$ slip system in magnesium, *Acta Metall. Mater.* **21**, p.845, 1973

[60] Odqvist F.K.G., Die Verfestigung von flusseisenähnlichen Körpern, *Ztschr. f. angew. Math. und Mech.* **13**, p.360, 1933

[61] Partridge P.G., The crystallography and deformation modes of hexagonal close-packed metals, *Metallurgical Reviews* **118**, p.169, 1967

[62] Peirce D., Asaro R.J., Needleman A., An analysis of nonuniform and localized deformation in ductile single crystals, *Acta Metall. Mater.* **30**, p.1082, 1982

[63] Peirce D., Asaro R.J., Needleman A., Material rate dependence and localized deformation in crystalline solids, *Acta Metall. Mater.* **31**, p.1951, 1983

[64] Reed-Hill R.E., Robertson W.D., Deformation of magnesium single crystals by non basal slip, *T. Metall. Soc. AIME* **209**, p.496, 1957

[65] Reed-Hill R.E., Robertson W.D., Pyramidal slip in magnesium, *T. Metall. Soc. AIME* **212**, p.256, 1958

[66] Rice J.R., Inelastic constitutive relations for solids: an internal variable theory and application to metal plasticity, *J. Mech. Phys. Solids* **19**, p.433, 1971

[67] Rockafellar R.T., Convex analysis, *Princeton University Press*, Princeton, NY, 1972

[68] Roe R.J., Description of crystallite orientation in polycrystalline materials. II.General solution to pole figure inversion, *J. Appl. Phys.* **36**, p.2024, 1965

[69] Schmid E., Proc. Int. Cong. Appl. Mech., p.342, 1924

[70] Schmid E., Boas W., Kristallplastizität, *Springer-Verlag: Berlin*, 1935

[71] Seeger A., Theorie der Gitterfehlstellen, In *Handbuch der Physik Bd. VII/l, Fluegge S. (ed.), Springer-Verlag: Berlin*, p.383, 1958

[72] Shaik B., Brocks W., Correlation between deformation mechanisms and yield surfaces of hcp metals, *HGF Forschungszentrum Geesthacht, Internal report Ref. WMS/06/08*, 2006

[73] Staroselsky A., Anand L., A constitutive model for hcp materials deforming by slip and twinning: application to magnesium alloy AZ31B, *Int. J. Plasticity* **19**, p.1843, 2003

[74] Stohr J.F., Poirier J.P., Etude en microscopie electronique du glissement pyramidal $\{11\bar{2}2\}$ $\langle 11\bar{2}3\rangle$ dans le magnesium, *Phil. Mag.* **25**, p.1313, 1972

[75] Styczynski A., Hartig Ch., Bohlen J., Letzig D., Cold rolling textures in AZ31 wrought magnesium alloy, *Scripta Mater.* **50**, p.943, 2004

[76] Tarasiuk J., Wierzbanowski K., Bacroix B., Texture decomposition into Gauss-shaped functions: classical and genetic algorithm methods, *Comp. Mater. Sci.* **29**, p.179, 2004

[77] Taylor G.I., Plastic strain in metals, *J. I. Met.* **62**, p.307, 1938

[78] Taylor G.I., The mechanism of plastic deformation, *P. Roy. Soc. Lond. A* **145**, p.362, 1934

[79] Tegart W.J.McG., Independent slip systems and ductility of hexagonal polycrystals, *Phil. Mag.* **9**, p.339, 1964

[80] Teodosiu C., A dynamic theory of dislocations and its applications to the theory of the elastic-plastic continuum, *Fundamental Aspects of Dislocation Theory, vol. II, US National Bureau of Standards, Special Publication*, p.837, 1970

[81] Tóth L.S., Van Houtte P., Discretization techniques for orientation distribution functions, *Texture. Microstruct.* **19**, p.229, 1992

[82] Tresca H., Mémoire sur l'écoulement des corps solides soumis à de fortes pressions, *CR Acad. Sci. Paris* **59**, p.754, 1864

[83] von Mises R., Die Mechanik der festen Körper im plastischen deformablen Zustand, *Nachrichten der Königl. Ges. der Wiss. zu Göttingen*, p.582, 1913

[84] von Mises R., Mechanik der plastischen Formänderung von Kristallen, *Ztschr. f. angew. Math. und Mech.* **8**, p.307, 1928

[85] Wonsiewicz B.C., Backofen W.A., Plasticity of magnesium crystals, *T. Metall. Soc. AIME* **239**, p.1422, 1967

[86] Yi S.B., Davies C.H.J., Brokmeier H.-G., Molmaro R.E., Kainer K.U., Homeyer J., Deformation and texture evolution in AZ31 magnesium alloy during uniaxial loading, *Acta Mater.* **54**, p.549, 2006

[87] Yoo M.H., Agnew S.R., Morris J.R., Ho K.M., Non-basal slip systems in HCP metals and alloys: source mechanisms, *Mater. Sci. Eng. A* **319-321**, p.87,2001

[88] Yoo M.H., Morris J.R., Ho K.M., Agnew S.R., Nonbasal deformation modes of hcp metals and alloys: role of dislocation source and mobility, *Metallurgical and Materials Transactions* **33A**, p.813, 2002

[89] Yoshinaga H., Horiuchi R., On the nonbasal slip in magnesium crystals, *T. Jpn. I. JIM* **5**, p.14, 1963

List of Figures

List of Tables